133p.

Rec'd

Code-1 N64-26578 Cat. 27
Nasa Cr-58181

OTS PRICE

XEROX	$	10.50ph
MICROFILM	$	

EOS

ELECTRO-OPTICAL SYSTEMS, INC., Pasadena, California
A Subsidiary of the XEROX Corporation

c

Final Report 17 May 1963 to 16 November 1963

DESIGN STUDY OF A SOLAR HYDROGEN PROPULSION AND POWER SYSTEM

Prepared for
National Aeronautics and Space Administration
Office of Propulsion and Power Generation
Code RP
Washington 25, D.C.

Contract No. NAS 7-231
EOS Report 4000-Final ~~23 July 1964~~

~~[illegible]~~
15 JAN. 1965

Prepared by
F. McFarlane
B. Kalensher
B. Wilner
E. Findl

Approved by

B M. Wilner
B. M. Wilner
Associate Manager
Energy Conversion Division

ELECTRO-OPTICAL SYSTEMS, INC. - PASADENA, CALIFORNIA

CONTENTS

Page

1. INTRODUCTION 1
2. SUMMARY AND RECOMMENDATIONS 4
    - 2.1 Summary of Results 5
    - 2.2 Recommendations 7
        - 2.2.1 Hydrogen Diffusion 7
        - 2.2.2 Thermal Energy Storage 8
        - 2.2.3 Cavity Absorber Development 8
3. PERFORMANCE ANALYSIS OF COMPONENTS 9
    - 3.1 Propellant Storage and Feed System 9
        - 3.1.1 Vented and Non-Vented Systems 9
        - 3.1.2 Propellant Storage, Feed System Geometry, Structural Requirements 14
        - 3.1.3 Insulation Requirements 18
        - 3.1.4 Meteoroid Shielding 23
    - 3.2 Collector-Absorber Characteristics 28
    - 3.3 Nozzle Performance 43
    - 3.4 Diode Characteristics 51
    - 3.5 Energy Storage 52
4. DESIGN STUDY OF COMBINED CAVITY ABSORBER 64
    - 4.1 Introduction 64
    - 4.2 Cavity Entrance, Flux Control, and Top Plate Considerations 64
    - 4.3 Design Considerations for the Hydrogen Heat Transfer Coils 66
    - 4.4 Integration of the Thermionic Diodes 70
    - 4.5 Startup Operation 80

CONTENTS (cont)

Page

4.6 The Hydrogen Diffusion Problem 82

4.6.1 Hydrogen Diffusion from the Cavity 82

4.6.2 Hydrogen Diffusion from the Thermal Recovery System 86

5. DEPLOYMENT, INITIAL ORIENTATION, STATION KEEPING 90

5.1 Deployment and Initial Orientation 90

5.2 Station Keeping 91

6. DESIGN FOR A 24-HOUR SATELLITE SYSTEM 92

6.1 System Considerations 92

6.2 Preliminary Design of Combined Cavity Absorber for 24-Hr Orbit 97

7. MISSION STUDIES 101

7.1 Introduction 101

7.2 Analysis 102

7.3 Conclusions on Solar Probe Mission 110

7.4 SOHR-SET for Synchronous and Lunar Orbit Missions 115

ILLUSTRATIONS

Figure		Page
3-1	Propellant storage and feed system	11
3-2	Temperature entropy diagram for hydrogen feed system	12
3-3	Tank diameter vs surface area, volume, and weight of stored propellant	16
3-4	Total and incremental tank weights vs propellant weight (Spherical Tank)	17
3-5	Mean temperature difference as a function of absorptivity, emissivity, and distance from sun	21
3-6	Rate of occurrence of punctures vs shield thickness	24
3-7	Required beryllium shield thickness vs the product of exposed surface area and exposure time for various probabilities of puncture	26
3-8	Shield weight vs propellant weight	27
3-9	Paraboloid reflector cross section	29
3-10	Efficiency definitions for SOHR-SET system	32
3-11	Mirror-absorber efficiency vs ratio of cavity entrance to sun's image diameter	35
3-12	Mirror efficiency for paraboloid concentrators with small surface deviations	36
3-13	Mirror-absorber efficiency vs cavity temperature parameter for various levels of angular surface deviation	38
3-14	Concentrator diameter vs weight	40
3-15	Mirror diameter parameter vs absorber thermal power	41
3-16	Mirror diameter parameter vs thrust	42
3-17	Thrust coefficient and energy efficiency vs Reynolds number	44
3-18	Nozzle throat Reynolds number parameter vs stagnation temperature for hydrogen	46

ILLUSTRATIONS (cont)

Figure		Page
3-19	Nozzle throat Reynolds number parameter vs frozen flow specific impulse for hydrogen	47
3-20	Nozzle energy efficiency vs thrust for $I_{sp} = 500, 800$ sec	48
3-21	Variation of nozzle energy efficiency with mirror size	50
3-22	Thermionic diode performance vs emitter temperature	53
3-23	Solar energy thermionic generator	54
3-24	Thermal conductivity, density, and heat of fusion of mixtures of molybdenum and ceramic oxides	63
4-1	Change in cavity opening vs distance from sun	65
4-2	Integral SOHR-SET cavity design concept	67
4-3	Modes of heat transfer from cavity to diode emitter	71
4-4	Integral regenerative and radiation cooled diode heat rejection system	75
4-5	Thrust and electrical power output vs mirror size for a system with 100 percent thermal recovery	79
6-1	Solar cavity absorber-thermionic generator assembly	98
7-1	Hohmann transfer ellipse for chemical rocket	104
7-2	Coast ellipse for SOHR-SET	104
7-3	Time of powered flight vs initial thrust acceleration	105
7-4	Distance from sun at instant of thrust termination vs initial thrust acceleration	107
7-5	Power plant mass fraction vs initial thrust acceleration	108
7-6	Propellant mass fraction vs initial thrust acceleration	109
7-7	Payload plus structure mass fraction vs initial thrust acceleration	111
7-8	Total mission time vs initial thrust acceleration	112
7-9	Period of coast ellipse vs initial thrust acceleration	113
7-10	Aphelion distance of coast ellipse vs initial thrust acceleration	114
7-11	Propellant mass ratio (M_p/M_o) vs specific impulse (I_{sp}) for SOHR-SET, arc jet, and ion engines	120
7-12	Critical initial thrust acceleration (a'_o) vs specific impulse (I_{sp})	122

ILLUSTRATIONS (cont)

Figure		Page
7-13	Power plant mass ratio (M_w/M_o) vs initial thrust acceleration (a_o) for SOHR-SET, arc jet, and ion engines	124
7-14	Payload plus structure mass ratio ($M_l + M_s/M_o$) vs initial thrust acceleration (a_o) for SOHR-SET, arc jet, and ion engines	126
7-15	Synchronous orbit mission time (t_l) vs initial thrust acceleration for SOHR-SET, arc jet, and ion engines	127

TABLES

3-1	Properties of select mixtures of the stable ceramic oxides	60
3-2	Physical properties of the stable ceramic oxides	61
6-1	Summary of system performance characteristics	96
7-1	Engine Parameters	101
7-2	Propellant mass ratios	119
7-3	Critical initial thrust acceleration	123
7-4	Power plant specific weight and thrustor efficiency	123

1. INTRODUCTION

At the earth's mean distance from the sun, the solar flux in space is 130 watts/sq. ft., and as the sun is approached, this value increases as the inverse of the square of the distance from the sun. Therefore, it is natural to examine ways of utilizing this energy for propulsion and power for space missions in the solar system. One of the promising approaches is to convert solar energy directly into heat, then utilize the heat in energy conversion devices. This study considers the case of the conversion of solar energy into heat, then utilizing this heat for electric power generation and propulsion by means of a hybrid engine.

The general problem areas which must be coped with in such a hybrid engine design arise as a consequence of thermodynamic, vehicle integration, geometric, and space environmental considerations. Thermodynamic considerations are such that to achieve high efficiencies, the system must be operated at high temperatures. As the temperature increases, gas diffusion, metal sublimation, and similar problems become more severe. The net result is that the operating life-time of such systems dictates the limiting temperature. The importance of geometric considerations arises from the fact that there are performances losses due to collector surface inaccuracies, and errors in the location of an isothermal cavity absorber. With such considerations in mind, it is evident that high precision mirror technology is necessary. Until recently, mirror technology was inadequate for building the mirrors required for high temperature systems. However, EOS now fabricates 5-foot diameter mirrors having performance characteristics approaching perfect mirrors. Further, EOS is studying a 30-foot rigid mirror design, and has built elements for a 44-foot unfurlable solar collector. One of the major uncertainties which affect the future of solar power systems using collectors is the effect of the space environment on the collector surface. Studies have been made which show that the problem may not be a serious one. However, there is still apprehension over the effects of the apparently fluffy meteoroids on the mirror surface. Work is currently in progress, which is planned to provide space experiments to evaluate this potential problem.

The Solar Hydrogen Rocket-Solar Energy Thermionic System (SOHR-SET) has five major components.

1. A hydrogen storage and feed system.
2. A solar collector and orientation system
3. A cavity heat exchanger and thermal regeneration system.
4. Thermionic diodes.
5. Rocket nozzles.

Solar energy is concentrated by a light weight, all metal parabolic reflector which may range in diameter from 5-feet to 40-feet or more, depending upon the thrust and power requirements for the particular mission.

In operation, solar radiation is reflected into a cavity absorber having an aperture diameter approximately 1 percent of the collector diameter. This black body cavity encloses a refractory metal heat exchanger through which hydrogen gas circulates. If required, the cavity may incorporate material for thermal energy storage. External to the cavity is a mechanism for control of flux entering the cavity. Of the radiation that enters the cavity, a fraction of it is re-radiated through the cavity entrance, and a fraction is lost through the cavity walls. By far the largest portion is absorbed, however, either by the diode system, or by the hydrogen gas. Of the heat going to the diodes, a fraction (approximately 10 percent) is converted into electrical energy and the remainder is rejected, partially or totally for preheating of the incoming hydrogen flow depending upon the particular design. The incoming hydrogen flow is further heated in the cavity, and expanded through a nozzle for propulsion.

EOS has developed light weight cavities which have been operated in conjunction with light weight mirrors at temperatures as high as 4500°R for extended durations. These cavities were fabricated from rhenium, molybdenum, and tungsten. The cavities normally maintain gas temperatures between 3000-4000°R, corresponding to a specific impulse of from 600 to 800 seconds, depending upon the size of the system involved. EOS has recently demonstrated the feasibility of the solar hydrogen rocket propulsion concept on Air Force Contract No. AF 04(611)-8181, with the operation of a ground demonstration model.

The incorporation of a thermionic system with a solar hydrogen rocket appears to be a logical technological development. Progress in thermionic diode technology has been accelerated, and is now at the point where application to actual systems should be contemplated.

Thermionic diodes at present have low thermal efficiencies, hence, in practice from 5-10 times the electrical power delivered must be rejected as heat. Thus, a considerable amount of waste heat is available for utilization. The combined system described herein utilizes this waste heat for propulsion, thereby significantly improving the effective thermal efficiency of the overall system.

The SOHR-SET hybrid system differs from the individual SOHR or SET systems, only by the fact that there is a common cavity, and a thermal preheat/recovery system. A very important feature of the system is the capability of operating as a thermionic power generation system even after propulsion ceases.

2. SUMMARY AND RECOMMENDATIONS

The objective of this program was to perform a study of a combined solar hydrogen propulsion and electric power system for space applications. The study was initiated on 17 May 1963 under Contract NAS 7-231 and completed over a period of six (6) months. This final report includes all of the work performed during the program.

The study includes a performance analysis of the components which comprise the system, a design analysis of the combined cavity-absorber, a preliminary design for a 24 hour satellite system, and mission studies to define performance characteristics for comparative propulsion systems (electric and chemical) for a solar probe mission and several earth orbit transfer cases. In general, the analyses support the feasibility of the concept and define the design constraints imposed on the system when utilizing a combined solar cavity-absorber for both propulsion and power generation. The use of thermal energy storage for orbital applications has been evaluated and although its use may introduce serious compromises in optimizing cavity configuration, by causing increased thermal losses, its overall value to the system places it in an essential category particularly for maintaining isothermal operation of the propulsion and power subsystems. The system shows considerable promise for solar probe missions where transit times comparable to chemical rockets are indicated and relatively high payload mass fractions (comparable to high I_{sp} electric rockets) appear achievable. Another application which is attractive for the solar propulsion and power system is the transfer of a large communications satellite from a 300 n m parking orbit to a 24 hour synchronous orbit and then utilizing the electric power output of the thermionic diodes to operate the communication payload. The remainder of this section is devoted to a summary of results in the body of the report and recommendations for future work in support of the system concept.

2.1 Summary of Results

An analysis was conducted of the propellant storage and feed system requirements for liquid hydrogen. It was concluded that a non-vented system, using thermal leakage into the tank for pressurization, would be optimum for most missions particularly those of longer duration. The requirements for the storage system in terms of pressure tankage, thermal insulation, and meteoroid shielding as a function of propellant weight and mission duration are presented in Section 3.1. Of significance is the large reduction in meteoroid shielding from earlier estimates, as a result of the more recent Explorer XVI data.

A general analysis of mirror-absorber efficiency η_{m-a} was performed for paraboloidal concentrators as a function of cavity temperature and distance from the sun. Graphical results presented in Section 3.2 permit estimation of mirror-absorber efficiency over a wide range of operating conditions, including the effect of surface inaccuracies on performance. At the temperatures of interest (3500 - 4500 ^{o}R) in the cavity, values of η_{m-a} in the range of 70-75 percent appear feasible in space near the earth. The results can also be used to estimate the changes in physical parameters necessary to maintain constant efficiency, temperature, or power at various solar distances. Graphical plots are also presented for the cavity thermal power and maximum thrust available as a function of mirror size.

A brief analysis of the influence of nozzle Reynolds No. and thrust level on performance was completed. The results are based on recent experimental data and related theory, and indicate the relative nozzle energy efficiencies η_n that can be anticipated for various thrust levels and Reynolds No. The results are most significant and indicate that if an upper limit on cavity temperature is chosen, consistent with available materials, the actual specific impulse attainable for very small nozzles (thrust = 0.01 - 0.1 lbs) is about 600 sec. For larger systems (thrust $\approx$ 1.0 lbs) with nozzles operating at reasonable Reynolds No. (Re $\approx$ 10,000), actual specific impulses of 750 - 800 sec. appear feasible based on the same criteria for limiting temperature. These results are presented in a graphical form in Section 3.3 of the report.

The energy storage requirements are examined for various orbital applications and it is concluded that thermal energy storage is superior to presently available electrochemical systems for this application. A survey of the current technology in TES materials is presented, and the performance in watt-hours/lb for various modifications to the bare material is included. On the basis of available information, a TES matrix consisting of compacted and sintered 3 B_eO-2 MgO granules which have been coated with vapor deposited tungsten or rhenium, is suggested as optimum for energy/weight and thermal conductivity considerations.

A study of the combined cavity absorber was completed, including consideration of the influence of cavity entrance, hydrogen heat exchanger, thermionic diodes, and thermal energy storage on the design constraints imposed on the system. An analysis of the thermodynamics of the combined system is presented in Section 4 and the relationship between thermal power input, thrust and electrical power output is determined for various operating conditions. Under typical operating conditions, with superheat for high I_{sp} thrusting, only about 5-7 percent of the total energy absorbed can be converted into electrical power. Graphical plots of electrical output power and thrust are presented as a function of collector diameter and I_{sp}. The hydrogen diffusion problem is analyzed in some detail and criteria for compatibility with the thermionic diodes are established in terms of diffusion rates and equilibrium pressure in the cavity.

A preliminary design of a SOHR-SET system was completed for a 24 hour synchronous satellite. A Centaur booster vehicle delivering an 8500 lb gross weight space craft in a 300 n m orbit was assumed. The SOHR-SET system consists of four (4) modules each consisting of a 9-1/2 diameter solar collector and (16) converter thermionic generator cavity absorber. The design incorporates TES material for continuous (isothermal) operation during transfer from the low altitude orbit to the 24 hour orbit. At an I_{sp} of 700 sec. the system is capable of producing about 0.8 lbs of thrust at the 300 n m orbit and almost 1.2 lbs of thrust at the 24 hour orbit, making possible a transfer time of 30 - 40 days. The results indicate that the propulsion system can deliver a 3300 lb payload to the synchronous orbit and then provide 2200 watts of electrical power from the thermionic power system to operate a communication system. Included in Section 6, is a preliminary design cross-section drawing of the cavity absorber showing the configuration and location of the various elements.

Several missions which appear of interest for the SOHR-SET system, were analyzed to determine performance characteristics and the results were compared with electric thrustors and chemical rockets. A solar probe mission starting from a 300 n m parking orbit around the earth to a coast ellipse passing within 0.3 AU of the sun was studied. The results are very favorable and indicate that payload mass ratios of about 0.25 - 0.30 are attainable for mission times of 100 days with the availability of significant levels of electrical power. Similar studies were performed for orbit transfer missions and the results comparing the performance of solar propulsion, ion engine, arc jet, and a chemical rocket are presented in Section 7. Graphical plots of propellant mass ratio, payload mass ratio, and mission duration are provided for comparison. In general, the SOHR-SET combination appears competitive with and in many cases superior to other propulsion systems for the missions reported, particularly where electrical power is required in transit or at the destination.

2.2 Recommendations

The utilization of a SOHR-SET propulsion and power system for the 24 hour orbit satellite appears to be a particularly suitable and useful application. While the results of this preliminary study indicate the technical feasibility of the concept, experimental verification of certain critical areas is essential to assure the logical future development of the system. Therefore, the following phases of work are recommended to provide information of a basic nature to support the development of a combined cavity-absorber.

2.2.1 Hydrogen Diffusion

As discussed in the report, hydrogen diffusion through refractory materials at temperatures up to 2500°K may be a critical problem. Available information on the subject is limited to data on molybdenum at lower temperatures ($< 1800^{o}K$) and some theoretical models for extrapolation to higher temperatures. Since the ultimate feasibility of the concept is dependent of certain diffusion criteria, it is recommended that an experimental research program be initiated to determine the diffusion characteristics of hydrogen through tungsten, rhenium, and other alloys of interest at temperatures up to $2500^{o}K$. This study should also consider the influence of the crystal structure; bar stock, rolled plate, vapor deposition, etc., and other pertinent processing history on the diffusion properties.

2.2.2 Thermal Energy Storage

The most promising TES concept appears to be the sintered matrix of vapor deposited tungsten on 3 BeO - 2 MgO pellets, all encapsulated in a tungsten-rhenium container. This approach offers relatively high capacity (watt-hours/lb) with reasonable thermal conductivity. However, the feasibility of the concept is dependent on the effectiveness of the thermal bonds throughout the matrix and the stability of the compact during thermal cycling. These factors will determine the magnitude of temperature drop and its variation with time. Therefore, it is recommended that a research program be undertaken to fabricate the sintered TES matrix and incorporate a capsule of the material on the emitter of a thermionic diode of the type under development for the Jet Propulsion Laboratory for the SET program. This experimental vehicle should be tested with electron bombardment heating at temperatures up to $2200^{o}K$ and heat fluxes up to 200 watts/cm^2 to determine effective thermal conductivity and temperature drop. Thermal cycling should also be included to evaluate the stability of the structure with time.

2.2.3 Cavity Absorber Development

Upon completion of the basic work described previously, a combined cavity-absorber incorporating thermionic diodes, hydrogen heat exchanger and thermal energy storage matrix should be designed, fabricated, and tested for performance characteristics. The tests during this phase should be conducted in a laboratory vacuum system utilizing electron bombardment heating as the energy source. The scope and nature of any subsequent solar testing should be based on the results of the laboratory test program.

3. PERFORMANCE ANALYSIS OF COMPONENTS

The SOHR-SET System is best suited to a class of missions intermediate between chemical and electric propulsion systems. Characteristic of the SOHR-SET system mission capabilities is low thrust, high specific impulse, and large payloads in low gravitational fields at the expense of flight time. Since the propulsion aspect requires the storage of large volumes of liquid, (the SOHR aspect of the system requires large mass fractions) then cryogenic storage considerations must be taken into account. Furthermore, since large areas are involved, and long flight times are anticipated, micrometeorite protection may become a significant factor.

3.1 Propellant Storage and Feed System

The following sections deal with the analysis of the tankage weight required for typical SOHR-SET missions.

3.1.1 Vented and Non-Vented Systems

The designer of a liquid hydrogen storage system for prolonged space missions must decide very early on the disposition of hydrogen boil-off due to heat leakage into the system. If it is decided to vent the system to prevent excessive pressure build-up, then the best that can be done is to optimize the boil-off-insulation relationship. For long duration missions, the penalty is severe. An earlier EOS study (RTD-TDR-63-1085, "Research and Development Studies to Determine Feasibility of Solar LH_2 Propulsion System.") gives an analysis of the boil-off penalties involved in a vented system. This study will be based on a non-vented system design concept.

In a non-vented system thermal leakage must be transferred from the body of the stored hydrogen to the existing liquid.

This can be done by throttling the hydrogen, then passing the wet mixture of liquid hydrogen droplets and saturated vapor through coils immersed in the storage tank. Figure 3-1 is a schematic of a non-vented system using stored gas pressurization. The system consists of the shield, tank plus suitable valves, regulators, expulsion bladder, throttling and warm-up coils, and other items. A schematic of the fuel tank wall is shown at the bottom of the page. The tank wall consists of the internal skin which contains the pressurized hydrogen, a layer of thermal insulation, a meteoroid shield, and a tank support structure.

The tank wall shown should not be considered as being the final form, since more optimized arrangements are possible. The interlacing of several layers of insulation and shielding is a distinct possibility as far as a lower weight design is concerned. However, optimization of the structure is uncalled for until further knowledge is gained concerning the meteoroid environment, and the relative merits of one type of shield configuration over the other is determined.

Figure 3-2 is the Temperature-Entropy diagram for liquid hydrogen controlled vaporization. State 1 corresponds to the condition of bulk storage. The fluid is stored under saturated liquid condition at a pressure p_1, temperature T_1, and enthalpy h_1. At state 2, the fluid is throttled resulting in a decrease in pressure and temperature, and an increase in quality X_2. At state 3 the fluid is recirculated through the fuel tank where its enthalpy is increased to h_3, and its quality increased to X_3. At state 4 the fluid is throttled resulting in a decrease in pressure and temperature and an increase in quality from X_3 to the near saturated vapor. At state 5 the saturated vapor enters the first of a set of heat exchangers. Here it is warmed up sufficiently so that it can be handled easily in a flow control system. Another function of this

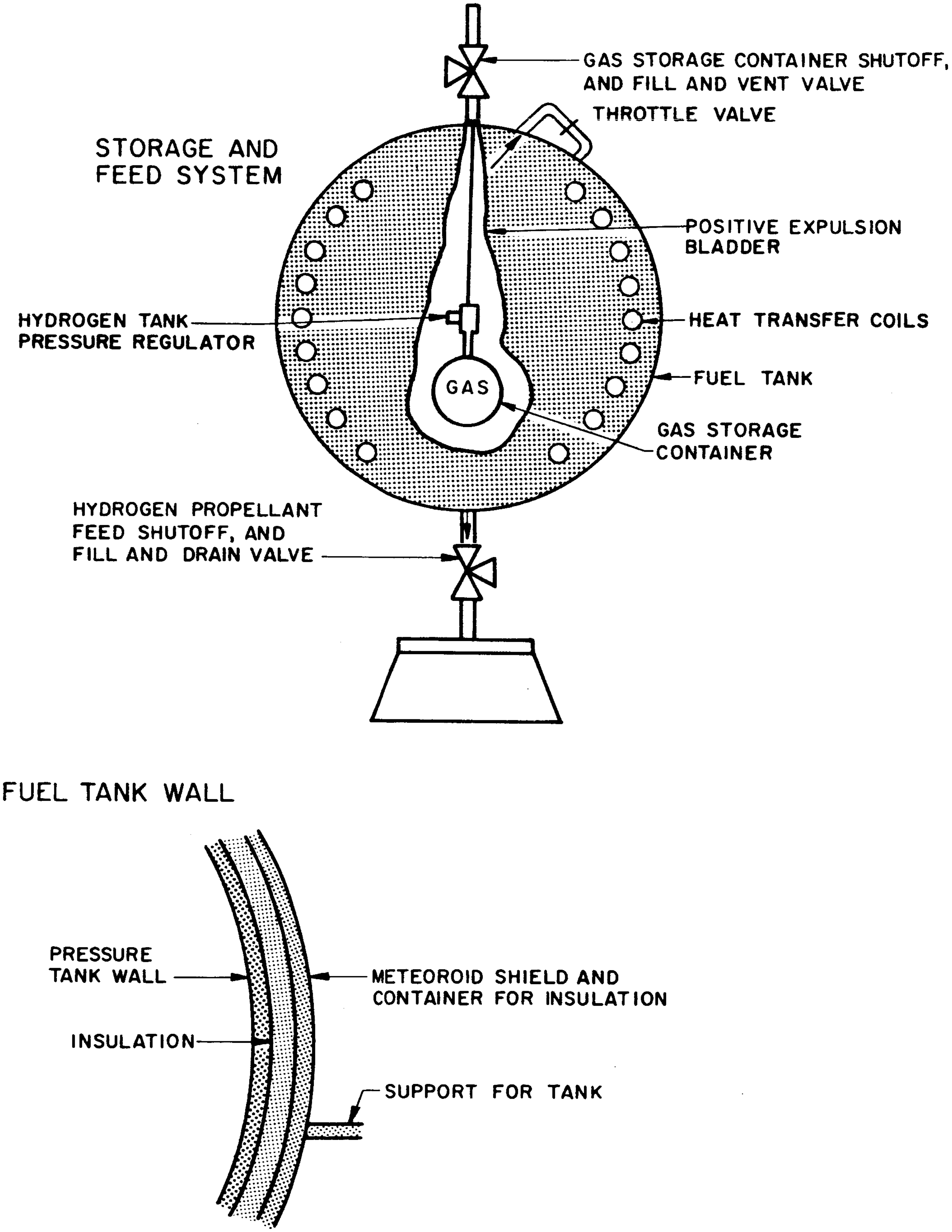
STORAGE AND FEED SYSTEM
GAS STORAGE CONTAINER SHUTOFF, AND FILL AND VENT VALVE
THROTTLE VALVE
POSITIVE EXPULSION BLADDER
HYDROGEN TANK PRESSURE REGULATOR
HEAT TRANSFER COILS
FUEL TANK
GAS
GAS STORAGE CONTAINER
HYDROGEN PROPELLANT FEED SHUTOFF, AND FILL AND DRAIN VALVE
FUEL TANK WALL
PRESSURE TANK WALL
METEOROID SHIELD AND CONTAINER FOR INSULATION
INSULATION
SUPPORT FOR TANK

FIG. 3-1 PROPELLANT STORAGE AND FEED SYSTEM

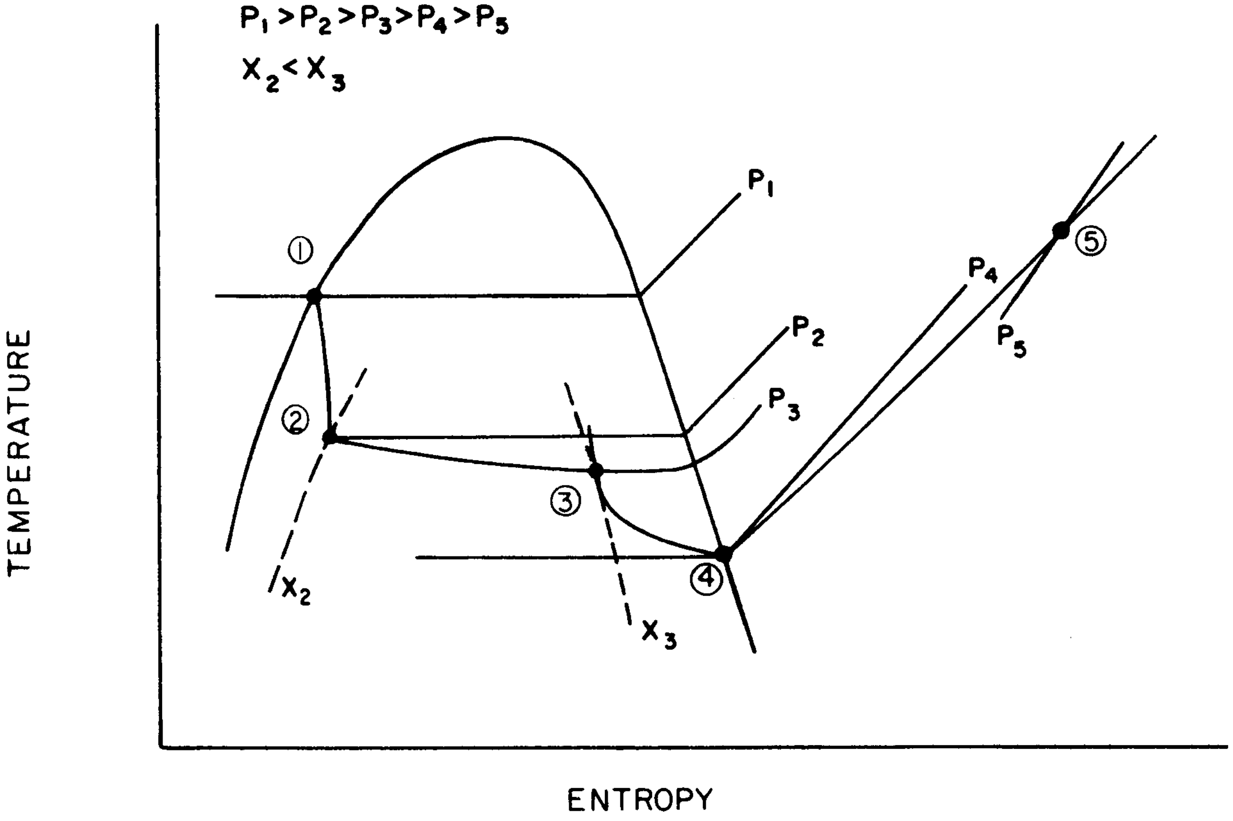
$P_1 > P_2 > P_3 > P_4 > P_5$
$X_2 < X_3$
①
②
③
④
⑤
P_1
P_2
P_3
P_4
P_5
X_2
X_3
TEMPERATURE
ENTROPY

FIG. 3-2 TEMPERATURE ENTROPY DIAGRAM FOR HYDROGEN FEED SYSTEM

heat exchanger is to make absolutely sure that no hydrogen droplets remain, thereby providing single phase vapor in the higher temperature exchangers.

The thermal leakage to the hydrogen will depend upon, among other things, the distance of the space craft from the sun. In actual practice we can anticipate several situations. We can envision the space-craft being on a mission so that at the end, it is closer to the sun than at any other point. We can also imagine this space-craft being further away from the sun at the end of the mission. There is the additional case in which space-craft is alternately close to and far removed from the sun, and finally, the craft may always be approximately the same distance from the sun. For the case in which the space-craft is closest to the sun at the end of the mission, the insulation must be adequate enough so that at the end of the mission the thermal leakage is not greater than the rate which enthalpy is being removed from the system by the exiting hydrogen stream. This being the case the hydrogen leaving the tank will always be of a quality less than 1, except at the end of the mission when its quality is 1, so that the first heat exchanger will in essence also be a vaporizer. For the case where the space vehicle is closest to the sun at the beginning of the mission, then the reverse case is true. Then again the first heat exchanger will also be a vaporizer. For the case where the spacecraft is alternately near and far removed from the sun, then the design must be for the point of closest approach to the sun, and for parts of the mission again the first heat exchanger will also be a vaporizer. The only missions on which the exiting hydrogen stream will be essentially a saturated vapor will be those in which the spacecraft distance from the sun remains approximately constant.

3.1.2 Propellant Storage, Feed System Geometry, Structural Requirements

The propellant storage and feed system weight consists of propellant weight plus the weight of the structure used to store and feed the propellant. The propellant weight consists of the hydrogen consumed for propulsion plus the propellant remaining after mission completion. The structure weight consists of pressure tank insulation and meteoroid shield. The pressure tank weight is derived partly from internal pressure considerations, and partly from other incremental factors described below. Since thermal insulation can serve as a meteoroid shield, and a meteoroid shield does have some thermal insulating properties, then the sum of the weights of thermal insulation and meteoroid shield should be optimized for a particular mission. In this analysis this has not been done.

As stated above $W_{sys} = W_{prop} + W_{struc}$ (3-1)

where

W_{sys} = system weight

W_{prop} = propellant weight

W_{struc} = storage and feed system structure weight

The make-up of the structure weight is as follows:

$$W_{struc} = W_v + W_i + W_m \tag{3-2}$$

where

W_i = weight of the insulating layer

W_m = weight of the meteoroid shield

$W_v = W_{press} + \Delta W_{ba} + \Delta W_{sa} + W_e + \Delta W_{sf}$

The contributions to W_v are defined as follows:

W_{press} = theoretical weight of propellant tank due to internal gas pressure.

ΔW_{ba} = incremental weight of propellant tank due to boost phase acceleration.

ΔW_{sa} = the incremental weight of tank due to state of the art restrictions in material gauges.

ΔW_{e} = incremental weight due to weight of expulsion bladder and associated structure of expulsion system (valves, regulators,etc.)

ΔW_{sf} = incremental weight due to factor of safety requirements

The propellant tank geometry is arrived at by placing two constraints upon the over-all problem of propellant tank design. It is assumed that the tank has the minimum surface to volume ratio, and that it is adaptable to present booster vehicle systems. The minimum area is necessary, not only to reduce the overall weight of the tank, but also to reduce the weight of meteoroid shielding, thermal insulation, and the necessary structural supports. Figure 3-3 shows the relationship between tank diameter, the tank volume, surface, area, and weight of hydrogen.

Figure 3-4 shows the propellant tank weight for storage of liquid hydrogen at 50 psia using Ti-5Al-2.5 Sn alloy. Note that the upper curve W_v gives the propellant tank weight, whereas the lower curves are plots of the theoretical minimum value, and the incremental values.

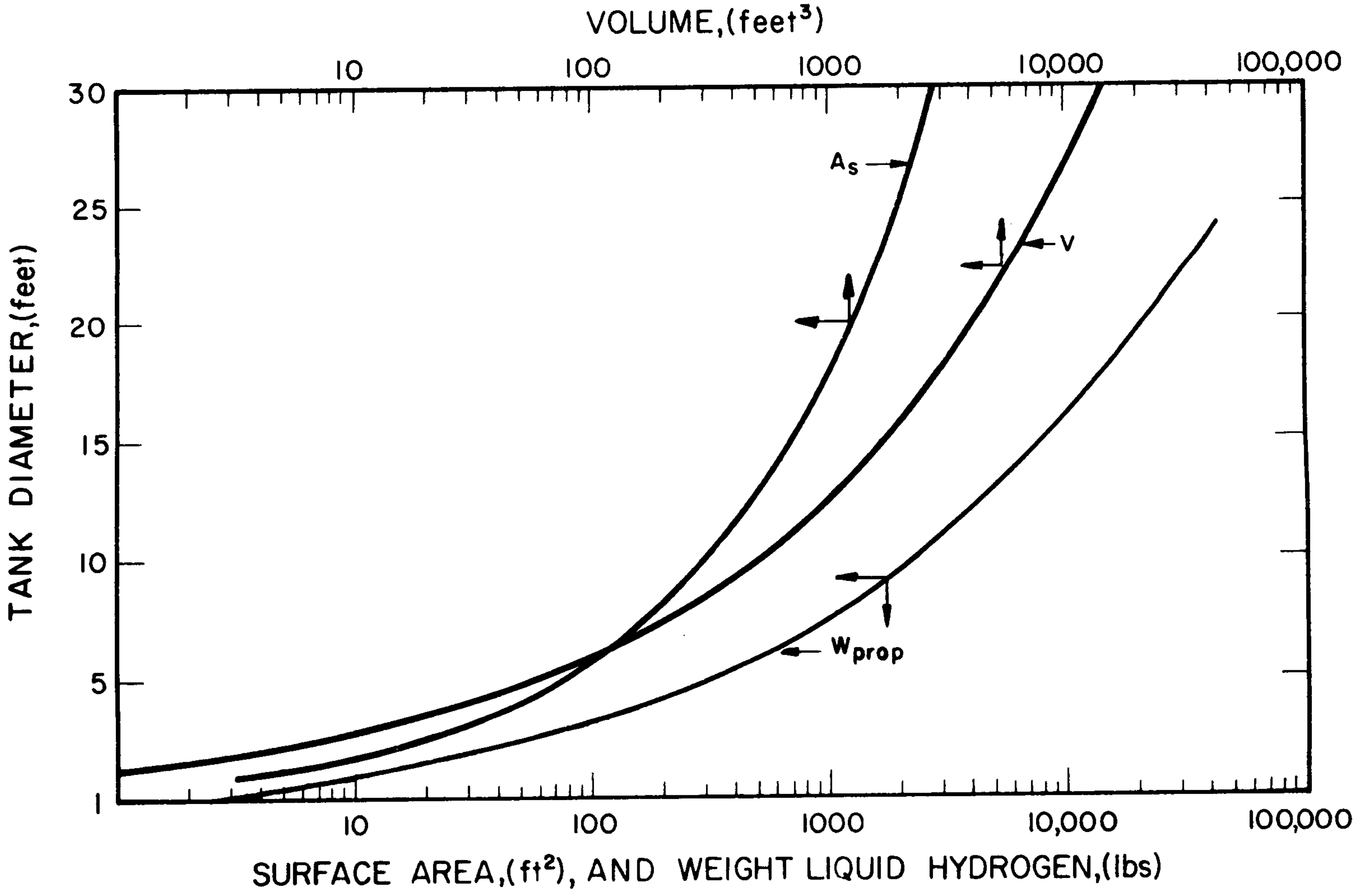

FIG. 3-3 TANK DIAMETER VS SURFACE AREA, VOLUME, AND WEIGHT OF STORED PROPELLANT

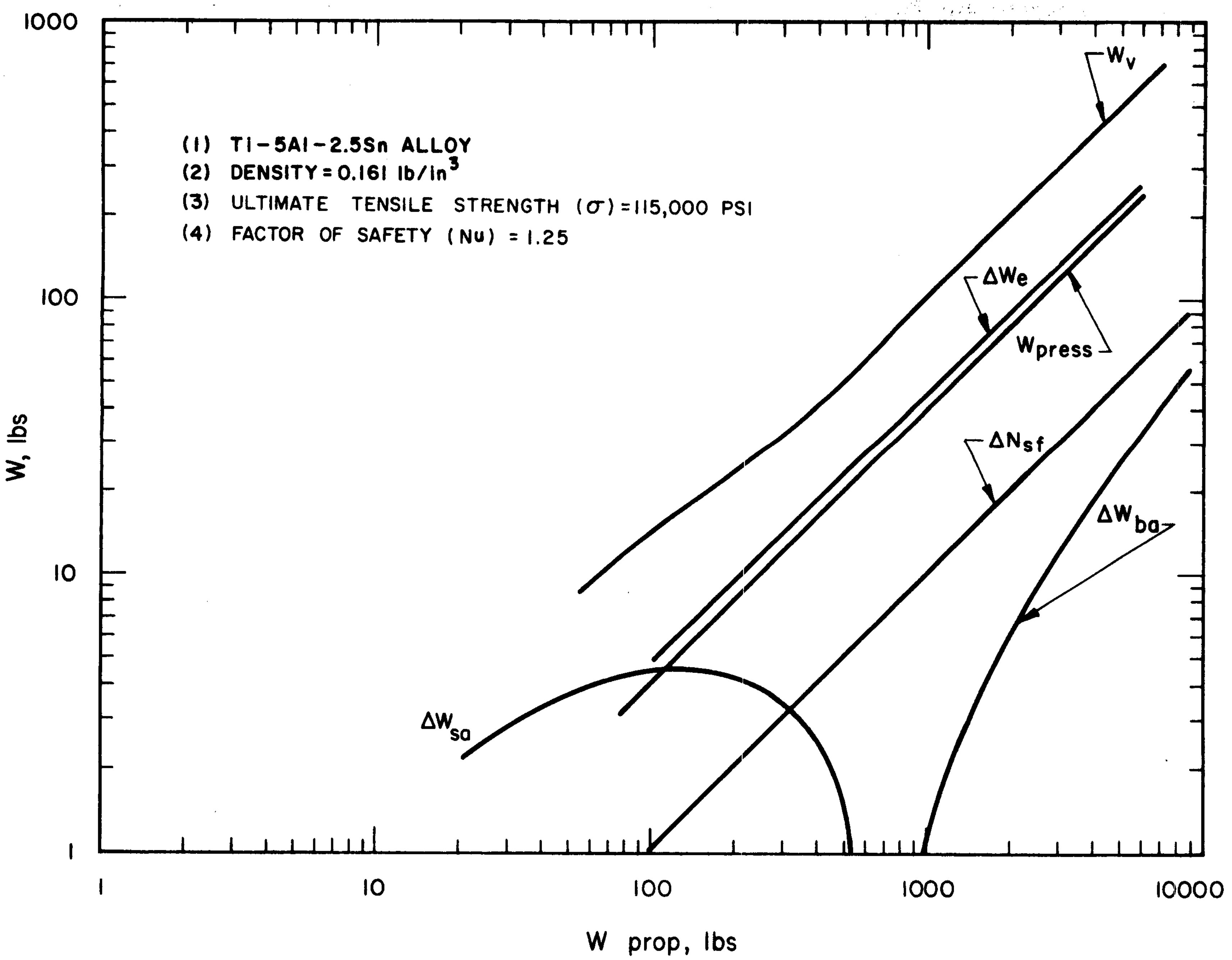

FIG. 3-4 TOTAL AND INCREMENTAL TANK WEIGHTS VS PROPELLANT WEIGHT (Spherical Tank)

3.1.3 Insulation Requirements

The heat transferred to a space vehicle in a solar system depends on its location in space relative to the sun and the other planets, and also on its motion and orientation relative to them.

For the case of a non-venting system the propellant consumption rate is equal to the boil off rate at the point of closest approach of the space vehicle to the sun. Another assumption is that the propellant is always in contact with the tank skin.

Let

X = insulation thickness

ΔT = temperature difference between insulation skin temperature and liquid hydrogen bulk temperature.

k = thermal conductivity

A_s = surface area of liquid hydrogen storage vessel.

F = thrust

D_m = mirror diameter

ρ = insulation density

Therefore, the heat input rate per unit area = $k\ \Delta T/X$

The total heat input is now

$$\int_{\text{surface}} (k/X)\ \Delta T\ dA_s \tag{3-3}$$

We will now define a mean temperature difference as equal to

$$\int (\Delta T/A_s)\ dA_s \tag{3-4}$$

Therefore, the total heat input rate is equal to

$$A_s\ k\Delta T_m/X \tag{3-5}$$

and the boil off rate is equal to the total heat input rate divided by the heat of vaporization.

Hence the boil off rate is equal to

$$A_s K \Delta T_m / (X H_v) \tag{3-6}$$

where H_v is the heat of vaporization of the liquid hydrogen. Let I_{sp} be the specific impulse of the hydrogen leaving the cavity. Therefore the propellant consumption rate is

$$\dot{w} = F/I_{sp} \tag{3-7}$$

Equating the boil off rate to $\dot{w}$ and noting that the insulation weight w_i is equal to $\rho A_s X$ we obtain

$$w_i = \rho A_s^2 k \Delta T_m I_{sp} / (H_v F) \tag{3-8}$$

Thermal conductivity values for evacuated laminated foil insulation have been reported as follows:

$$k = .012-.05 \times 10^{-3} \text{ btu/hr-ft-}^{\circ}\text{R}, (36^{\circ}-530^{\circ})\text{R}$$

$\rho = 7.5$ lbs./ft^3. To obtain high performance space vacuum conditions must be maintained between the many layers of aluminum foil, aluminized mylar, or like insulation.

The mean temperature difference will now be estimated for an orbit around the earth, and for any point in space as a function of the distance from the sun. First we define the following terms:

Q_e = rate of thermal radiation emitted from an arbitrary element of tank surface.

Q_v = the rate of transmission of thermal leakage to the stored hydrogen.

Q_a = the rate at which radiation is being absorbed by arbitrary element of the tank surface. This radiation may be direct solar radiation emission radiation or reflected radiation.

H = solar radiation (solar constant) = H_o/r^2

α_{ss} = total surface absorptivity for solar radiation

ϵ_s = the surface emissivity of the tank.

σ = Stefan-Boltzmann constant

T = tank surface temperature.

f = radiation per unit area of tank surface due to reflection and reradiation from earth.

θ = angle that incident energy ray makes with the normal to tank surface.

dA = element of tank surface area.

then by making an energy balance about a surface element

$$(f + \alpha_{ss} H \cos \theta)\ dA = (T_s - T_i)\ (k/x)\ dA + \epsilon_s \sigma T_s^4\ dA \qquad (3\text{-}9)$$

Let $\Delta T = T_s - T_i$

and further note that for the system under consideration

$$\frac{k}{x} \approx 0$$

and

$$T_s\ (\theta) = \left[(f + \alpha_s \cdot \cos \theta\ H_o/r^2)/\epsilon_s \sigma \right]^{1/4} \qquad (3\text{-}10)$$

for case where $f \rightarrow 0$, i.e., the spacecraft is far removed from the earth, then

$$\Delta T_m = \int T\ dA_s/A_s = 2.60 \times 10^2 \left[(\alpha_s/\epsilon_s r^2)^{1/4} - T_i/2 \right] \qquad (3\text{-}11)$$

Eqn. 3-11 is plotted in Fig. 3-5 as curve 4. Curve 1 may be used as an indication of the mean surface temperature for the situation where both reflection and reradiation from earth are important. The above calculations are based on the assumption of negligible lateral thermal conductivity in the insulation.

Over the range of low surface temperatures, 0-600°R, surface coatings composed of organic base white paints have achieved α/ϵ ratios as low as 0 . 1.(see Ref. H.S. London, T.N. Edelbaum, Et.al., "Mission Capabilities of Ion Engines" NAS 5-935. Phase II-Final Report) Hence the minimum mean temperature difference for near earth missions seems to be about 130°F. At .3 AU from the sun, the mean skin temperature difference will be 280°F.

Let W_{HO} = Initial weight of Hydrogen

D = tank diameter

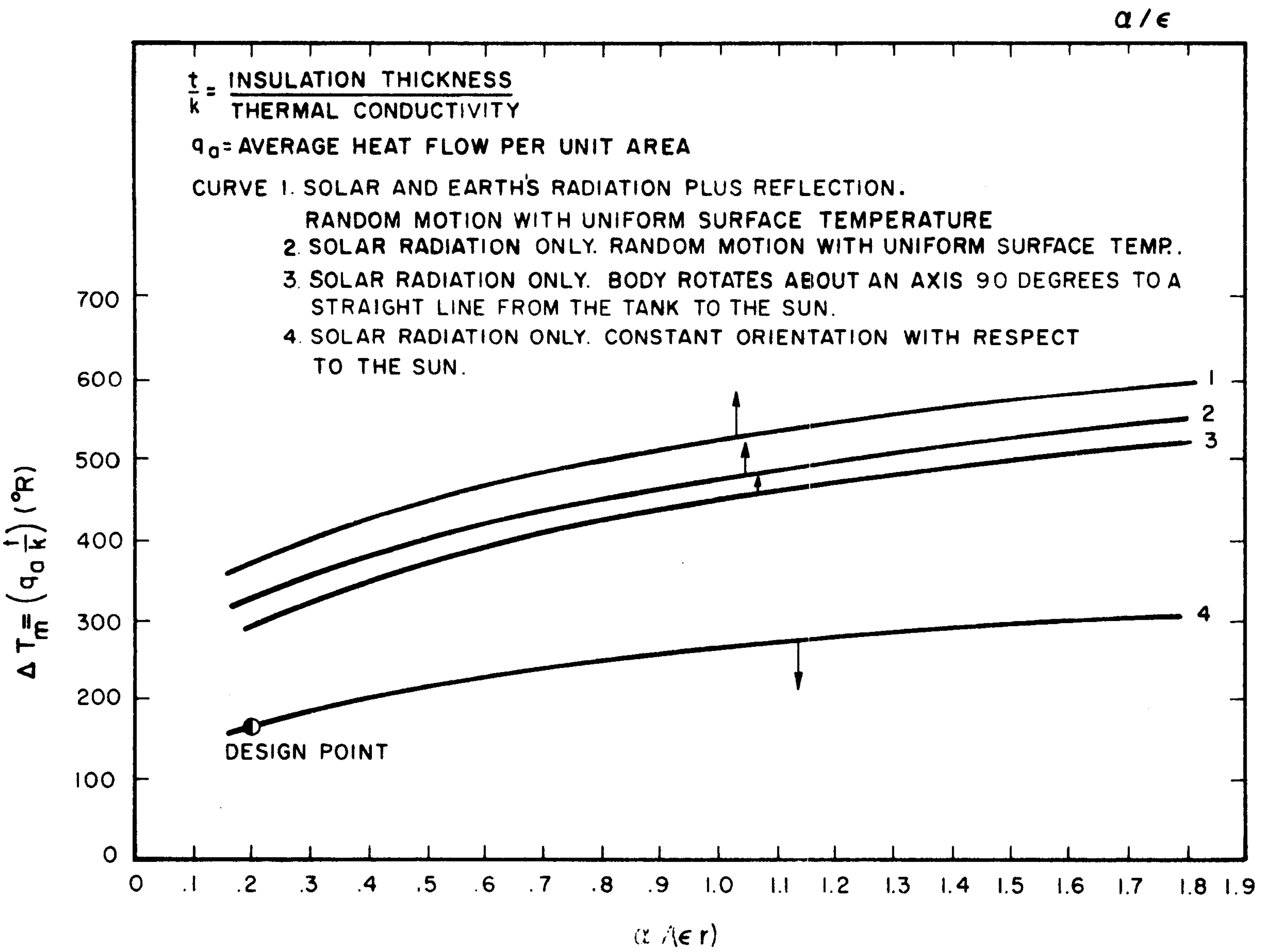

FIG. 3-5 MEAN TEMPERATURE DIFFERENCE AS A FUNCTION OF ABSORPTIVITY, EMISSIVITY, AND DISTANCE FROM SUN

Then from the equations developed earlier it follows that;

$$Wi/W_{HO} = 3\ k\ I_{sp}\ \rho/(H_v \rho_H F\ D)\ \left[520 \left(\frac{\alpha s}{\epsilon_s r^2} \right)^{1/4} - T_i \right] \quad (3\text{-}12)$$

$T_i = 30^{o}R$

$k = 2 \times 10^{-5}$ Btu/hr-ft.-°F

$I_s = 800$ sec.

$\rho_H = 4.4$ lb/ft.^{3}

$H_v = 195$ Btu/lb.

$\rho = 7.5$ lb/ft.^{3}

$\alpha_s/\epsilon_s = .1$

$$W_i/W_{HO} = [3.5 \times 10^{-5}/(FD)]\ [520\ (\alpha_s/\epsilon_s r^2)^{1/4} - T_i] \quad (3\text{-}13)$$

$$W_i/W_{HO} = [3.5 \times 10^{-5}/(FD)]\ [292\ (1/r^{1/2}) - T_i] \quad (3\text{-}14)$$

For r = 1

$$W_i/W_{HO} = [3.5 \times 10^{-5}\ /(FD)]\ [277\ (970 \times 10^{-5}/FD) - (.970 \times 10^{-2}/FD)] \quad (3\text{-}15)$$

In general, since Wi/W_{HO} depends on the spacecraft geometry (to determine reradiation) and on the spacecraft orbit, these considerations must be known before an accurate W_i/W_{HO} determination may be made. Fig. 3-5 does, however, indicate that nature of the problem. Once ΔT_m has been estimated, W_i may be found directly.

3.1.4 Meteoroid Shielding

Any vehicle operating in space for a prolonged period of time must be protected from meteoroid damage by a protective shield. Estimates of the meteoroid effects on the space structure depend on two sets of data, namely; the frequency with which the surface will be struck by a particle with a given size, velocity, direction, and composition, and the penetrating ability of a particle on a particular surface of a given thickness. Figure 3-6 gives penetration data for steel and aluminum as deduced from the works of Whipple and Bjork. Also include in Fig. 3-6 is penetration data based on the 1963 findings of Explorer XVI (J. C. Evvard, "How Much Future for Electric Propulsion?" Astronautics and Aerospace Engineering, August 1963. It should be noted that the Explorer XVI data were obtained only for penetrations of stainless steel material a few mils thick, and that extrapolation to material thickness of say 1/4 inch has yet to be verified. Note that the curve derived by assuming meteoroid densities of 0.5 gms per cm^3 forms an upper boundary for recent Explorder XIV data.

The effectiveness of the optical surface of the solar concentrator, and of the surface coatings used for structures and for the thermal protection of propellant tanks will be affected by the average depth of the surface coating destroyed by meteoroids. Analysis has shown that much less than 1 percent of the mirror surface will be affected. For long periods of time meteoroid punctures follow a random arrival, or Poisson distribution. This assumption is used to calculate the meteoroid shield weight necessary for prolonged space craft operation. We define P(n) as the probability that n punctures of a sensitive area A will occur in a given time λ. Assume that the shielding material is beryllium of density 0.066 lbs. per $inch^3$. From Figure 3-6, we can find the expected value of the

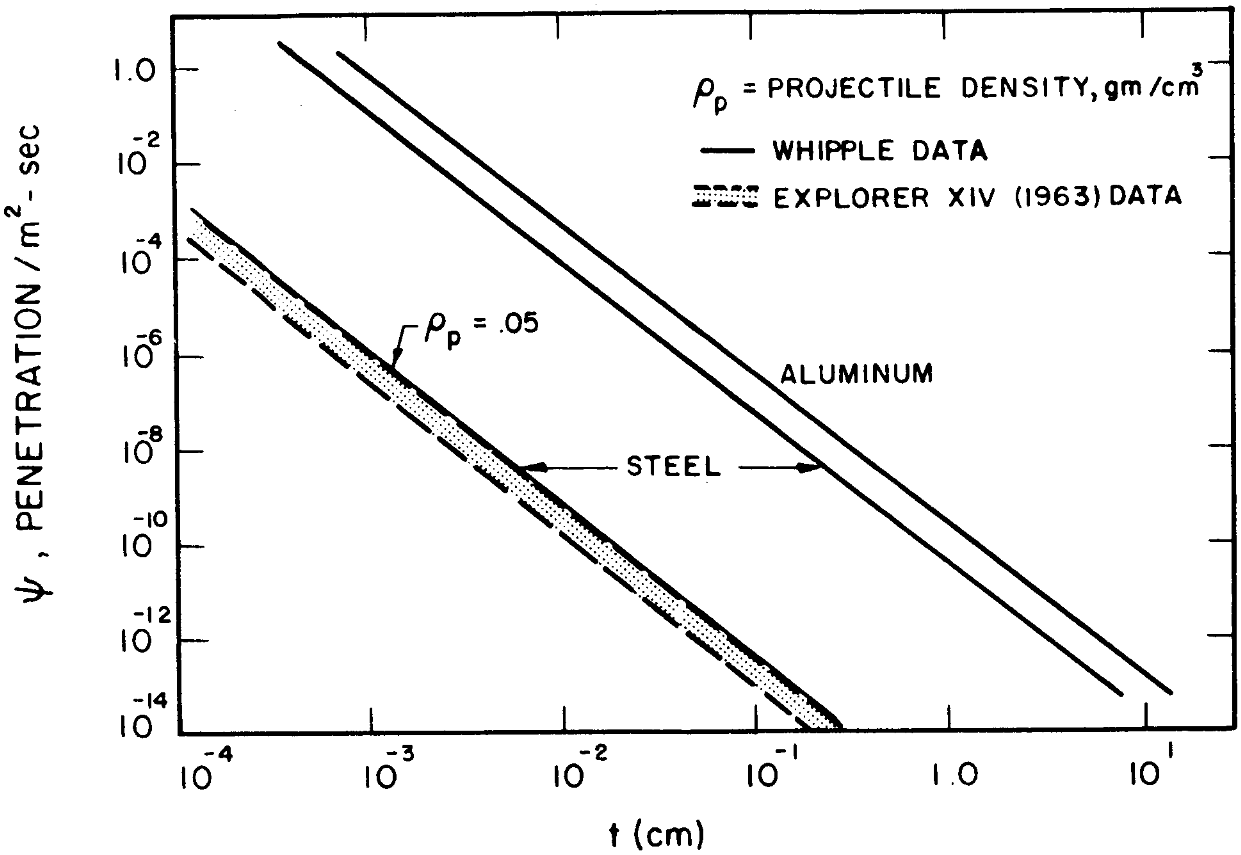

FIG. 3-6 RATE OF OCCURRENCE OF PUNCTURES VS SHIELD THICKNESS

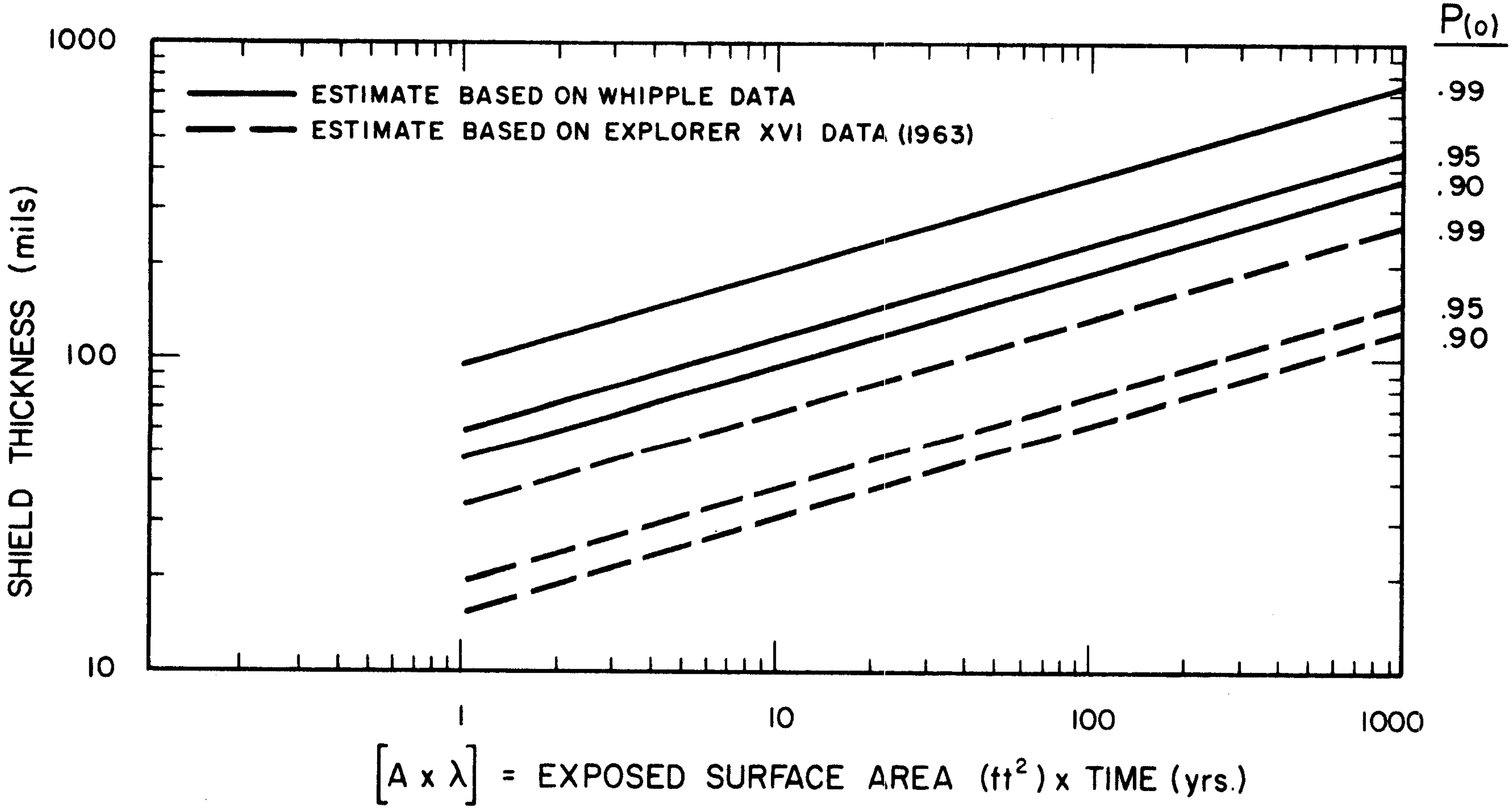

FIG. 3-7 REQUIRED BERYLLIUM SHIELD THICKNESS VS THE PRODUCT OF EXPOSED SURFACE AREA AND EXPOSURE TIME FOR VARIOUS PROBABILITIES OF PUNCTURE

number of punctures for any area or for a given time.

Ψ = number of punctures/m^2-sec
A = exposed area, m^2
λ = exposure time, sec.
t = thickness in mils

The expected value of the number of punctures is $\Psi A\lambda$, hence $P(n)$ and $P(0) = \exp-(\Psi A\lambda)$ are known. Since $\Psi_{beryllium} = 1.45 \times \Psi_{steel}$, the shield thickness for beryllium is expressed by

$$t = 23.5 \left[\frac{A\lambda}{1-P(0)}\right]^{0.3} \tag{3-16}$$

for values of $P(0) > 0.90$.

Figure 3-7 is the plot of the beryllium shield thickness required for preventing meteoroid penetrations, as a function of time. The required shield thickness based on Whipple's data, is approximately three times greater than the thickness based on Explorer XVI data.

Figure 3-8 gives a shielding requirement for various quantities of stored hydrogen. The shielding figures are based on the tank configuration discussed previously.

The results indicate that for a 90 percent survival probability of no penetrations, the meteoroid shield requirement based on the Explorer XVI data will be only about 6 percent of the propellant weight for a 100 day mission, and about 3 percent of propellant weight for a 10 day mission. Of course, if the design is based upon the earlier Whipple data, then the figures would be approximately three times larger.

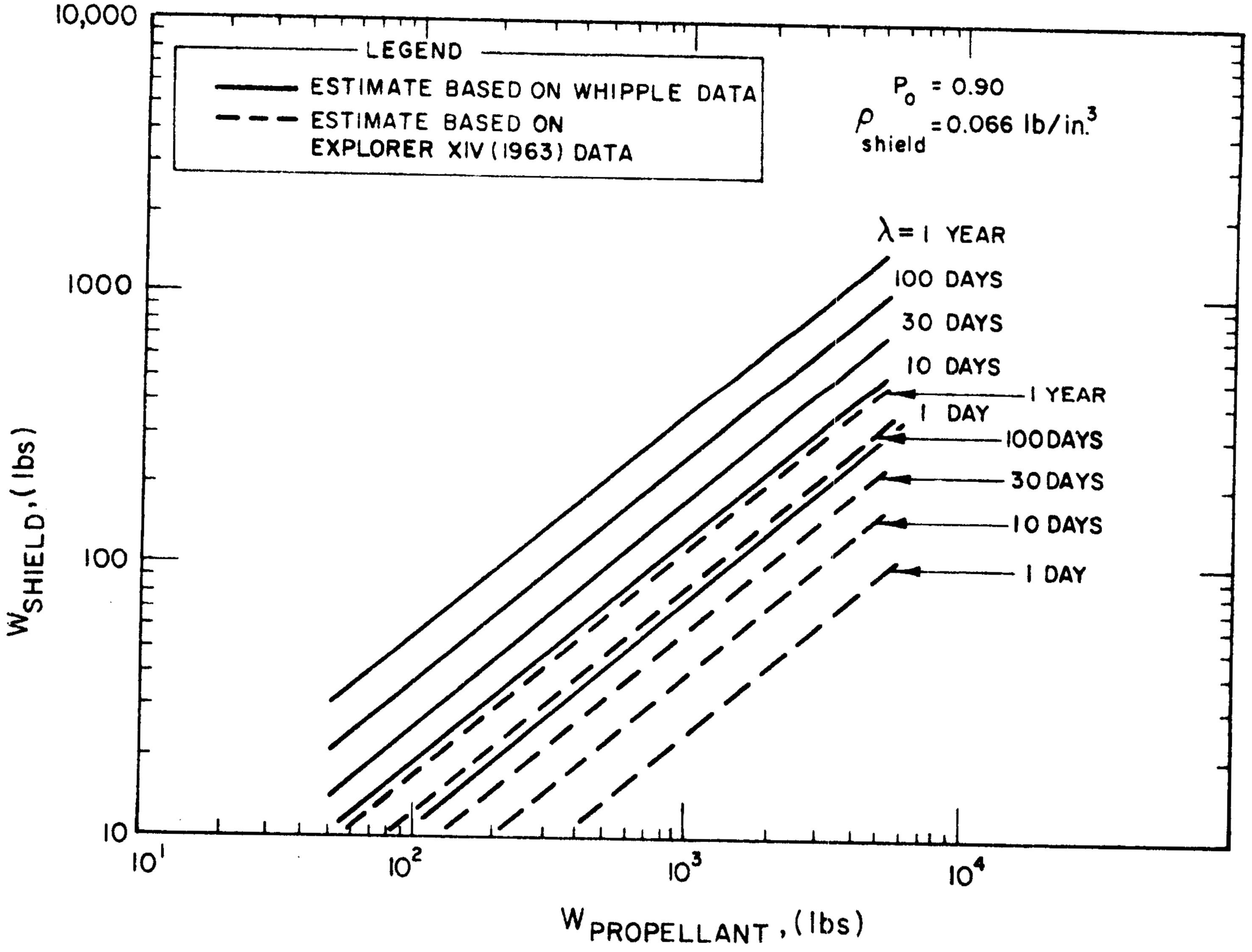

FIG. 3-8 SHIELD WEIGHT VS PROPELLANT WEIGHT

3.2 Collector-Absorber Characteristics

The paraboloidal reflector has been established as the most logical selection for the high-temperature SOHR-SET application. It is the only concentrator that allows the attainment of high temperatures at high efficiency. Figure 3-9 illustrates the cross section of a paraboloid reflector, as well as the shape of a theoretically ideal focal image.

The parameters of interest in the selection of a specific paraboloid concentrator are summarized below. Each parameter is closely related to the others, and each must be considered in a final selection.

1. Geometry
    a. Diameter
    b. Focal length
2. Accuracy
    a. Angular and linear surface deviations from true paraboloid.
    b. Figure distortion
3. Physical Characteristics
    a. Weight
    b. Type of fabrication techniques
    c. Folded volume
    d. Support members
    e. Unfolding mechanisms
4. Space Environmental Effects
5. Vehicle Integration
    a. Volume and dimension limits
    b. Interference with other vehicle functions

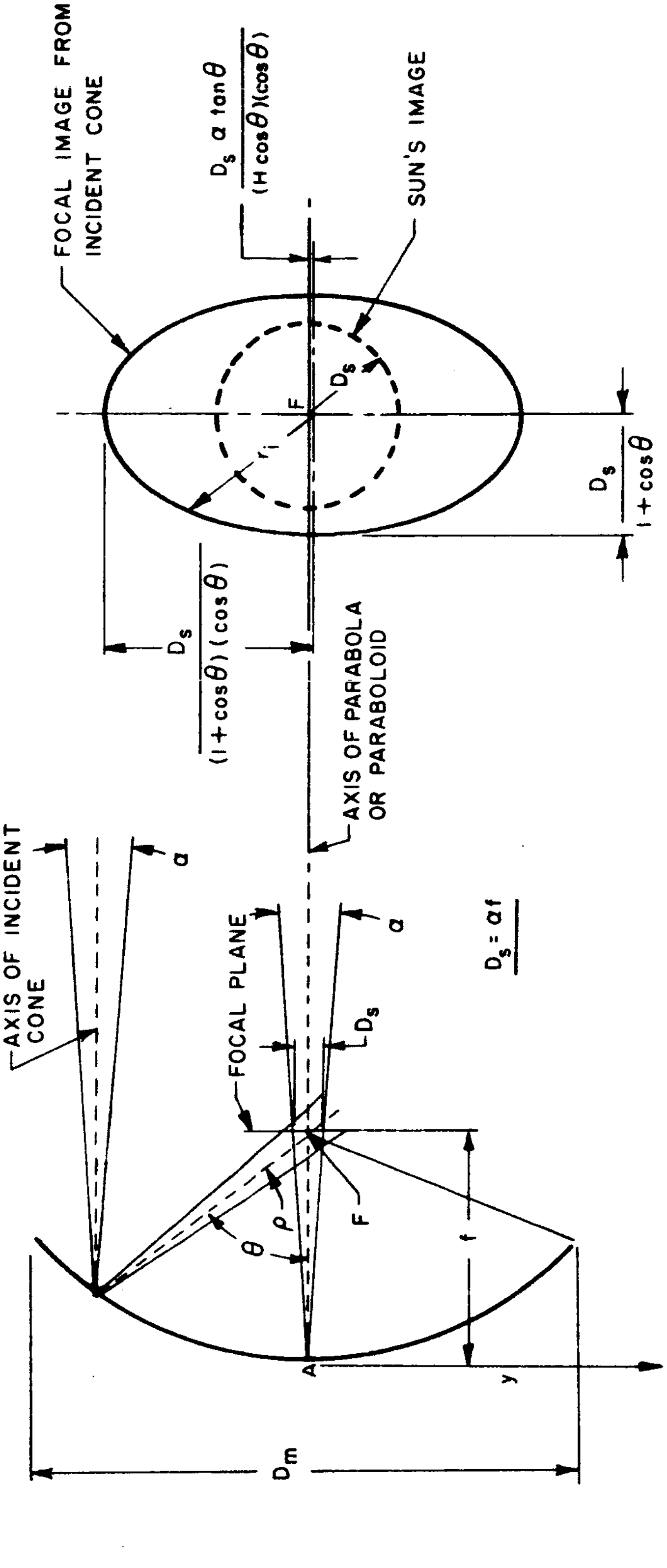
FOCAL IMAGE FROM INCIDENT CONE
$\frac{D_s \alpha \tan\theta}{(1+\cos\theta)(\cos\theta)}$
SUN'S IMAGE
F
D_s
r_1
$\frac{D_s}{1+\cos\theta}$
$\frac{D_s}{(1+\cos\theta)(\cos\theta)}$
AXIS OF PARABOLA OR PARABOLOID
AXIS OF INCIDENT CONE
α
FOCAL PLANE
α
$D_s = \alpha f$
D_s
θ
ρ
F
f
A
y
D_m

FIG. 3-9 PARABOLOID REFLECTOR CROSS SECTION

It can be shown that the only type of absorber that will result in high efficiency at high temperatures is a cavity where the emitting-surface area is much smaller than the absorbing-surface area. This condition reduces the fraction of energy reradiated from the cavity. Actual performance of flat-plate absorbers, based on presently available refractory materials, would be extremely poor, since absorptivity-emissivity values of less than 0.5 are normal for typical operating conditions. Another advantage of the cavity absorber is the design freedom afforded by its relative insensitivity to shape and size.

Analyses are available in the open literature that describe the performance obtainable from low-thrust systems as a function of thrusting time, exhaust velocity, powerplant specific weight, thrust, impulse, and other factors. These analyses have assumed that the powerplant specific weight is constant over the range of exhaust velocities of interest. This assumption is inaccurate in the case of solar propulsion. A further characteristic of solar power plants is that the specific weight will decrease as the spacecraft gets closer to the sun.

The specific weight of the powerplant for the solar-hydrogen propulsion system, increases as the hydrogen-exhaust velocity increases, thereby effectively limiting the practical exhaust velocities (specific impulse) that can be achieved. This weight increase is due to the efficiency drop at high temperatures, as explained in the following simplified analysis.

The powerplant specific weight is defined as:

$$\begin{aligned} \text{powerplant specific weight} &= \frac{\alpha}{\eta_{(r)}} \ (\text{lb/kw}) = \frac{\alpha}{\eta_{(r)}} \qquad (3\text{-}17) \\ &= \frac{Br^2}{H_o \eta_{(r)}} \ (\text{lb/kw}) \end{aligned}$$

where

$\eta_{(r)}$ = propulsion system efficiency as a function of distance from sun-decreases with increasing r.

α = effective weight of powerplant per kw of solar power incident on system.

β = effective lb/ft^2 of concentrator(including structural supports)

H = solar flux $kw/ft^2 = .130/r^2 \ kw/ft^2$

r = distance from sun in AU.

Several efficiencies associated with the solar-hydrogen rocket thermionic power plant are shown in Fig. 3-10. These are:

1. Mirror efficiency-the amount of solar radiation that is reflected onto the useful area of the absorber, divided by the amount of sunlight falling on the system.
2. Mirror-absorber efficiency-the amount of energy kept by the absorber after re-radiation losses divided by the amount of sunlight on the system.
3. Propulsion System Efficiency-the power in the propellant flow divided by the sunlight on the system.
4. System Efficiency-The sum of the power in the propellant flow plus the electric power output divided by the amount of sunlight on the system.

For preliminary calculations, it is assumed that the absorber, located at the focal plane of the concentrator, is a cavity designed so that the maximum amount of sunlight will enter the cavity without an excessive amount of re-radiation from the entrance. It can be shown, that the use of a combined flat-plate and cavity-type absorber, will result in higher efficiency than obtainable with a single cavity absorber. This improvement is significant for poor quality mirrors, and only a few percent better for an ideal concentrator.

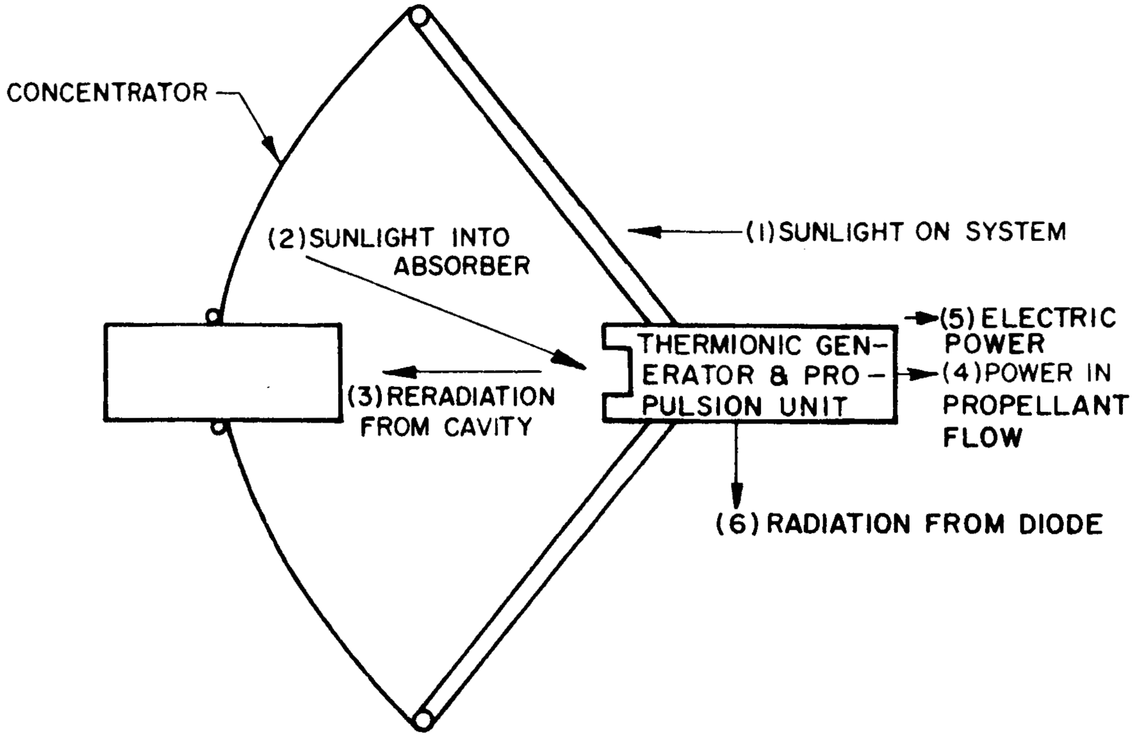
CONCENTRATOR
(2)SUNLIGHT INTO ABSORBER
(1)SUNLIGHT ON SYSTEM
(5)ELECTRIC POWER
THERMIONIC GENERATOR & PROPULSION UNIT
(4)POWER IN PROPELLANT FLOW
(3)RERADIATION FROM CAVITY
(6)RADIATION FROM DIODE

MIRROR EFFICIENCY $\eta_m = \frac{(2)}{(1)}$

MIRROR-ABSORBER EFFICIENCY $\eta_{m-a} = \frac{(2)-(3)}{(1)}$

PROPULSION SYSTEM EFFICIENCY $\eta = \frac{(4)}{(1)}$

SYSTEM EFFICIENCY $\eta_s = \frac{(4)+(5)}{(1)}$

FIG. 3-10 EFFICIENCY DEFINITIONS FOR SOHR-SET SYSTEM

The following nomenclature will be used in the analysis of mirror-absorber efficiency.

$A_{cav} \sigma T_{cav}^4 \epsilon_{cav}$ = re-radiation from cavity

η_{m-a} = mirror-absorber efficiency

η_m = mirror efficiency

A_{cav} = entrance area of the cavity

σ = Stephan-Boltzmann constant

T_{cav} = effective cavity re-radiation temperature

ϵ_{cav} = effective emissivity of cavity

H = solar constant at r

H_o = solar constant = 130 w/ft^2 at 1 AU

r = distance from sun, AU

A_m = mirror area (frontal)

P = electrical power output from diode

Q_{lost} = unavoidable heat losses due to radiation from cavity walls, etc.

Q_{rad} = thermal energy rejected by diode.

G = mass-flow rate of propellant

$\bar{C}_p$ = mean heat capacity of propellant

T_e = propellant exit temperature from absorber coils

T_o = propellant temperature at cavity inlet.

$r^{1/2}T$ = temperature parameter

η_N = nozzle energy efficiency

η_F = frozen flow efficiency

The equation describing the heat balance of the mirror-absorber combination are:

$$H_o A_m \eta_{m-a}/r^2 = H_o A_m \eta_m/r^2 - A_{cav}\ \sigma\ T_{cav}^4\ \epsilon_{cav} \tag{3-18}$$

or

$$\eta_{m-a} = \eta_m - \frac{\sigma\ \epsilon_c A_c r^2 T_c^4}{H_o A_m} \tag{3-19}$$

hence,

$$H_o A_m \eta_m/r^2 - A_{cav}\ \sigma\ \epsilon_{cav}\ T_{cav}^4 = Q_{lost} + P + Qrad + G\bar{C}_p(T_e - T_o) \tag{3-20}$$

The term $G\bar{C}_p\ (T_e - T_o)$ provides the power for thrusting, hence with power in watts, thrust in lbs. and I_{sp} in sec.;

$$H_o A_m \eta_{m-a}/r^2 = Q_{lost} = P + Q_{rad} + 21.8\ F\ I_{sp}/(\eta_N \eta_F) \tag{3-21}$$

In general, in this study we will assume $Q_{lost} = 0$, and during thrusting $Q_{rad} = 0$ will be the condition for total thermal recovery from the diodes. Hence, during thrusting with total recovery;

$$H_o A_m\ \eta_{m-a}/r^2 = P + 21.8\ F\ I_{sp}/(\eta_N \eta_F) \tag{3-22}$$

Later on a relationship will be derived for the nozzle energy efficiency (η_N) as a function of thrust (F).

Fig. 3-11 is a plot of mirror-absorber efficiency vs ratio of cavity entrance diameter to sun's image diameter. The curves are plots of η_{m-a} for a perfect concentrator with the temperature relationship ($r^{1/2}T_{cav}$) as a parameter. Similar curves may be derived for imperfect mirrors if η_m is known. Note that the optimum cavity entrance diameter decreases with increasing T_{cav}, in order to compensate for reradiation losses, and that for T_{cav} = constant, the optimum D_{cav}/D_m Will change with r. The curves are based on the assumption $\epsilon_{cav} = 1.0$ and are plotted against the parameter (D_{cav}/D_s). Figure 3-12 is a plot of mirror efficiency for imperfect mirrors. The imperfection is denoted by σ_Ψ, which is the standard

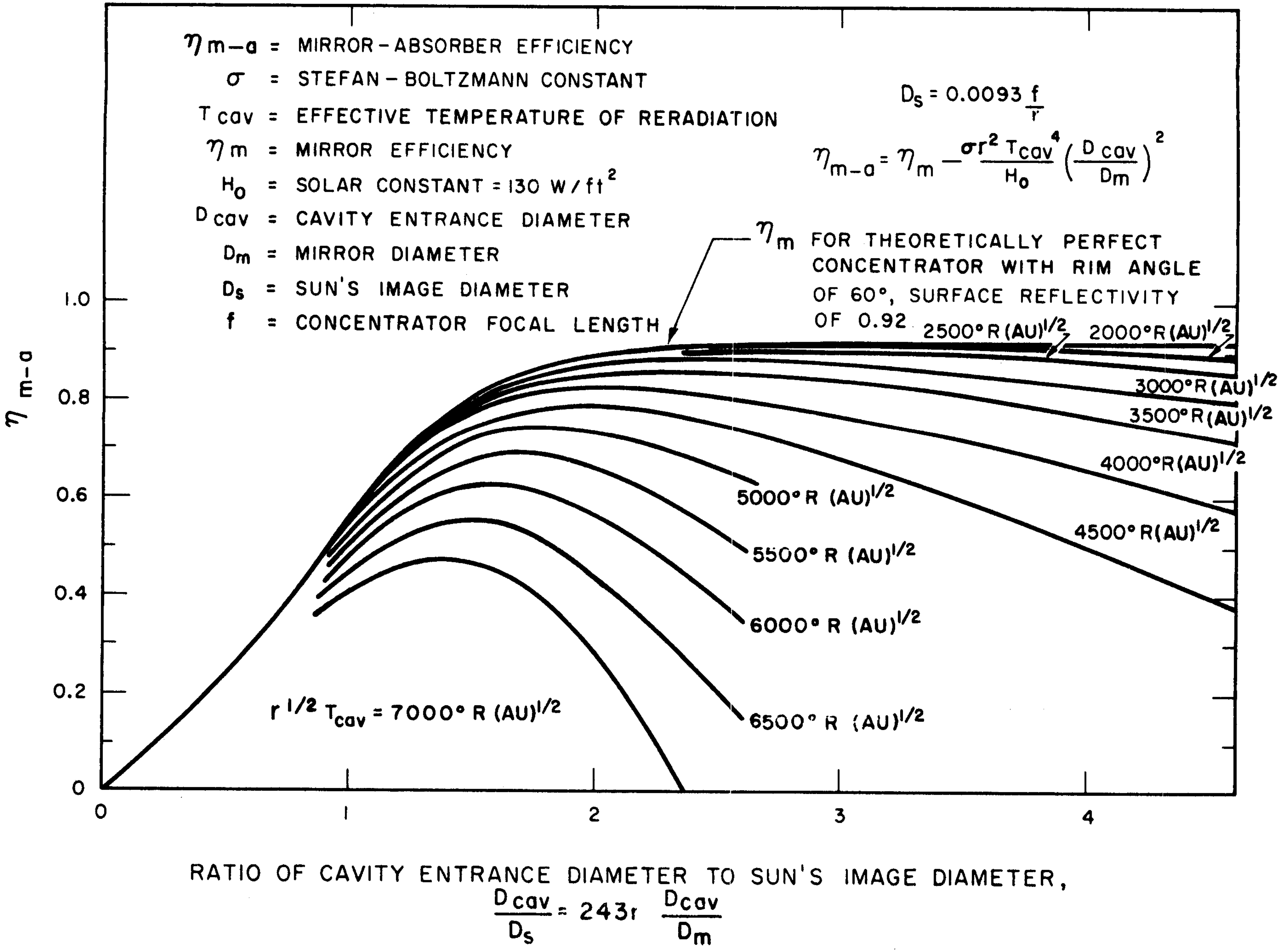

FIG. 3-11 MIRROR-ABSORBER EFFICIENCY VS RATIO OF CAVITY ENTRANCE TO SUN'S IMAGE DIAMETER

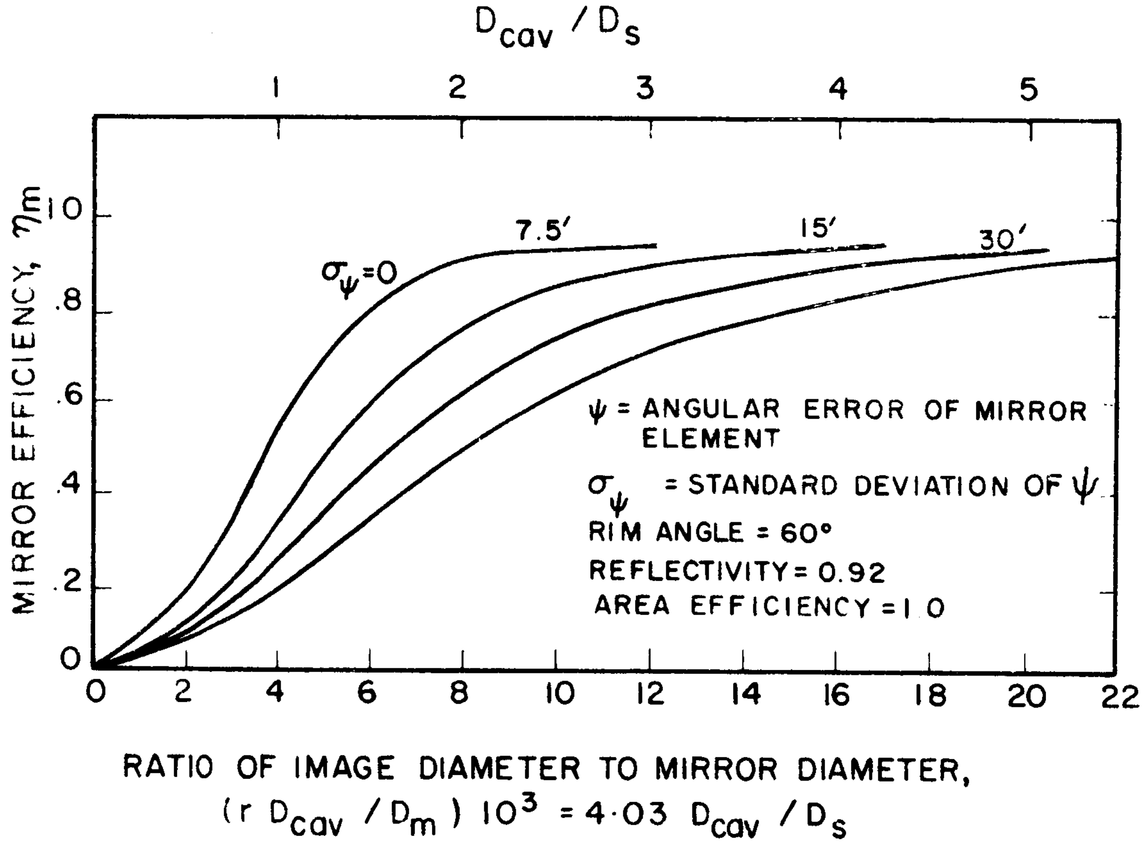

FIG. 3-12 MIRROR EFFICIENCY FOR PARABOLOID CONCENTRATORS WITH SMALL SURFACE DEVIATIONS

deviation of the mirror-surface angular error. The magnitude of the mirror surface error is assumed to be normally distributed and the standard deviation found accordingly. The mirror performance degrades rapidly and collectors $\sigma_\psi > 30'$ are not regarded as very suitable for solar hydrogen rocket propulsion. Since η_{m-a} decreases even further with increasing temperature, then high temperature systems will perform poorly if σ_ψ is excessive.

The mirror efficiency associated with any given paraboloidal concentrator is a function of the ratio of cavity-entrance diameter to the sun's image diameter. For a concentrator with a perfect surface, all the sun's energy will be focused into a cavity-entrance diameter that is about $2.8D_s$ where D_s is the sun's image diameter at the focal plane defined by

$$D_s = 2\ f \sin(\theta/2) = .0093\ f/r \qquad (3\text{-}23)$$

where

$\theta = 32'$ at $r = 1$ AU

D_s = sun's image diameter

f = focal length of concentrator

Figure 3-13 shows the maximum mirror-absorber efficiency for several paraboloidal concentrators as a function of cavity temperature, and illustrates the effect of various degrees of surface degradation. Case 1 is for an ideal concentrator with no surface obscuration and a reflectivity equal to 0.92 (the maximum obtainable with aluminum). Cases 2 and 3 are the resultant curves for values of 0.5 and 0.25 degrees for the angular deviation. As indicated earlier η_{m-a} is very small at high temperatures. Case 4 comes close to having a perfect surface geometry with a reflectivity of 0.88 instead of 0.92.

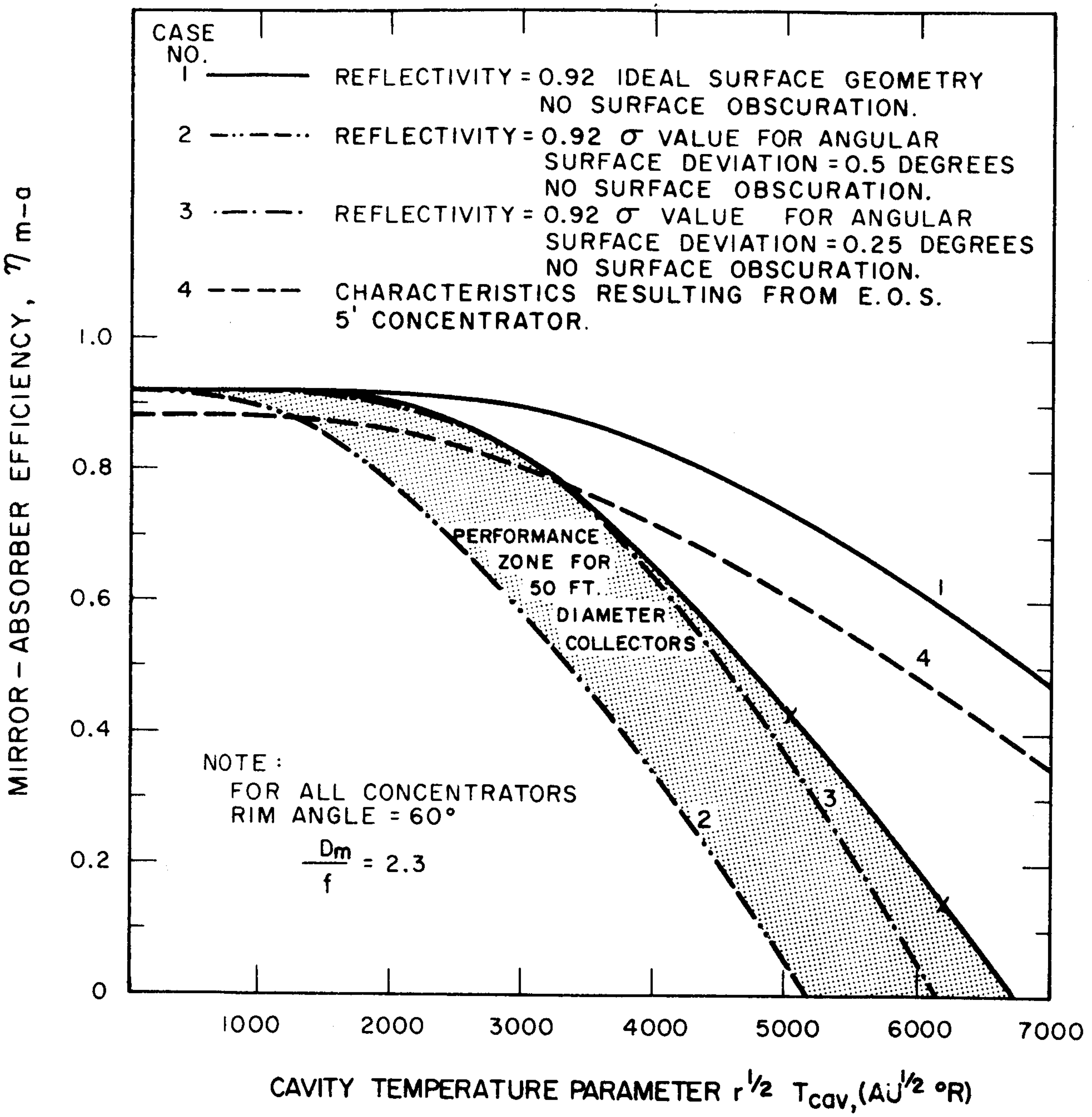

FIG. 3-13 MIRROR-ABSORBER EFFICIENCY VS CAVITY TEMPERATURE PARAMETER FOR VARIOUS LEVELS OF ANGULAR SURFACE DEVIATION

The effect of misorientation on collector-absorber efficiency becomes more serious at the higher cavity temperatures. A limit of about 30 min. of angular error is required to achieve acceptable efficiencies at cavity temperatures above 2000°K. The maximum rim angle, before performance becomes seriously degraded, is about 60°.

Specific weights of solar collectors at present appear to be about 0.5 lbs. per sq. ft. for units ranging from 5 feet to 40 feet in diameter. Figure 3-14 gives the weights of representative collectors as a function of diameter. Even though the rigid collector is the heaviest of them all, due to the accuracy inherent in its fabrication, it is able to deliver more energy at a higher temperature on a per unit weight basis than any of the other systems. It is likely that improved techniques and advanced materials may decrease the specific weight by a factor of two in the near future, if continued emphasis is placed on this area of development. It appears reasonable to anticipate that values of α in the range of 2-4 lbs. per kw will be achieved for relatively high performance space mirrors.

Fig. 3-15 is a plot of mirror size vs thermal cavity power. The plot is obtained from the relationship;

$$\text{Thermal Cavity Power} = 102\ \eta_{m-a}\ (D_m/r)^2 \text{ watts.} \qquad (3\text{-}24)$$

The rapid increase in mirror size for a correspondingly small increase in cavity thermal power for $r^{1/2}\ T_{cav} = 4700$ and $D_m > 40$ is characteristic of performance degradation that will result with large mirror systems at high temperatures, based on current projections of surface inaccuracies.

Fig. 3-16 is a plot of maximum thrust available vs mirror size. Curves are plotted for specific impulse values of 500 and 800 sec. The curves are a plot of the relationship

$$F = (4.68\ \eta_{m-a}\ \eta_N\ \eta_F / I_{sp})\ (D_m/r)^2 \qquad (3\text{-}25)$$

which is developed from the earlier derived results by setting P = 0.

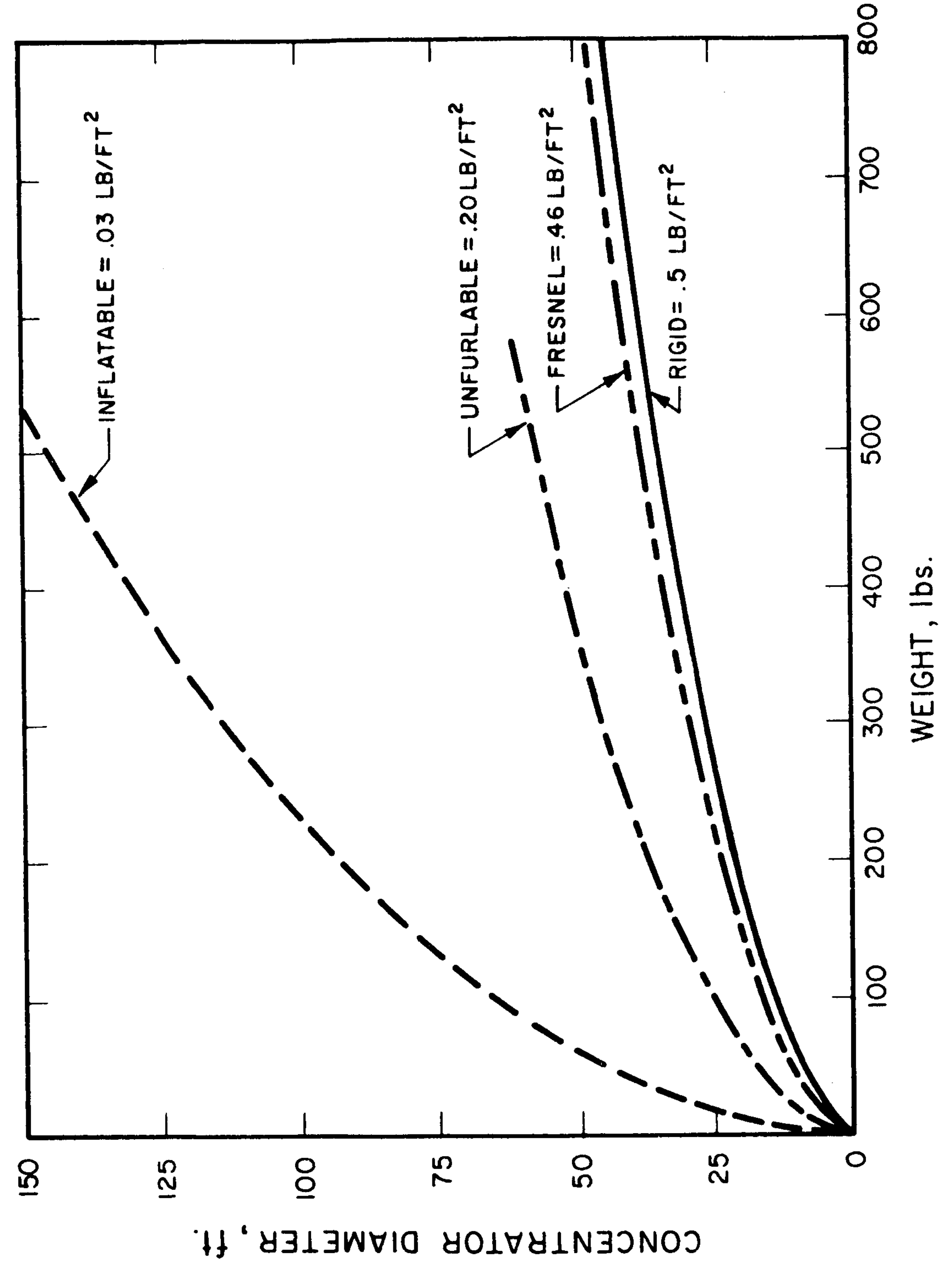

FIG. 3-14 CONCENTRATOR DIAMETER VS WEIGHT

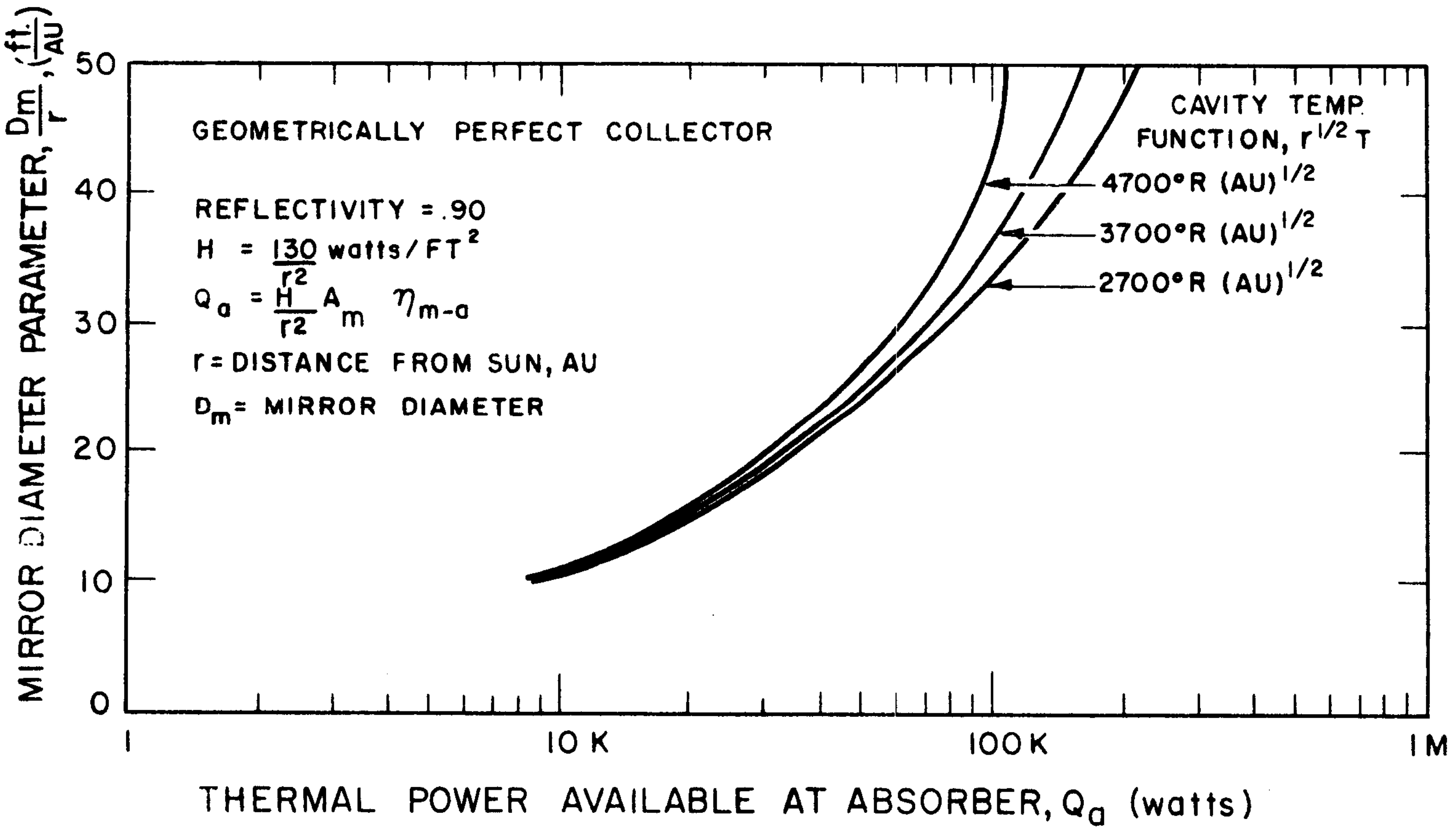

FIG. 3-15 MIRROR DIAMETER PARAMETER VS ABSORBER THERMAL POWER

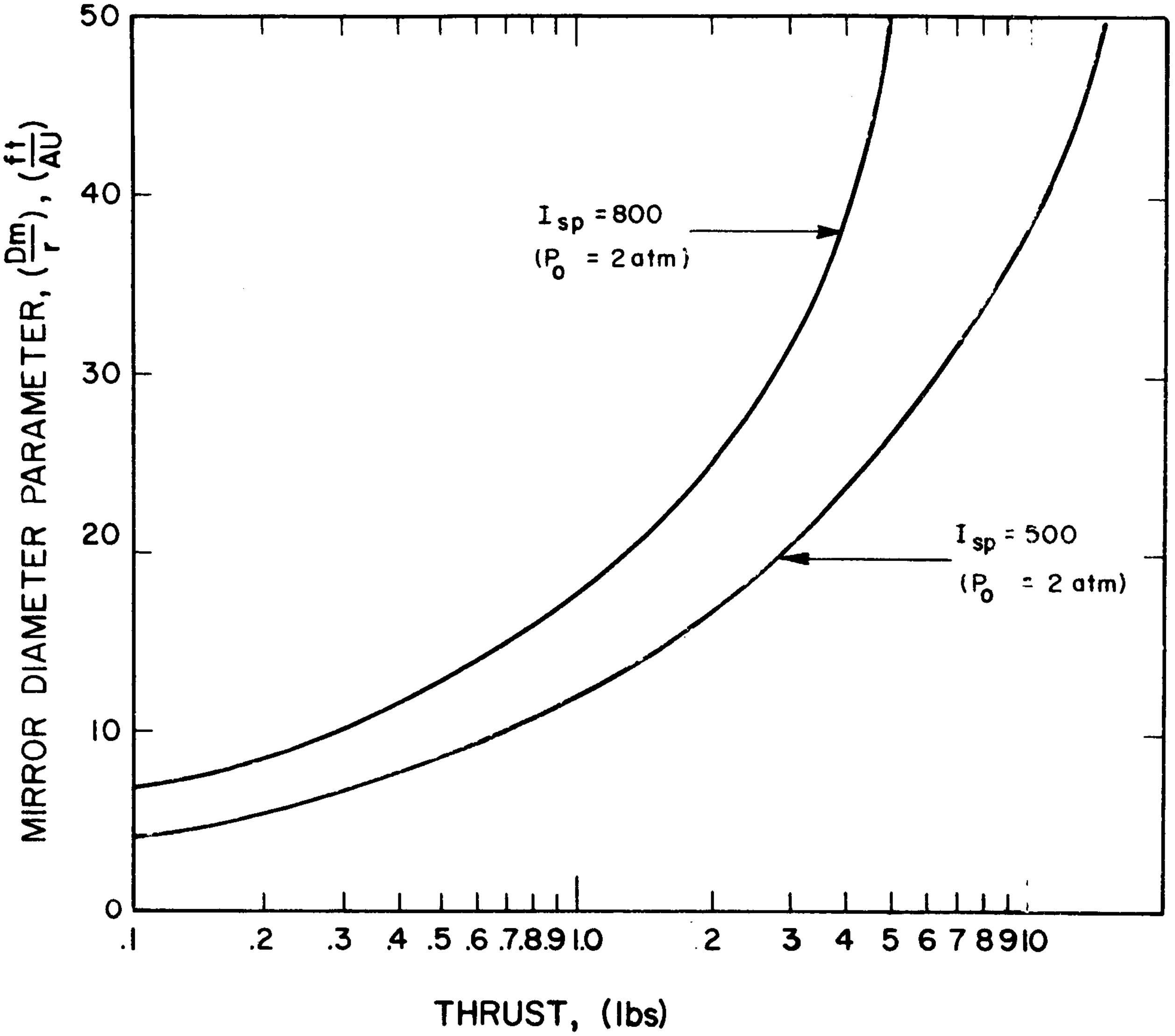

FIG. 3-16 MIRROR DIAMETER PARAMETER VS THRUST

3.3 Nozzle Performance

Definitions:

C_F = thrust coefficient $= \frac{\text{thrust (actual)}}{\text{thrust (ideal)}}$

I_{sp} = Measured specific impulse

$I_{sp,\ id}$ = ideal specific impulse

F = thrust, lbs.

$f_R = R_e/1000(W_h P_o)^{1/2} = \frac{\text{Reynolds No.}}{(\text{KW-Atm.})^{1/2}}$

W_h = Power of hydrogen stream at nozzle entrance, KW.

η_F = Frozen flow efficiency

η_N = Nozzle energy efficiency = C_F^2

Conventional rocket nozzles can be designed to recover a relatively large fraction of the available enthalpy in the hot gas stream. Since the solar rocket propulsion system is inherently a low thrust device, the nozzle size and Reynold's number tends to be considerably smaller than conventional rocket nozzles for many cases. Hence, it can be anticipated that viscous losses during nonisentropic expansion of the heated hydrogen can be higher than normal, thereby reducing the energy efficiency of the system. Some of the work performed at EOS under AF 04(611)-8181 has been used in the following analysis to estimate the losses in performance associated with the very low thrust levels.

Buhler and Moore (Ref. "Performance of Small Hot Gas Expansion Nozzles" EOS RN 13 8-63) examined the frictional and "cosine" losses in small rocket nozzles and derived a first approximation for the thrust coefficient, C_F, as a function of Reynold's number, and of total nozzle power at nozzle entrance (see Fig. 3-17). The authors

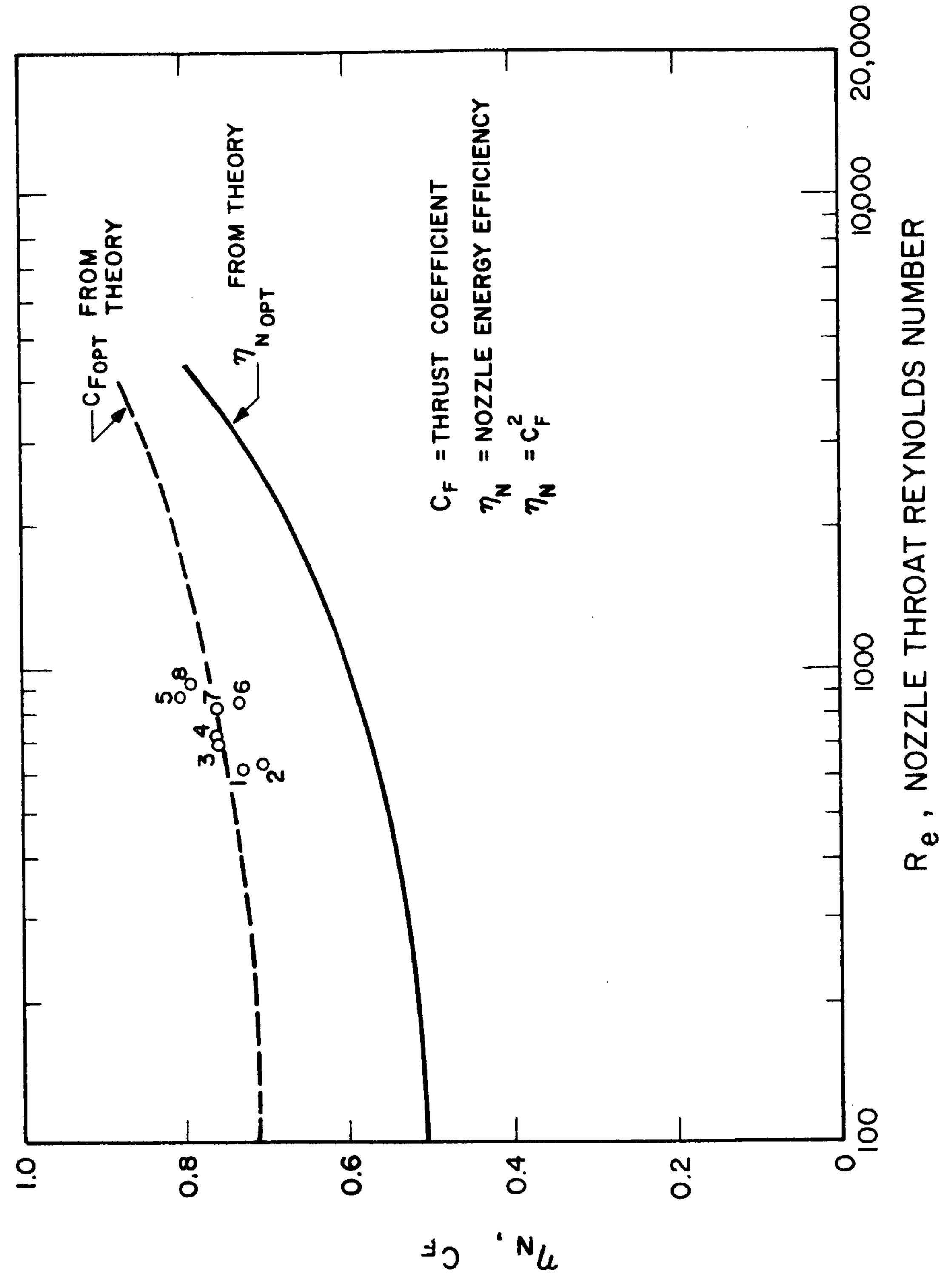

FIG. 3-17 THRUST COEFFICIENT AND ENERGY EFFICIENCY VS REYNOLDS NUMBER

also plot a Reynold's number parameter vs. stagnation temperature, (Fig. 3-18), and Reynold's number parameter vs. frozen flow specific impulse with stagnation pressure as parameter (Fig. 3-19).

On examining both Fig. 3-18 and 3-19, it is apparent that for the temperature range of interest (2000-2500°K) the pressure dependence may be neglected for the curves and retained only in the Reynold's number parameter. To do this we note that for almost any practical system we will be concerned with pressures between 1 and 10 atmospheres, hence the average for these two curves will be a good approximation for the type of systems we are considering.

The energy efficiency will be best if the stagnation pressure is high, but the structural, reliability, and hydrogen diffusion considerations require the lowest possible pressures. For an actual system these questions pose an optimization problem which can, and must be resolved only when more performance data is available. In this analysis curves will be plotted for stagnation pressures of 1 and 2 atmospheres to indicate the variation of η_N with pressure.

With curves and relationships introduced later, it is possible to represent the nozzle energy efficiency as a function of thrust (with specific impulse and pressure as parameters, see Fig. 3-20. The results show that substantial performance gain may be achieved at low thrust if the associated problems at the higher pressures can be tolerated. We can express the thermal power as a function of thrust and specific impulse as follows;

$$W_h = \frac{0.0218\ F\ I_{sp}}{\eta_F\ \eta_N}\text{, Kilowatts} \qquad (3\text{-}26)$$

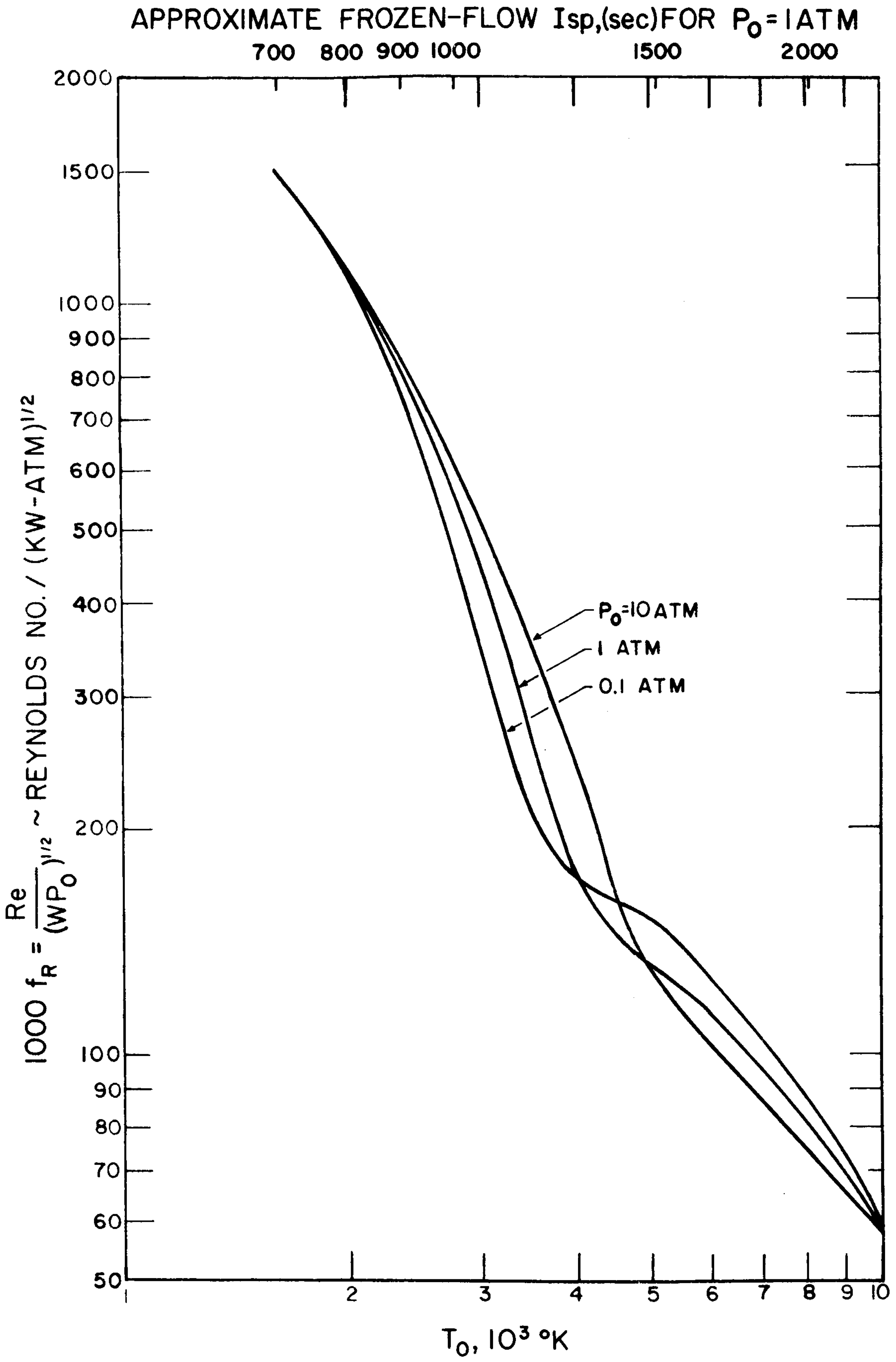

FIG. 3-18 NOZZLE THROAT REYNOLDS NUMBER PARAMETER VS STAGNATION TEMPERATURE FOR HYDROGEN

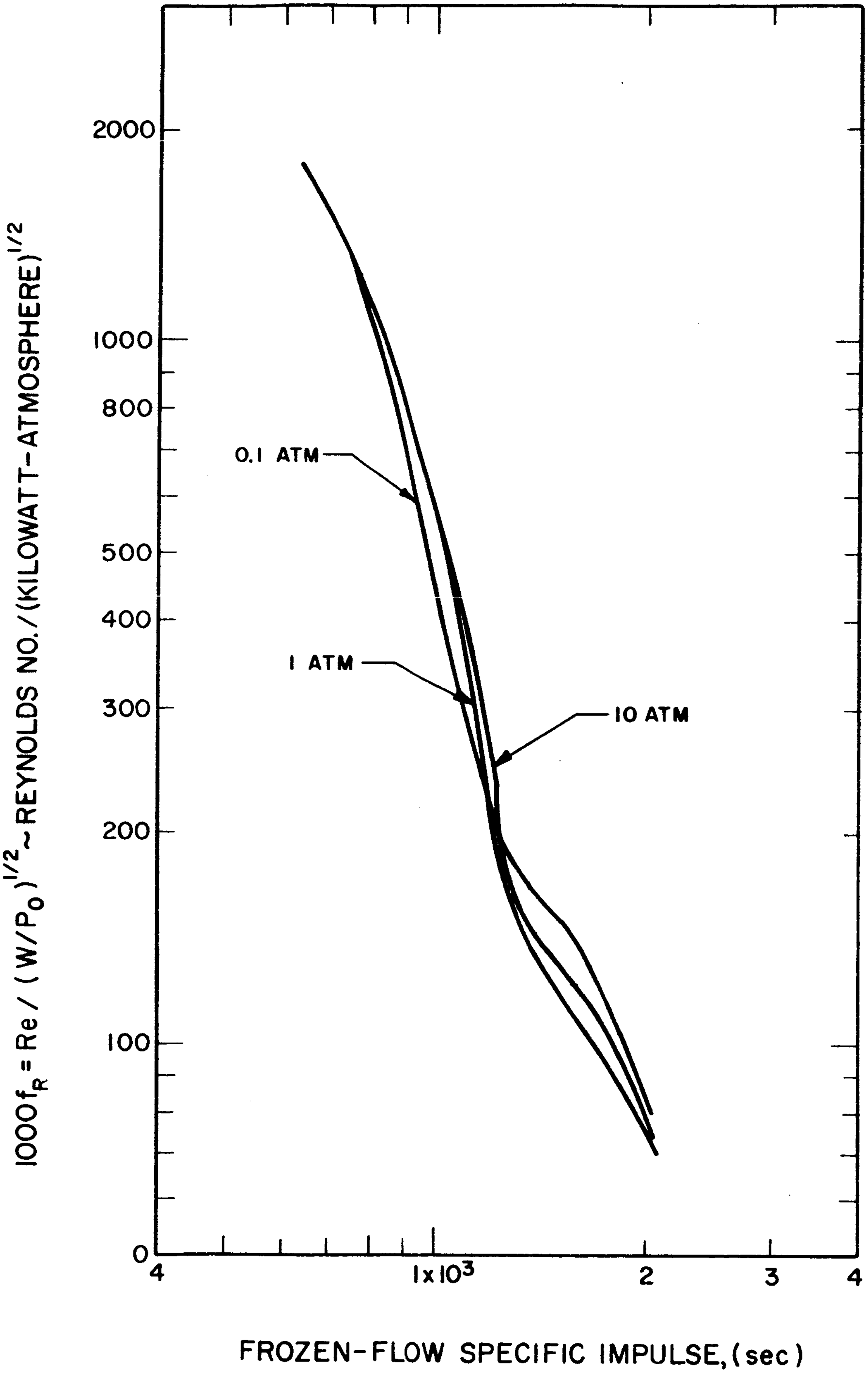

FIG. 3-19 NOZZLE THROAT REYNOLDS NUMBER PARAMETER VS FROZEN FLOW SPECIFIC IMPULSE FOR HYDROGEN

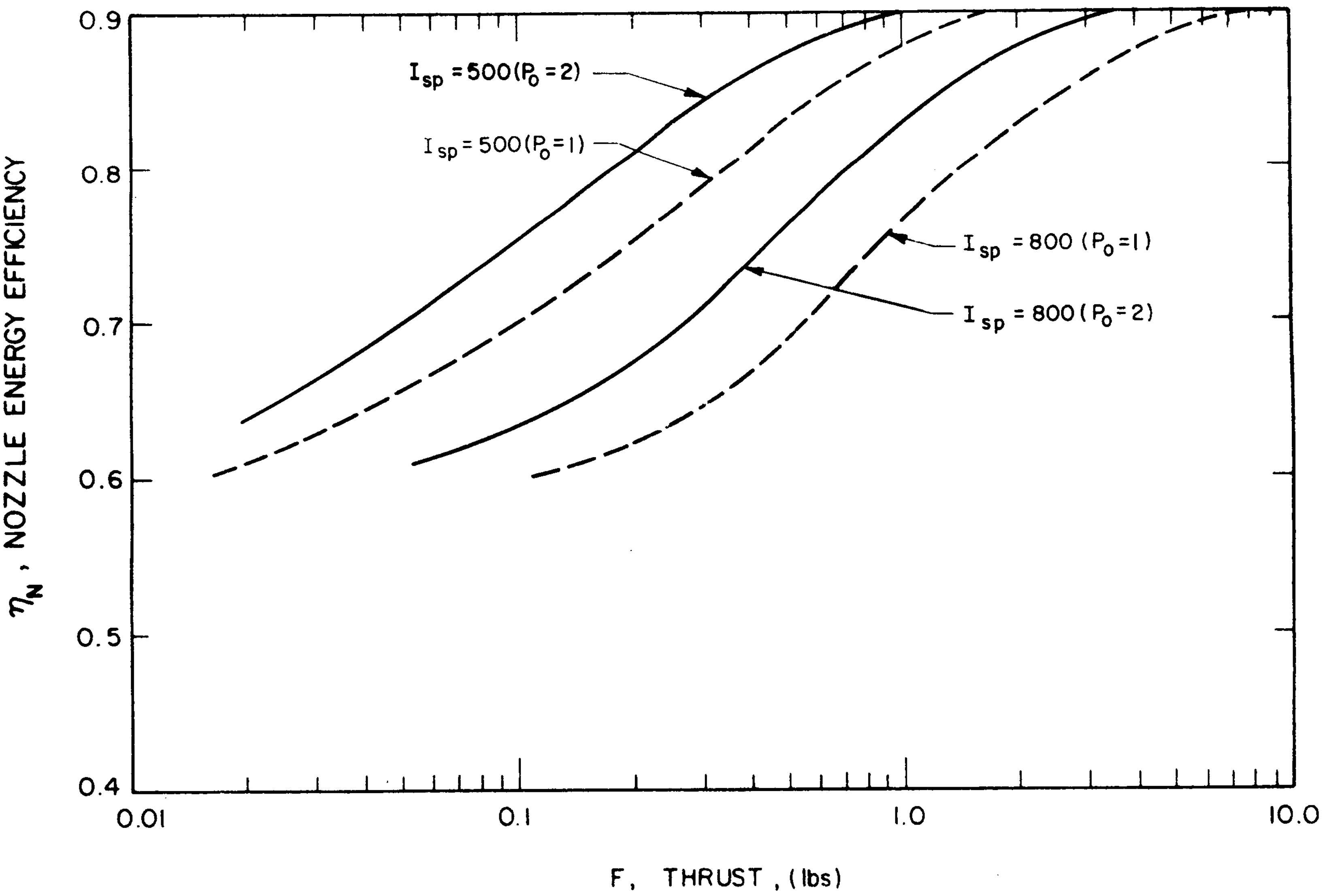

FIG. 3-20 NOZZLE ENERGY EFFICIENCY VS THRUST FOR I_{sp} = 500, 800 SEC.

From Fig. 3-19, we obtain an expression for Reynold's number in terms of power;

$$R_e = 1000\ f_R\ (W_h\ P_o)^{1/2} \qquad (3\text{-}27)$$

Jack ("Theoretical Performance of Propellants Suitable for Electrothermal Jet Engines" John R. Jack, ARS Journal, Dec. 1961.) indicates the frozen flow efficiency for hydrogen $\eta_F = 1$ at $I_{sp} < 900$ sec. and pressures above 1 atm.

Therefore, we obtain the following simplified expression;

$$R_e = 1000\ f_R \left[\frac{.0218\ F\ I_{sp}\ P_o}{\eta_N} \right]^{1/2} \qquad (3\text{-}28)$$

This equation used in conjunction with Fig. 3-17, yields η_N as a function of thrust for assumed values of I_{sp} and P_o. The calculation process is simple; assume a Reynold's number and determine η_N from Fig. 3-17 assume I_{sp} and P_o and determine the parameter 1000 f_R from Fig. 3-19 and finally use the following form of the above equation to calculate thrust;

$$F = \frac{(R_e/1000\ f_R)^2\ \eta_N}{.0218\ I_{sp}\ P_o} \qquad (3\text{-}29)$$

The results are presented in Fig. 3-20 as a function of F for

$I_{sp} = 500$ and 800 sec. and $P_o = 1$ and 2 atm.

Fig. 3-21 is a plot of nozzle energy efficiency vs. mirror size for 500 and 800 sec. specific impulse, and under conditions of full thermal recovery. As is expected, the energy efficiency increases with mirror size (thrust level) and decreases with specific impulse. For a specific impulse of 500 sec., the nozzle energy efficiency is greater than 0.80 for a 7-foot diameter collector. It is evident that high specific impulse systems (800 sec.) are attainable with the large spacecraft (and larger nozzles) only. Thus, for very low thrust level smaller spacecraft (and very small nozzles) the attainable specific impulse will be smaller (~600 sec.) since the upper temperature is fixed by material limitations and the nozzle energy efficiencies will be reduced.

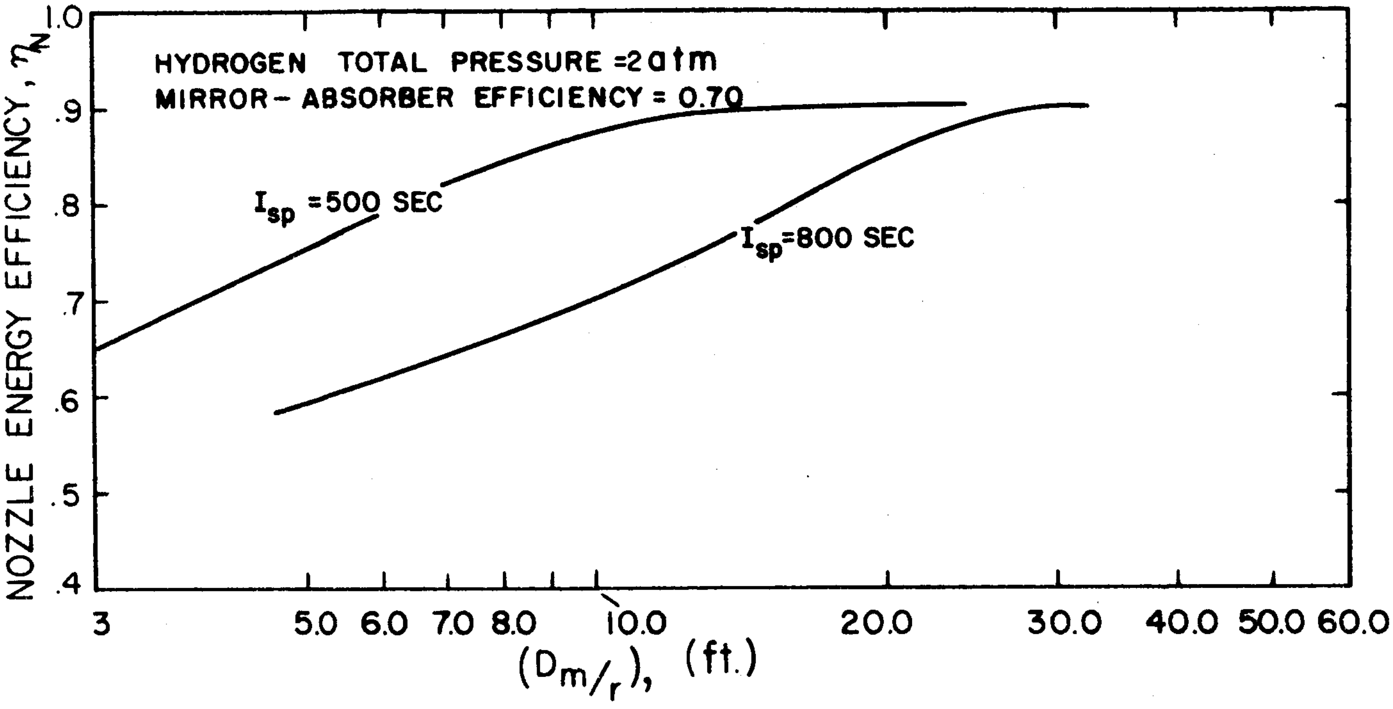

FIG. 3-21 VARIATION OF NOZZLE ENERGY EFFICIENCY WITH MIRROR SIZE

3.4 Diode Characteristics

Thermionic diodes operate on the principle wherein hot surfaces emit electrons according to Richardson's equation. When surfaces at different temperatures, and emitting electrons at different rates are connected through an external circuit, then an electric current will flow. The first step towards getting useful amounts of electric power out of such a device is to try to eliminate the space charge which tends to develop between an anode and a cathode of such a device. The most accepted method used at the present time is a source of positive ions (cesium) introduced in the interelectrode gap and used to neutralize the excess electrons forming the space charge. Under conditions where the space charge is assumed to be negligible, the diode efficiency is given by

$$\eta_D = \frac{(\phi_C - \phi_A)\, J_{ext}}{J_{ext}\, (\phi_C + 2\, k\, T_C) + Q_{str} + Q_r + Q_{cesium}} \qquad (3\text{-}30)$$

J_C, J_A = cathode and anode current respectively as given by Richardson's equation .

J_{ext} = external current .

ϕ_C, ϕ_A = cathode and anode work functions respectively.

k = Boltzman constant .

Q_{cesium} = heat conducted away from cathode to anode by cesium vapor.

Q_r = heat lost by radiation from cathode to anode.

Q_{str} = heat conducted away from cathode by support structures.

T_C = absolute temperature of cathode face.

The output voltage is proportional to $(\phi_C - \phi_A)$. To achieve a highly efficient thermionic diode, $(\phi_C - \phi_A)$ should be made as large as possible, J_A should be a small fraction of J_C, Q_{cesium} and Q_r should all be made as small as possible. In the design of a diode care has to be taken to exclude any foreign gases that may tend to upset the neutralizing effect of the cesium ions. The design must also be such that the proper spacing results at the operating temperature. The cathode and anode materials must also be such that they have low vapor pressures and so prevent a build up of one on the other. During operation the electrodes must not undergo changes in crystal orientation or growth that may adversely effect the diode performance.

Figure 3-22 is a plot of thermionic diode performance vs emitter temperature. Although a diode efficiency of 20 percent is indicated at 3400°F, such a system cannot presently be built to operate over any prolonged period of time due to materials limitations, and systems for missions contemplated in this report are expected to have an efficiency of approximately 10-15 percent at emitter temperatures of about 3100°F.

Figure 3-23 is a recent photo of a solar energy thermionic generator system built by EOS for the Jet Propulsion Laboratory (JPL PO 950349). When tested with a tungsten electron bombardment source, this system delivered almost 60 watts. With a solar energy source at 1.0 AU in space, the overall performance of a similar unit employing additional diodes should result in an output of about 150 watts with a five (5) foot diameter collector.

3.5 Energy Storage

Due to the high operating temperature of the SOHR-SET system, it would be desirable to eliminate thermal cycling in order to prevent the reduced operational life which is a consequence of such cycling. If there is no energy storage mechanism thermal cycling will occur if the space craft passes through the shadow of the earth or other

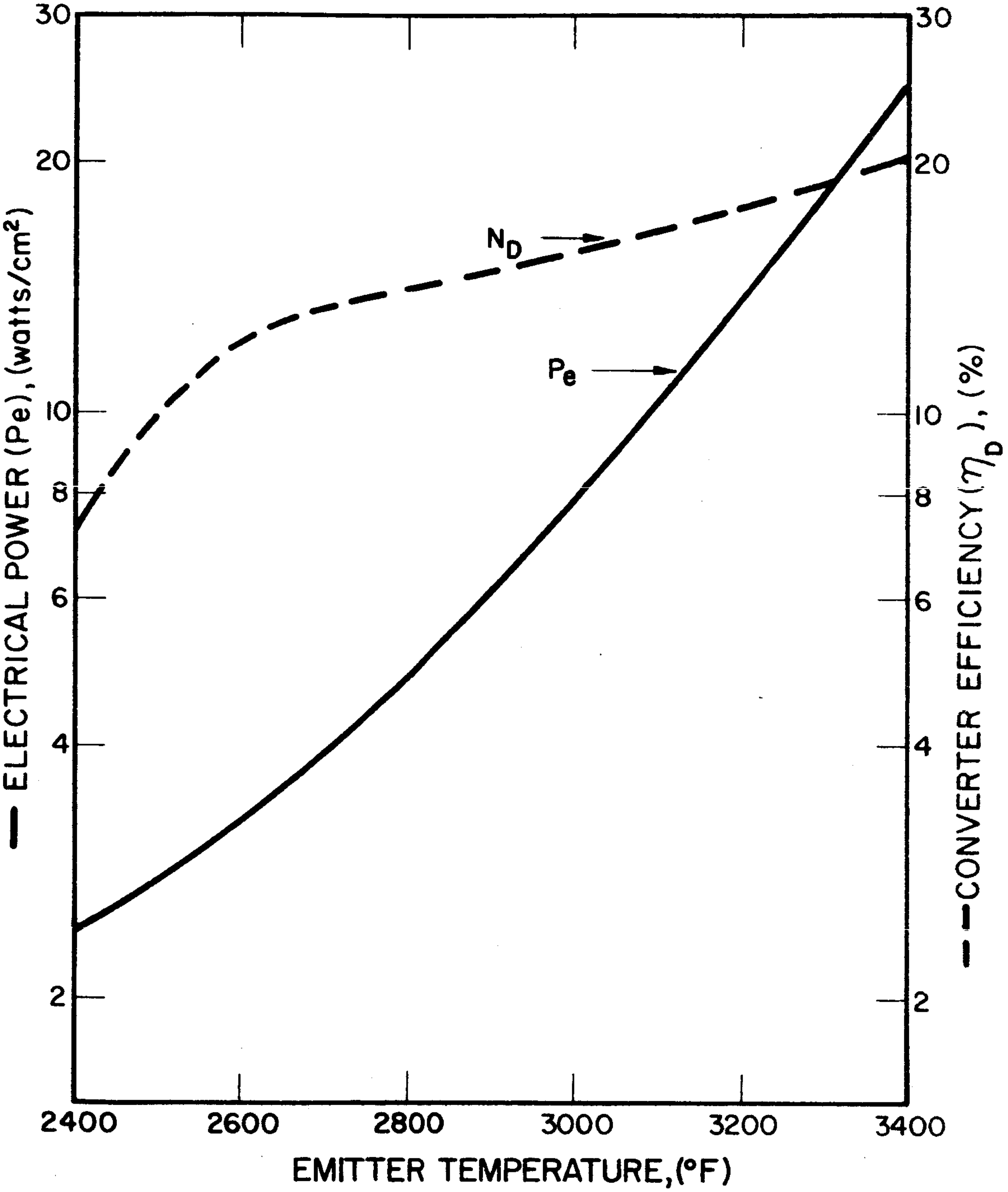

FIG. 3-22 THERMIONIC DIODE PERFORMANCE VS EMITTER TEMPERATURE

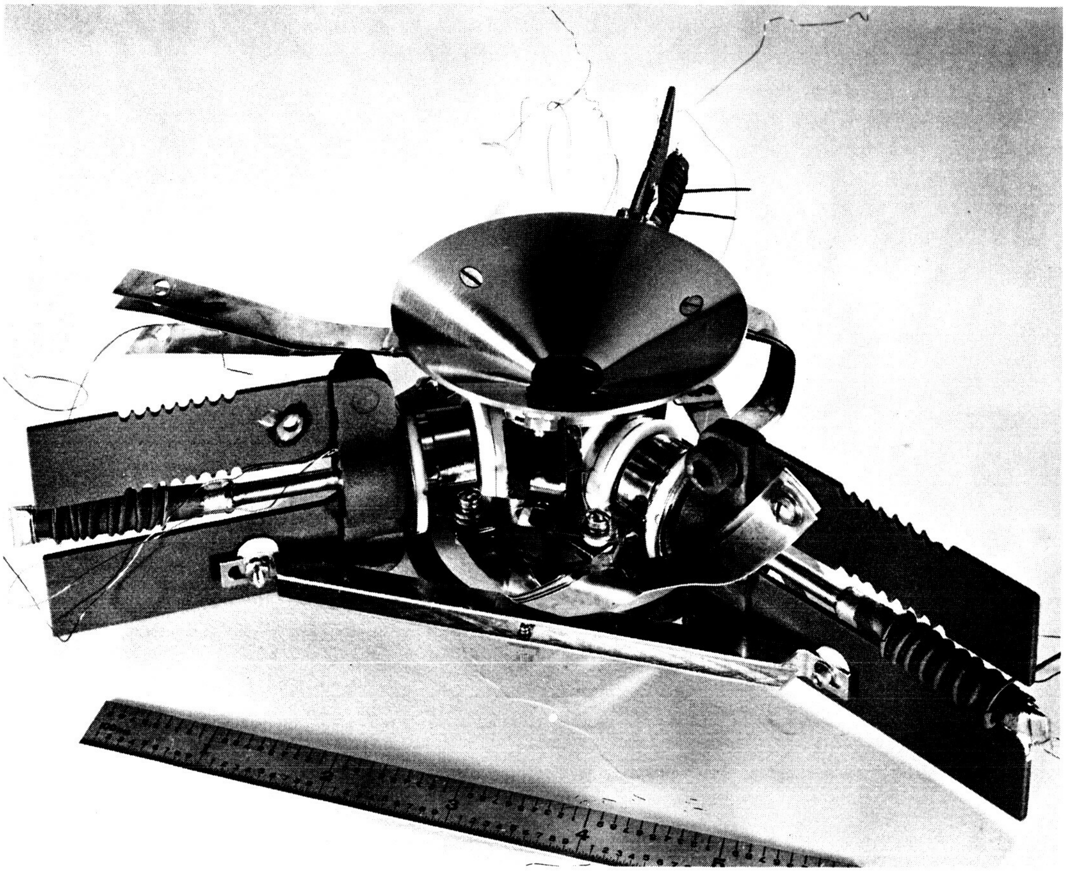

FIG. 3-23 SOLAR ENERGY THERMIONIC GENERATOR (Built by EOS for Jet Propulsion Laboratory)

planet, or if there is a momentary misorientation of the solar collector. If energy is stored in the cavity, then cycling can be damped out by the heat reservoir.

There are three basic requirements for energy storage devices.

1. High capacity in terms of energy stored per unit weight and volume.
2. The capability of many charge and discharge cycles without degradation.
3. Discharge characteristics may vary only slightly with temperature and load.

Among the possible methods of energy storage are heat storage by thermal capacity, order-disorder transitions, heat of fusion, heat of vaporization, thermochemical reaction, heat of sublimation, capacitors, batteries, regenerative fuel cells. Of these, heat of fusion devices, batteries, and fuel cells appear to be the most promising systems. When one considers that with cyclic operation, available batteries have an energy storage capacity of only 5-10 watts-hrs/lb, and the regenerative fuel cell capacity is projected at approximately 20-30 watt-hrs/lb., then these two storage systems would compete with thermal energy storage by heat of fusion (TES), under certain special conditions only (on a weight basis). The following simplified analysis will indicate the crossover point for comparative weights between the electrochemical storage versus the thermal storage for a complete system. The system weight can be described by the following expression:

$$W_{sys} = \frac{P}{\alpha}\left[1 + \frac{1}{\eta}\left(\frac{t_D}{t_C}\right)\right] + \frac{P t_D}{\beta} \qquad (3\text{-}31)$$

where:

P = Power, watts

α = Energy converter specific power, watts/lb.

t_D = Discharge duration, hours

t_C = Charge duration, hours

η = Efficiency, $\frac{\text{output}}{\text{input}}$ of storage system

β = Storage system capacity, watt-hrs./lb

The crossover point for electrochemical versus thermal storage can be established from the following relationship:

$$\epsilon\beta_{\text{thermal}} = \frac{1}{\frac{1}{\alpha\eta_B t_C} - \frac{1}{\alpha\eta_T t_C} + \frac{1}{\beta_{\text{Battery}}}} \tag{3-32}$$

where

ϵ = Energy Converter Efficiency, $\frac{\text{Electrical Output}}{\text{Thermal Input}}$

In most cases this expression can be approximated by:

$$\beta_{\text{Thermal}} = \frac{\beta_{\text{Battery}}}{\epsilon} \tag{3-33}$$

Therefore, the thermal storage will be superior to the electrochemical on a weight basis for almost all cases where the heat of fusion is at least ten times ($\epsilon = 10\%$) the energy to weight ratio of the battery. This appears to be the case for available or anticipated secondary batteries, and almost all heat of fusion materials currently under evaluation. Of course, the thermal storage enjoys the additional advantage of minimizing thermal cycling problems. A further reason for choosing TES is that it is potentially a simpler and inherently more reliable device once the materials compatibility problem is solved. Consider a system utilizing TES. Then,

$$\frac{E_s}{Q} = 1/[1 + t_D/(t_C\eta)] \equiv f_T \tag{3-34}$$

$$E_T = (E_s\ t_D)/(\eta\ t_C)$$

$$W_T = (E_T tc/\eta H_T/f_s) = E_s t_d/(\eta H_T/f_s)$$

E_S = rate at which energy is used by SOHR-SET
E_T = rate at which energy is withdrawn by TES
Q = rate at which energy is absorbed in cavity
f_T = energy storage factor

W_T = Weight of TES material

H_T = Energy storage capacity of TES material

f_s = Structural factor for TES system

For a 300 nm circular orbit;

t_D = .59 hr.

t_C = 1.59 hrs.

and for the 24 hr. synchronous orbit;

t_D = 1.16 hrs.

t_C = 22.84 hrs.

hence

f_T = 0.629, 300 nm orbit
= 0.948, synchronous orbit

Purdy has shown (Batutis and Purdy "Thermal Energy Storage For Thermionic Conversion") that at least for one TES system design concept, the optimum oxide content for ceramic oxide-molybdenum combinations is approximately 0.90. Though this design is by no means the ultimate, it nevertheless indicates a value for design purposes. To be conservative, this analysis will be based on a 85% oxide content. An oxide with a heat of fusion of 200 watt hrs/lb yields an oxide-molybdenum matrix with the capability of 135 watt-hrs/lb (these aspects are discussed in greater detail later on in this section) If the structural factor is 1.10, then one may charge to TES a H_T/f_s of 110 watt hrs/lb.

For an orbit raising mission, the power reduction due to TES is greatest at the parking orbit level (t_D/t_C greatest there), but the energy stored is least there (t_C is smallest there). For a 300 n.mi. parking, the amount of power withdrawn for storage is ~ 7 times greater than that withdrawn for a spacecraft in a 24 hr synchronous orbit, whereas the TES System weight required increases by a factor of three. An important implication of these results is, that in order to fully utilize all the energy absorbed by the system, the ideal thrust for orbit lifting with TES, is not a constant thrust, but an ever increasing thrust, which is a function of the spacecraft altitude from earth. There are, of course, system considerations such as added complexity which may rule out the variable thrust approach. One of the desirable aspects of a SOHR-SET system is its simplicity, and this must never be compromised.

Utilizing the formulae developed earlier we find that,

$$W_T = E_s\, t_D/(\eta H_T/f_s) = 0.0105\, E_s$$

for 24 hr orbit and $\eta = 1$

Hence, for a 24 hr orbit

(weight TES system, lbs)/watts absorbed by cavity =

$$W_T/(E_s/f_T) = 0.00661 \qquad (3\text{-}35)$$

and for $\eta_{m-a} = 0.70$

(weight TES System, lbs)/watts falling on system =

$0.00661\eta_{m-a} = 0.00462$

In the design of TES systems, some general problem areas are evident. These are;

1. Diffusion to or from the TES material.
2. Reactivity of the TES material.
3. Specific energy storage capacity.
4. Thermal conductivity of TES material.
5. Containment material vapor pressure and grain growth.

It is objectionable to have diffusion to or from the TES material if it adversely affects the functioning of the system. Diffusion could conceivably alter the stability of the ceramic oxide, or affect the functioning of the thermionic diodes.

The reactivity of the TES-containment vessel system must definitely not be appreciable over the projected life time of the system. Unfortunately, there is no method available for predicting compatibility, the best that may be done is to predict incompatibility based on free energy data, and then screen successful candidate TES systems by testing.

The energy stored per unit TES system weight depends on the energy storage capacity of the TES material,and to a certain extent in the design concept used. TES materials should be pure compounds, eutectics, or at least have "essentially congruent" melting points. These materials will most likely be mixtures of certain light metal compounds (the stable oxides, MgO, BeO, CaO, Al_2O_3) or the stable light-metal compounds themselves. The need for stable compounds is evident, and the light-metal requirement is a consequence that these metals or their compounds give high heats of fusion per unit weight. Tables 3-1 and 3-2 list some physical properties of ceramic oxides of interest to TES system design. These oxides have low vapor pressure, and at least one, 3 BeO-2MgO is being developed as a TES material. Note that quite a bit of work remains to be done on quaternary systems. It is possible that promising eutectics may be found among them.

Tungsten-Rhenium alloys are currently being developed for use with the above ceramic-oxide materials, and this area of investigation shows great promise (this matter will be discussed later). It should be noted that such factors as impurities, grain growth, and vapor pressure are very important considerations for TES container materials. It is desirable that the vapor pressure be less than 10^{-6} mm Hg, and these vapors should definitely not have an adverse effect on the structural integrity of any of the cavity or diode elements which it may contact. As a possible means of containing the TES material, it is proposed that the material be used in an encapsulated state. A technique for achieving this

TABLE 3-1 PROPERTIES OF SELECT MIXTURES OF THE STABLE CERAMIC OXIDES*

Oxide Mixture	M.P., °K	Density		Heat of Fusion	
		g/cc	lb/in^3	cal/g	watt-hrs/lb.
$3BeO-2CaO$ (compound)	1630	3.00	0.11	180	95
$5CaO-3Al_2O_3$ (compound)	1730	3.66	0.13	70	37
$CaO-Al_2O_3$ (eutectic)	1870	2.73	0.10	115	61
$4MgO-4BeO-Al_2O_3$ (eutectic)	1910	3.56	0.13	340	179
$MgO-4BeO-Al_2O_3$ (compound)	2020	3.57	0.13	360	190
$3BeO-2MgO$ (eutectic)	2120	3.20	0.12	500	264

*Ref. E. F. Batutis and D.L. Purdy, "Thermal Energy Storage for Thermionic Conversion" Paper No. 2505-62, ARS Space Power Systems Conference, Santa Monica, California.

TABLE 3-2 PHYSICAL PROPERTIES OF THE STABLE CERAMIC OXIDES*

Oxide	Molecular Weight	M.P. °K	Density g/cc	Heat of Fusion (cal/g)	cal/cc	Entropy Cal/°K mol	Cal/°K·g	Thermal Conductivity at 1670°K Cal. Sec.$^{-1}$cm^{-2} cm° C-1
Al_2O_3	101.96	2303	3.97	255.0	1012	11.3	0.11	0.0131
BeO	25.01	2803	3.01	679.7	2077	6.1	0.24	0.362
CaO	56.08	2873	3.32	338.8	1125	6.6	0.12	0.0174
MgO	40.32	3073	3.63	458.8	1675	6.0	0.15	0.0144

*Ref. E. F. Batutis and D.L. Purdy, "Thermal Energy Storage for Thermionic Conversion" Paper No. 2505-62, ARS Space Power Systems Conference, Santa Monica, California would be to coat small low density particles of the material with a high melting point material such as molybdenum, then fill the storage container with the material and compress under high pressure to a dense state. The need for this type of TES became apparent after reading the G.E. Analysis (Batutis and Purdy) even though it was not suggested by the authors in the analysis. The initial low density requirement is necessary so that when compressed, the particles will deform and pack densely this ensuring intimate contact between metal coatings. Under these circumstances, the design must be such that during fabrication, the volume available to TES material is the maximum value that the TES material will achieve in use. If this be the case, then volume change during cycling will no longer be of major concern.

Fig. 3-24 shows the improvement in gross thermal conductivity that may be achieved in such a scheme. Note that even though the storage capacity decreases with oxide content in the range of oxide content of interest, say 0.5-0.9, the thermal conductivity increases at a much faster rate than the rate of decrease of energy storage capacity. It is expected that such systems will yield more than 100 watt-hrs/lb in the fabricated state. This seems reasonable when one considers that the TES material per se can be expected to yield storage capacities in the 180 to 260 watt-hrs/lb range.

One of the most promising candidates for TES application, 3 BeO-2MgO has so far withstood 1196 hrs at temperature (MP = 2120°K, 264 watt hrs/lb) without evidence of the tungsten-rhenium container being chemically attacked (E.F. Batutis, "Storing Thermal Energy", Astronautics and Aerospace Engineering, May, 1963). Tests at and exceeding the 5000 hr. level are planned.

To recover the energy from the stored state, both conduction and radiation paths must be considered. It is conceivable that the coils may be brought in contact with the material to facilitate heat transfer during earth-shadow operation, or this may be undesirable due to the effects of diffused hydrogen on the TES system.

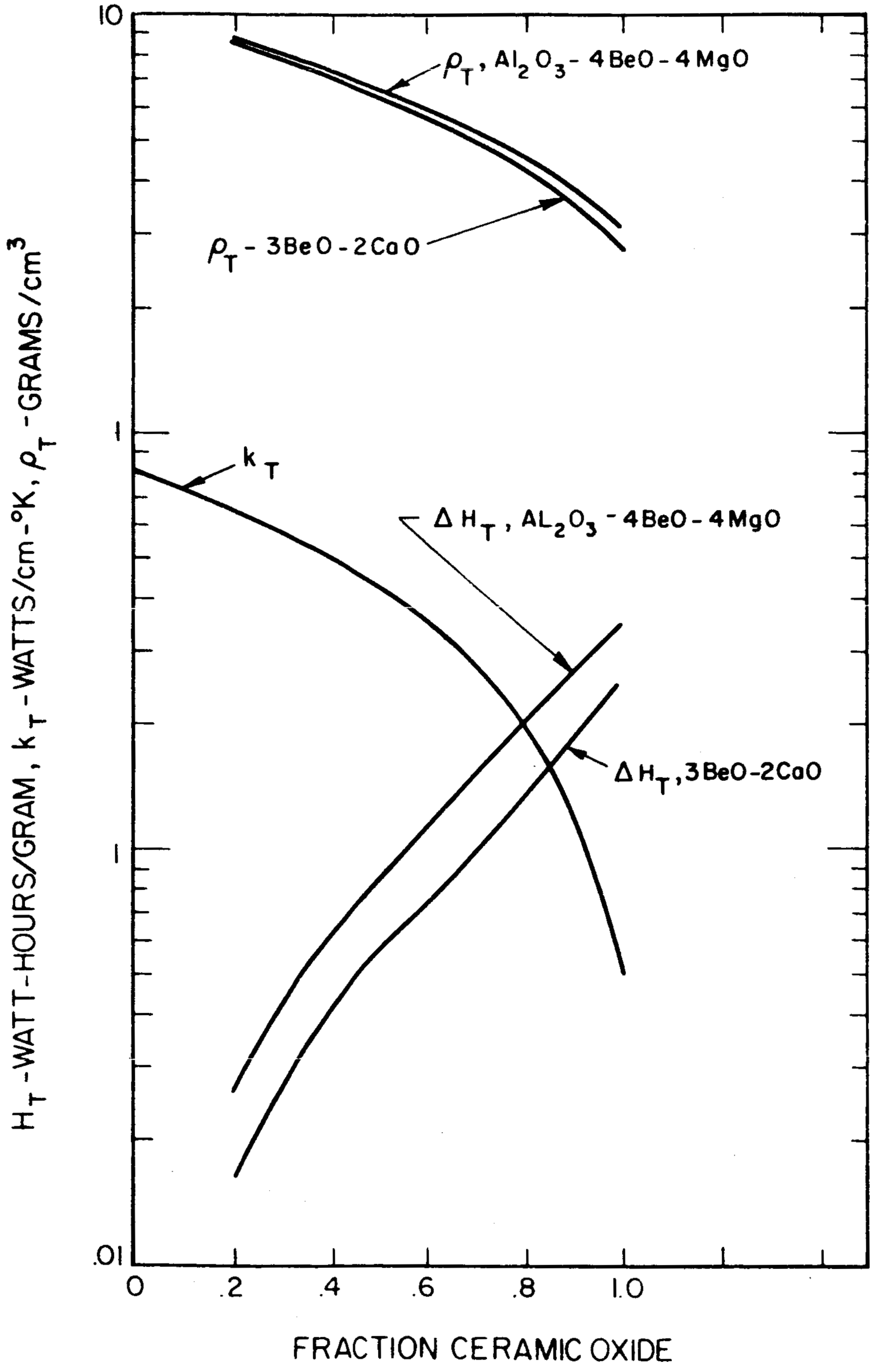

FIG. 3-24 THERMAL CONDUCTIVITY, DENSITY, AND HEAT OF FUSION OF MIXTURES OF MOLYBDENUM AND CERAMIC OXIDES

4. DESIGN STUDY OF COMBINED CAVITY ABSORBER

4.1 Introduction

There are four important subsystems in the design of a combined cavity absorber.

1. The cavity entrance flux control and aperture plate.
2. The thermal regeneration system.
3. The diodes.
4. The thermal energy storage system.

4.2 Cavity Entrance, Flux Control, and Top Plate Considerations

The cavity entrance can be designed as a flat plate absorber so that any stray incoming radiation can be utilized as a pre-heat system for the gas entering the cavity. It is an alternative to the conical flux trap concept.

With regards to flux control, it appears that a rather versatile flux flap is required. If the spacecraft distance from the sun is constantly changing, then the flux flaps must be capable of adjusting the cavity aperture diameter or the effective cavity diameter accordingly, since both the sun's image diameter and the solar radiation intensity are functions of distance from the sun. During the period of time when the SOHR-SET is receiving its energy from its heat reservoir, the ideal condition is to have the cavity opening closed. Hence, not only should the system be capable of modulating solar influx to the cavity, but it should also be capable of literally closing off the cavity entrance during dark time to conserve the thermal energy stored. Figure 4-1 indicates the manner in which the cavity opening must be adjusted for operation in space at different solar distances. Note, that for constant energy withdrawal from the cavity, the aperture adjustment

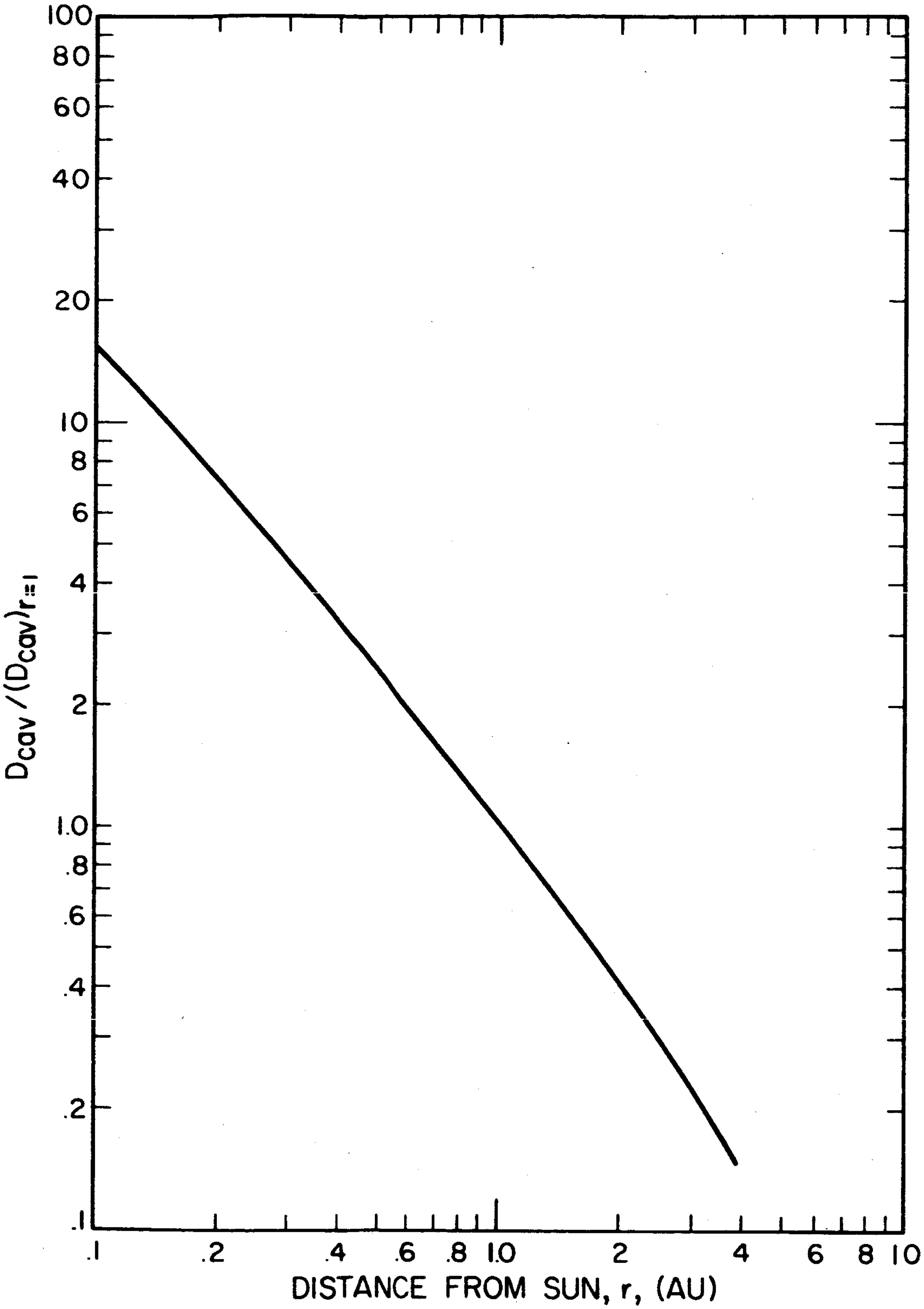

FIG. 4-1 CHANGE IN CAVITY OPENING VS DISTANCE FROM SUN (T_{cav} = 4500°R, Maximum Energy Withdrawn at Optimum Mirror Absorber Efficiency)

control may be achieved by blocking off incident flux or defocusing the cavity, but that control could also be achieved by opening up the cavity entrance. For most applications, blocking of incident flux or defocusing the cavity, appear to be among the more practical means of achieving flux control. For a mission to 0.3 AU the optimum aperture diameter increases by a factor of 4.5 for the optimum constant efficiency case, where as for a mission to 2 AU the optimum cavity entrance diameter is now reduced to approximately 0.4 the initial value.

It is conceivable to design a flap by having the cavity temperature operate a vernier-like positioning mechanism, and by having the presence or absence of stray flux on the top plate operate a normally closed device. Current design practice is to make the cavity entrance diameter approximately 1 percent of the collector diameter, when operating at 1.0 AU.

4.3 Design Considerations for the Hydrogen Heat Transfer Coils

In the cavity, the hydrogen is heated by passing it through tungsten, molybdenum, rhenium, or rhenium alloy coils which are heated by the reradiation in the cavity, and by the direct impingement of the incoming solar radiation. The coils must be arranged in the cavity in such a fashion that the hottest point occurs at the point of exit of the gas stream. In order to do this, the coil geometry becomes very important since this determines the local intensity of the incident solar radiation. The incident solar radiation for a heating coil arrangement as shown in Fig. 4-2 is:

$$Q_s = \frac{4f^2 H \eta_m}{R_o^2} \frac{\sin^3 (\alpha + \theta)}{\cos^2 \alpha (1 + \cos \theta)^2} \qquad (4\text{-}1)$$

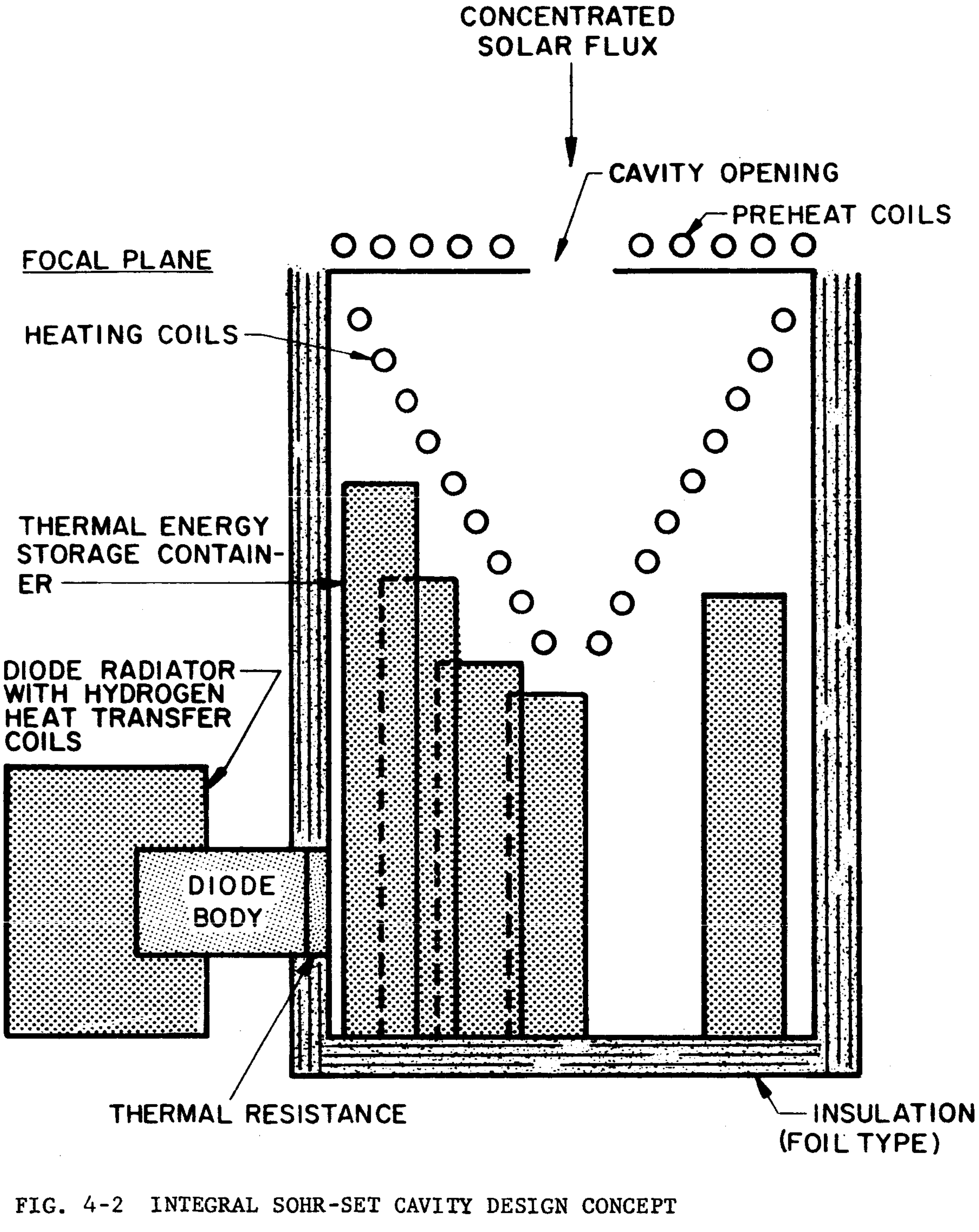
CONCENTRATED SOLAR FLUX
CAVITY OPENING
PREHEAT COILS
FOCAL PLANE
HEATING COILS
THERMAL ENERGY STORAGE CONTAINER
DIODE RADIATOR WITH HYDROGEN HEAT TRANSFER COILS
DIODE BODY
THERMAL RESISTANCE
INSULATION (FOIL TYPE)

FIG. 4-2 INTEGRAL SOHR-SET CAVITY DESIGN CONCEPT

where

Q_s = incident solar radiation per unit area

f = focal length of collector

R_o = length of radius vector from focal point to point under consideration

α = half angle of conical surface on which coils lie ($\alpha = 0$ for cylindrical cavity)

θ = angle between cavity axis and line from focal point to point under consideration

The value of α is usually chosen as 30 degrees to minimize the coil length, the maximum flux on a 30 degree coil is given by

$$Q_{s_{max_{30}}} = \frac{0.445\ 4f^2 H\eta_m}{R_o^2} \qquad (4\text{-}2)$$

For a coil design utilized as per Fig. 4-2 , the intensity of the incident solar radiation decreases as the distance from the focal plane increases. From a heat balance about the element of the exit section of the heating coil receiving the most intense solar radiation, it can be shown that

$$Q_H \approx \alpha_s\ Q_s \approx h\ (T_{we} - T_b) \qquad (4\text{-}3)$$

where

Q_H = energy transferred to hydrogen

α_s = absorptivity at solar wavelengths

h = heat transfer coefficient

T_{we} = wall temperature at exit

T_b = hydrogen bulk temperature at outlet, $4000^{\circ}R$

If we assume:

$$T_{we} - T_b = 400^{\circ}R \qquad (4\text{-}4)$$

$$Q_{s_{max}} \approx \frac{400}{\alpha_s} h$$

For laminar flow (and this is usually the case), the heat transfer coefficient is approximately,

$$h = \left(\frac{k_H}{d_t}\right)\left[5.14 - (0.78)\ (T_{we}/T_{be})\right] \tag{4-5}$$

where

d_t = tube internal diameter

k_H = thermal conductivity of hydrogen at 4000°R
$\approx$ .58

hence maximum allowable value of Q_s is

$$Q_{s_{max}} = \left(\frac{400\ k_H}{\alpha_s\ d_t}\right)\left[5.14 - (0.78)\ (T_{we}/T_{be})\right] \tag{4-6}$$

where $Q_{s_{max}}$ is given by equation 4-2.

If these relationships are used, the general cavity-heat exchanger configuration can be estimated for safe ΔT across the heat transfer boundary. Within limits, this represents a relatively simple technique for estimating size and geometry to protect against "hot spots" and subsequent burnout. In practice, this more conservative cavity design might be refined to reduce the outside surface area, thereby decreasing thermal losses and improving overall efficiency.

4.4 Integration of the Thermionic Diodes

Two major considerations dictate the manner by which the thermionic diode is incorporated in a combined cavity absorber. One consideration is the fact that the thermionic diode emitter face operates at a temperature which may be as much as 1,000°R less than the optimum for the SOHR aspect of the design; hence, some method must be found to deliver heat to the emitter face of the thermionic diode at a lower temperature. The second consideration is coupled with the first and is the requirement that the temperature on the emitter face must be uniform. These considerations rule against placing the diodes in the forward part of the cavity;* here the direct solar radiation is most intense and the variation steepest. The diodes should be placed in the rear of the cavity preferably in the shadow of the coils and the thermal energy storage containers (Fig 4-2).

To transfer the heat to the emitter face at a temperature difference as high as 1,000°R, several general approaches have been considered. Two of these approaches are shown in Fig. 4-3. These approaches can be used in conjunction with the conventional type diode configuration in which both the emitter and the collector are of plane geometry. The heat transfer is accomplished by conduction or combination of conduction and radiation.

An alternate approach is to use the heat exchanger as a "radiating wall" to transfer energy to a series of cylindrical diodes which comprise the outer wall of the cavity.

---

*It is possible to choose the geometry of the heat conduction path so that the temperature on the emitter face is uniform even though the temperature variation might be severe on the cavity side.

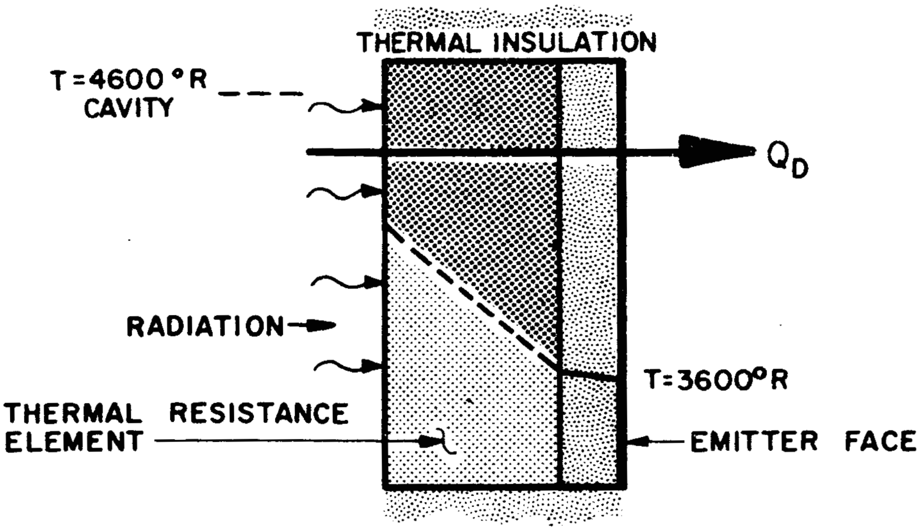
THERMAL INSULATION
T=4600°R
CAVITY
Q_D
RADIATION
T=3600°R
THERMAL RESISTANCE ELEMENT
EMITTER FACE

(A) TEMPERATURE RESISTANCE ELEMENT

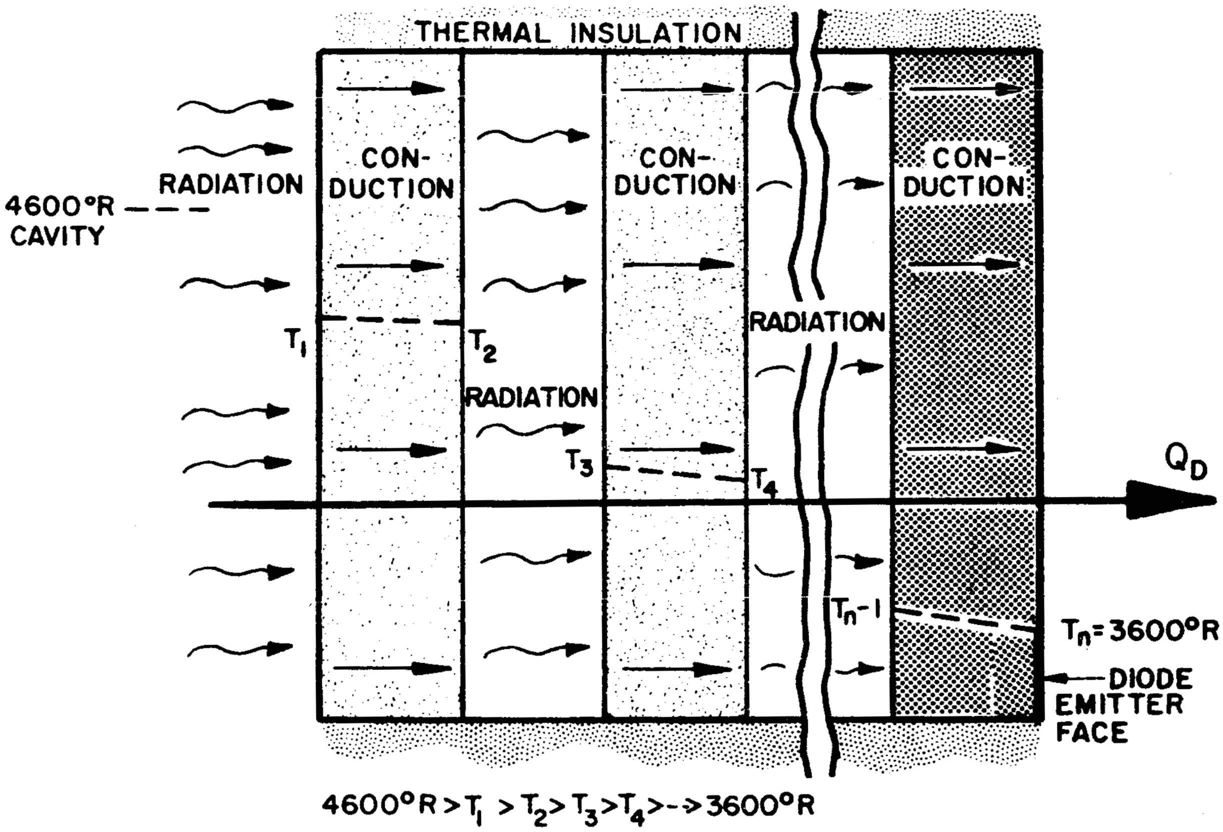
THERMAL INSULATION
RADIATION
4600°R
CAVITY
CONDUCTION
CONDUCTION
CONDUCTION
RADIATION
RADIATION
T_1
T_2
T_3
T_4
T_n-1
Q_D
T_n=3600°R
DIODE EMITTER FACE
$4600°R > T_1 > T_2 > T_3 > T_4 > - - > 3600°R$

(B) TEMPERATURE REDUCTION BY RADIATION AND RESISTANCE ELEMENTS IN SERIES

FIG. 4-3 MODES OF HEAT TRANSFER FROM CAVITY TO DIODE EMITTER

In Fig. 4-3a, the heat is first transferred by radiation from the cavity to the surface of the thermal resistance element, then conducted with the required temperature drop to the diode emitter element. The required emitter drop across the resistance element may be large or small depending upon the fraction of the temperature drop which occurs as a consequence of the radiative heat transfer to the surface of the thermal resistance element. The temperature drop due to radiative heat transfer will be large if the emissivity of the thermal resistance element is small, and small if the converse is the case. If the emissivity of the thermal resistance element is as large as 0.9, then substantially all of the temperature drop may occur across the thermal resistance. Whereas, if the emissivity is small, say 0.3, then substantially all the temperature may occur as a consequence of radiation from the cavity to the surface of the resistance element. The derivation of the equations from which these conclusions were drawn are shown below. From a heat balance about the wall face of the resistance element

$$T_w = \left(T_c^4 - \frac{Q_D - \alpha_s Q_s}{\sigma \epsilon} \right)^{1/4} \tag{4-7}$$

T_w = absolute wall temperature of thermal resistance element

T_c = absolute cavity temperature

T_e = absolute temperature of emitter face

Q_D = diode heat flux

Q_s = incident solar radiation

α_s = absorbtivity at solar wavelengths

σ = Stefan-Boltzmann constant

ϵ = emissivity of wall of thermal resistance element for

$$Q_s = 0$$

$$T_w = \left(T_c^4 - \frac{Q_D}{\sigma\epsilon}\right)^{1/4} \tag{4-8}$$

now

$$Q_D = \frac{\Delta T}{x} \; \frac{1}{\left(\frac{1}{k}\right)_{\text{resistance element}} + \left(\frac{1}{k}\right)_{\text{emitter}}} \tag{4-9}$$

$$= \frac{k_m}{x} \Delta T$$

where

k_m = thermal conductivity (equivalent)

ΔT = temperature drop

x = length of heat transfer path

hence

$$T_w^4 + \frac{k_m}{x\,\sigma\epsilon} T_w - \left(T_c^4 + \frac{k_m T_e}{x\,\sigma\epsilon}\right) = 0 \tag{4-10}$$

In practice $Q_D = \dfrac{\text{diode output per unit area}}{\text{diode efficiency}}$

This data is given in Fig.3-22 as a function of emitter temperature.

Figure 4-3b illustrates the use of the radiation and conduction modes of heat transfer in series. With this type of arrangement, it is possible to have almost all of the temperature drop occur as a consequence of radiation heat transfer and hence, reduce the distortion of the temperature field. If adequate control can be achieved over the emissivities of the radiating surfaces, significant temperature reductions can be achieved in a single step. For example, for a high temperature face at 4,600°R and an emissivity equal to 0.3, transferring heat to a lower temperature face with emissivity equal to 0.9, the low temperature face equilibrates at a temperature below 3,500°R. The exact temperature depends upon the amount of heat being transferred. Hence, it appears feasible that the diode will be able to function simply by radiative heat transfer from the cavity wall to the emitter element, provided that the emissivity values can be maintained constant throughout the desired diode lifetime. The relationship between the high and the low temperature surfaces is given by

$$T_2 = \left[T_1^4 - \left(\frac{1}{\epsilon_1} + \frac{1}{\epsilon_2} - 1 \right) \frac{Q}{\sigma} \right]^{1/4} \qquad (4\text{-}11)$$

where the subscript (1) denotes the higher surface temperature and subscript (2) the lower temperature.

In order to recover heat rejected by the diode collector, the diode heat rejection system must be designed so that during thrusting, all the waste heat available is transferred to the incoming hydrogen, and the unavailable remainder rejected by the diode radiator. Figure 4-4 is a design concept for such a system. The degassing and scavenger chambers shown are necessary to prevent the hydrogen diffusion from the coils to the diode. In the degassing chambers the hydrogen and the metal diffuses out into the vacuum of outer space or the near-vacuum maintained by the scavenger chamber. The scavenger chamber maintains the near vacuum by reacting with any free hydrogen to form a compound which has a very low equilibrium hydrogen pressure at the temperature at which it is maintained. It should be noted that at times it may be best to make the radiator flat rather than cylindrical in order to reduce collector obscuration. The rate of power recovery from the thermionic system is given by

$$Q_{recovered} = 1{,}055\ \dot{w}\ \overline{C}_p\ \Delta T_H \text{ watts}$$

ΔT_H = increase in hydrogen temperature, ^{o}R

$\dot{w}$ = hydrogen flow rate to cavity, pounds/sec.

$\overline{C}_p$ = mean specific heat of hydrogen over temperature range of interest

= 3.5 BTU/pound

For ideal case

$Q_{recovered}$ = waste heat rejected by diode

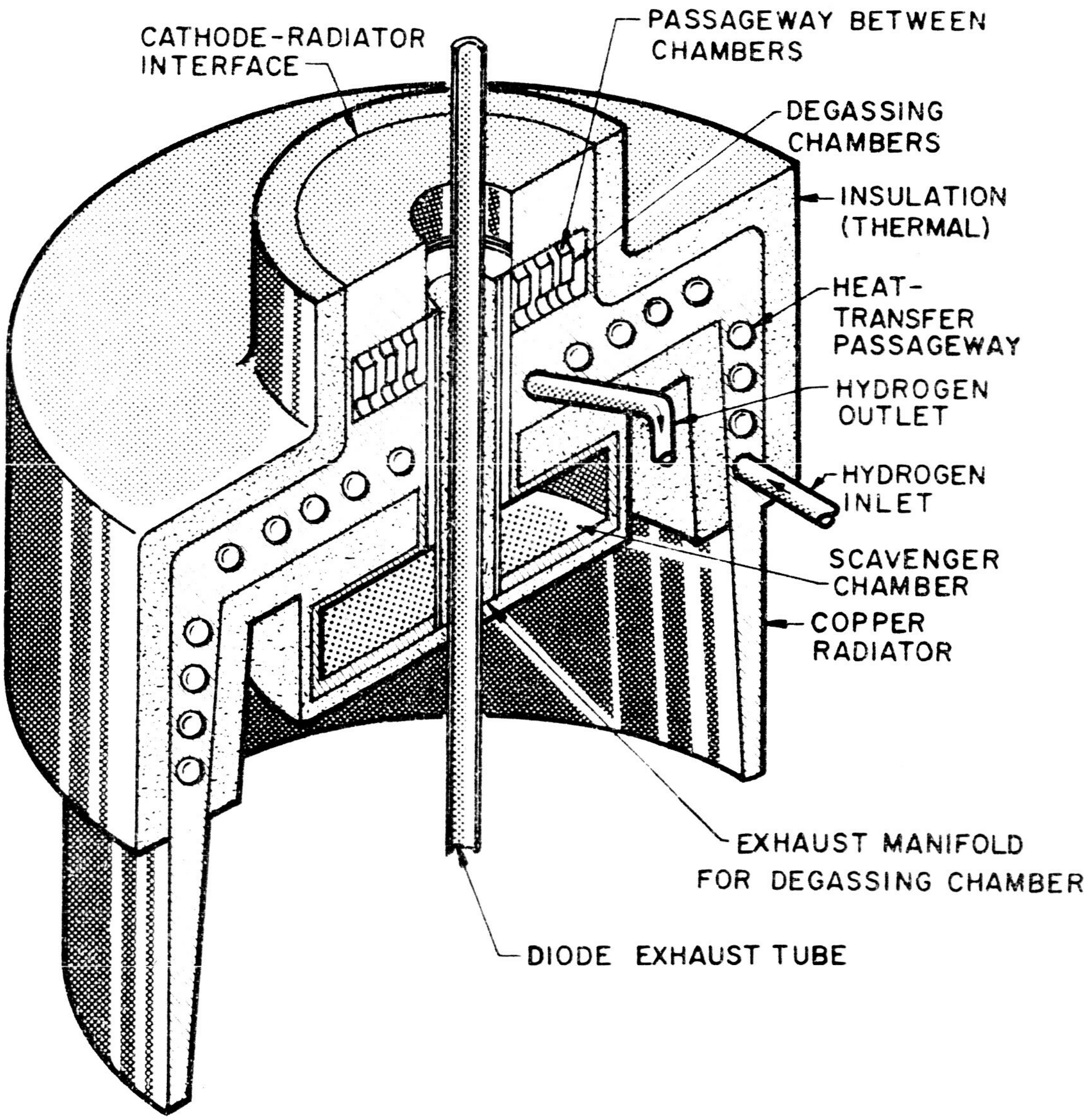
CATHODE-RADIATOR INTERFACE
PASSAGEWAY BETWEEN CHAMBERS
DEGASSING CHAMBERS
INSULATION (THERMAL)
HEAT-TRANSFER PASSAGEWAY
HYDROGEN OUTLET
HYDROGEN INLET
SCAVENGER CHAMBER
COPPER RADIATOR
EXHAUST MANIFOLD FOR DEGASSING CHAMBER
DIODE EXHAUST TUBE

FIG. 4-4 INTEGRAL REGENERATIVE AND RADIATION COOLED DIODE HEAT REJECTION SYSTEM

Since

Output Power, $P = \eta_D Q_D$ where η_D = diode efficiency

It follows that for the ideal case (full recovery):

$$(1-\eta_D)\ Q_D = 1055\ \dot{W}\ \bar{C}_p\ \Delta\ T_H$$

Since the hydrogen enters at about 50°K, and the collector operates at about 1000°K, if a 25°K temperature difference is assumed, the maximum practical $\Delta T_H \approx 1670^{\circ}R$.

Therefore, in the limit;

$$Q_{recovered} = 6.2 \times 10^6\ \dot{W}\ \text{watts}$$

Since by definition,

$$\text{Mass Flow Rate, } \dot{w} = \frac{\text{Thrust}}{\text{Specific Impulse}} = \frac{F}{I_{sp}}$$

An expression for the relationship between electrical output and propulsion from waste heat can be derived:

$$(1-\eta_D)\quad Q_D = 6.2 \times 10^6\ \frac{F}{I_{sp}} \tag{4-12}$$

Hence,

$$\frac{(1-\eta_D)}{\eta_D}\ P = 6.2 \times 10^6\ \frac{F}{I_{sp}} \tag{4-13}$$

Under optimum conditions, η_D = .15 and I_{sp} = 500 sec. for the case where the hydrogen outlet temperature is limited to reheat by the diode collector. The relationship between thrust and electrical power becomes:

$$\frac{F}{P} = \frac{(1-0.15)}{0.15}\ \frac{500}{6.2 \times 10^6} = 4.5 \times 10^{-4}\ \text{lbs./watt electrical} \tag{4-14}$$

Another condition for heat recovery is the requirement that the cavity be able to heat the hydrogen to the level required for optimum mission performance. For many missions, the maximum specific impulse is optimum hence the formulation will be in terms of specific impulse.

We define

r = solar distance in AU

η_N = nozzle energy efficiency

g = gravity constant, $\frac{\text{ft.}}{\text{sec.}^2}$

$Q = \frac{\pi D_m^2}{4} \cdot \frac{H_o}{r^2} \cdot \eta_{m-a}$ = total energy absorbed in cavity, watts.

P_j = jet thermal power, watts

P = diode electrical output, watts

Then;

$$Q = P + P_j \tag{4-16}$$

And;

$$\frac{Q}{P} = 1 + \frac{P_j}{P} \tag{4-17}$$

from previous analysis,

$$F = \frac{(1-\eta_D)}{\eta_D} \quad \frac{I_{sp} \; P}{6.2 \times 10^6} \tag{4-18}$$

Since the power in the exhaust jet can be expressed as:

$$\frac{P_j}{F} = \frac{21.8 \; I_{sp}}{\eta_N} \text{ watts/lb. thrust} \tag{4-19}$$

Combining with the previous expression;

$$\frac{\eta_N P_j}{21.8 \; I_{sp}} = \frac{(1-\eta_D)}{\eta_D} \quad \frac{I_{sp} P}{6.2 \times 10^6} \tag{4-20}$$

Therefore,

$$\frac{P_j}{P} = \frac{(1-\eta_D)}{\eta_N \eta_D} \quad \frac{21.8 \; I_{sp}^2}{6.2 \times 10^6} \tag{4-21}$$

and,

$$\frac{Q}{P} = 1 + \frac{(1-\eta_D)}{\eta_N \; \eta_D} \quad \frac{I_{sp}^2}{2.85 \times 10^5} \tag{4-22}$$

If we assume typical performance objectives;

$\eta_D = 0.15$

$\eta_N = 0.80$

$I_{sp} = 800$ sec.

Then,

$$\frac{Q}{P} = 1 + \frac{(.85)}{.80\ (.15)} \ \frac{6.4 \times 10^5}{2.85 \times 10^5} = 17.0\ \frac{\text{watts thermal input}}{\text{watts electrical}} \qquad (4\text{-}23)$$

This implies that in the limit, for a combined propulsion-power system, only about 5.9 percent of the total energy absorbed will be converted into electrical power. Almost all of the remainder will be utilized as propulsive power. The electrical power available with both waste heat recovery and "superheat" of the hydrogen can be expressed in terms of collector size;

$$P = \frac{102\ \eta_{m-a} \left(\frac{D_m}{r}\right)^2}{\left[1 + 3.5 \times 10^{-6}\ I_{sp}^2\ \frac{(1-\eta_D)}{\eta_N\ \eta_D}\right]}\ \text{, watts} \qquad (4\text{-}24)$$

Using the above expression and the following expression for thrust, we obtain,

$$F = 16.5 \times 10^{-6}\ \frac{\eta_{m-a}\ (1-\eta_D)\ I_{sp}\ (D_m/r)^2}{\eta_D + 3.5 \times 10^{-6}\ I_{sp}^2\ (1-\eta_D)/\eta_N} \qquad (4\text{-}25)$$

We can plot these parameters in terms of collector diameter. These results are presented in Figure 4-5, for the following assumed conditions:

$\eta_{m-a} = 0.70$

$\eta_D = 0.15$

$I_{sp} = 500{,}800$ sec.

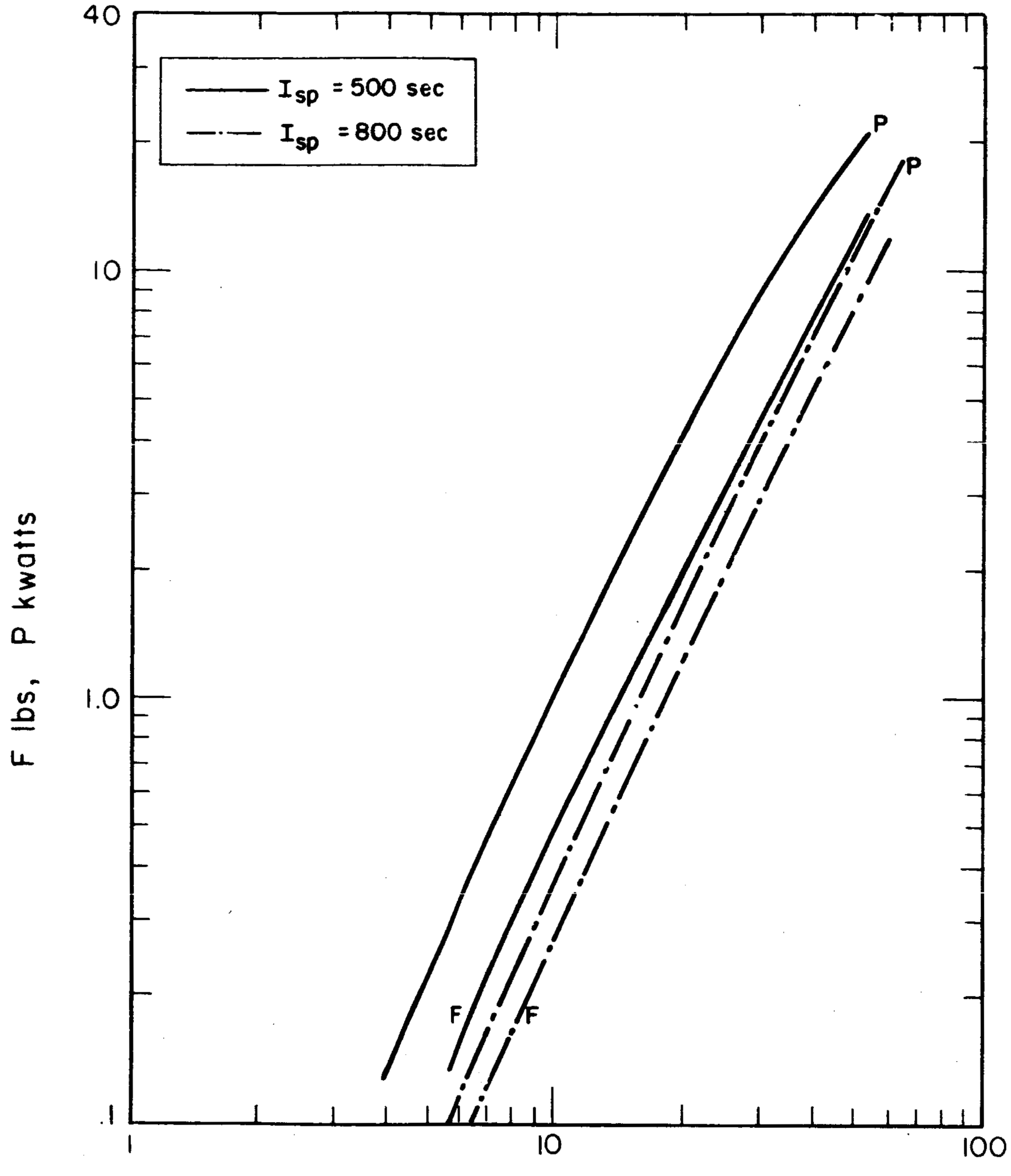

FIG. 4-5 THRUST AND ELECTRICAL POWER OUTPUT VS MIRROR SIZE FOR A SYSTEM WITH 100 PERCENT THERMAL RECOVERY (Absorber Hydrogen Pressure = 2 atm.)

The results indicate that significant amounts of electrical power are available (5-10 kilowatts) and approximately 2-3 lbs. of thrust when using a thirty (30) foot diameter solar collector.

4.5 Startup Operation

The thermal energy storage system can be placed either in the walls of the cavity or in the body of the cavity. It is preferable to place the thermal energy storage system in the rear of the cavity and make the cavity longer rather than wider. This is done in order to keep the projected area of the cavity small and hence the mirror efficiency high. An important function of the thermal energy storage containers is to shield the diode locations from direct solar radiation. One problem area that must be considered specifically is the problem of getting the cavity started. The TES material must be gradually heated up to temperature before the cavity may be considered fully operative.

Enthalpy data for ceramic TES materials show that from 275-525 watt-hrs/lb are required to raise the temperature from ambient to the melting point. For a 300 nm orbit the charge time is 1 hour, and it is presumed that the first 15 min. of time in sunlight will be spent orienting the system.

If;

H_{start} = enthalpy change per unit weight required to bring system to operating temperature

$\bar{t}$ = time required for cavity start up

$\bar{Q}_{start}$ = average rate at which heat is absorbed in cavity during startup phase

then $(H_{start} + H_T)\, W_T$ = enthalpy of TES system when all material is melted.

$\equiv \bar{H}$

and furthermore,

$$\bar{t} = \frac{\bar{H}}{\bar{Q}_{start}} = \frac{(H_{start} + H_T)\, W_T}{\bar{Q}_{start}} \qquad (4\text{-}26)$$

Then for 300 n.mile orbit (from previous analysis),

$$W_T = .00198\ Q_s = 0.00195\ \bar{Q}\ f_{start} \qquad (4\text{-}27)$$

Q = energy normally withdrawn by cavity

W_T is derived by assuming $\frac{Q}{\bar{Q}_T} \equiv f_{start}$ for startup,

Assume

H_{start} = 500 watt hrs/lb.

H_T = 135 watt hrs/lb

Then $$\bar{t} = \frac{.00198\ \bar{Q}_T\ (635)\ f_{start}}{\bar{Q}_{start}} \qquad (4\text{-}28)$$

hence it seems that from 1-3 passive orbits will be required to get the SOHR-SET system fully up to operational temperatures.

4.6 The Hydrogen Diffusion Problem

4.6.1 Hydrogen Diffusion from The Cavity

Due to the relatively high operating temperatures of the SOHR/SET system, some diffusion of the hydrogen working fluid into the solar cavity and thermionic diode are to be expected. The magnitude of the problem is quite difficult to determine without specifying some of the details of the design being considered. However, certain preliminary analyses can be made and acceptable limits estimated on the rate of diffusion.

The principal detrimental effects of hydrogen diffusion on the SOHR/SET system operation are; (a) embrittlement of materials of construction (b) poisoning of cesium diodes and (c) loss of thrust due to loss of working fluid. Typical metals used in the construction of diodes and high temperature containers are; tungsten, tantalum, molybdenum, rhenium, niobium, and titanium. When some of these materials are exposed to hydrogen atmospheres $>10^{-5}$ mm Hg for prolonged periods at the temperatures between 300° and 500°C, embrittlement occurs. Above 500°C the embrittlement is much less pronounced due to outgassing of the hydrogen entrapped in the metal lattice.

Aside from embrittlement, the adsorption of hydrogen on the diode emitter and collector surfaces in the 10^{-4} to 10^{-3} mm Hg range may adversely affect their work functions and thus their performance. Further, if the hydrogen pressure in the diode interelectrode space reaches the 1 mm Hg level, severe degradation of diode performance may occur due to interference with the cesium present for space charge neutralization.

In order to minimize the problem of hydrogen diffusion, it appears desirable that the pressure of the hydrogen in the cavity and other heat exchanger locations, be limited to 10^{-5} mm Hg. With this level as a desirable goal, the apparent diffusion rate will be estimated and the resultant cavity pressure will be compared to the limited data available on the subject. Unfortunately, the available diffusion data are limited to hydrogen-molybdenum, and conclusions with the other refractory metals (which are more likely to be used) will have to be extrapolated from this information.

The diffusion of gases through metals has been treated extensively in the literature, particularly as related to vacuum technology. In Ref. "Scientific Foundations of Vacuum Technique", (Dushman and Lafferty) this problem is treated in detail. At constant pressure, the rate of diffusion increases exponentially with temperature, and from theoretical considerations basic relations were derived, with constants for given gas-metal systems. The following relationship can be used to estimate the rate of diffusion;

$$\log Q_{\mu 1} = C - B/T \tag{4-29}$$

where

$Q_{\mu 1}$ = micron . liters (at 0°C) per cm.^{2}, per minute, per millimeter thickness, at P = 760 mm.

C = a characteristic constant of the gas-metal system and is (C = 4.0679 for $H_2 - M_o$)

B = a constant based on the heat of diffusion and is (B = 4417 for $H_2 - M_o$)

T = temperature in °K

For the most severe operating conditions in the cavity, certain parts of the heat exchanger wall may reach peak temperatures approaching 2500°K (4500°R). Since it is expected that tungsten or tungsten-rhenium alloys will be used at these conditions since molybdenum is not suitable, it will be assumed that the rate of diffusion through molybdenum at lower temperatures (T = 2000°K or 3600°R) will be a reasonable estimate of the behavior of the tungsten/rhenium alloys at the higher temperatures. This is not unreasonable, since the relationship of the operating temperature to the melting point, the ratio of densities, vapor pressures and other physical characteristics, tend to support this qualitative assumption.

Therefore,

$$\log Q_{\mu 1} = 4.0679 - 4417/2000 \qquad (4\text{-}30)$$

$$\log Q_{\mu 1} = 4.0679 - 2.2085 = 1.8594$$

$$Q_{\mu 1} = 72 \text{ micron . liters } (0^{o}C)/cm^{2}\text{-minute}$$
(for 1 mm thickness at 1 atm. pressure)

If we assume a heat exchanger wall thickness of 1.0 mm (.040") and an internal pressure of 1.0 atm., which are typical values, the rate of diffusion into the cavity is approximately;

$$Q = 1 \times 10^{-3} \text{ cm}^{3} \text{ (at } o^{o}C)/cm.^{2} - \text{sec.} \qquad (4\text{-}31)$$

From the kinetic theory of gases, Avogadro's number can be used to estimate the molecular rate of diffusion, with the following result;

$$Q = 1 \times 10^{-3} \times 2.687 \times 10^{19} = 2.69 \times 10^{16} \text{ molecules/cm.}^{2}\text{-sec.} \qquad (4\text{-}32)$$

To evaluate the influence of the above rate of diffusion on the equilibrium pressure in the cavity, we shall first determine the flow regime. The Knudsen number (the ratio of the mean free path of a molecule to a characteristic dimension of the flow channel) is generally used to define the flow regime in low pressure situations as follows:

When:

$L_a/a < 0.01$ flow is viscous

$L_a/a > 1.00$ flow is molecular

$0.01 < L_a/a < 1.00$ flow in transition range

From the reference by Dushman and Lafferty (Table 1.6), the value for the mean free path of hydrogen (corrected for temperature and desired pressure in the cavity) is;

$$L_a = 8.39 \times 10^{-3} \times \frac{2500^{o}K}{273^{o}K} \times \frac{1 \text{ mm}}{10^{-5} \text{mm}} \qquad (4\text{-}33)$$

$$L_a = 7.7 \times 10^{3} \text{cm.}$$

Since the characteristic dimension of the cavity (such as the cavity aperture diameter) will normally cover the range of 1-10 cm. for almost all applications, it can be assumed that free-molecule flow ($L_a/a > 1.0$) will always exist for cavity pressures as high as 10^{-2}mm Hg.

The typical configuration of solar cavity-absorbers tends to approximate an isothermal vessel containing a gas at low pressure, with an orifice in one wall. For a simple approximation it will be assumed that the walls of the cavity do not impede or affect the conductance of the orifice. If the external pressure is assumed to approach zero in space, then the total rate of flow out of the cavity, in molecules/sec is given by;

$$\frac{dN}{dt} = \frac{1}{4} \; v_a \; A \; n \qquad (4\text{-}34)$$

where

v_a = average molecular velocity $= \left(\frac{8 R_o T}{\pi M} \right)^{1/2}$, cm./sec.

A = orifice area in cm^2

n = density of molecules = $9.66 \times 10^{18} \frac{P_{mm}}{T}$ molecules/cm^3.

At T cavity = 2500^oK,

$$v_a = 14{,}551 \left(\frac{T}{M} \right)^{1/2} = 5.1 \times 10^5 \text{ cm./sec.} \qquad (4\text{-}35)$$

From previous experience with solar cavities incorporating hydrogen heat exchangers, the internal surface area to the cavity opening area is, $S/A \approx 20$. Utilizing the previous results for diffusion into the cavity and effusion out of the cavity we can estimate the equilibrium pressure in the cavity as follows;

$$Q \; . \; S = \frac{dN}{dt} = \frac{1}{4} v_a \; A_n \qquad (4\text{-}36)$$

$$\text{Since, } n = \frac{9.66 \times 10^{18}}{2500^o \; K} \; P_{mm} = 3.86 \times 10^{15} \; P_{mm} \qquad (4\text{-}37)$$

$$P_{mm} = \frac{4Q(S/A)}{3.86 \times 10^{15} \; v_a} \qquad (4\text{-}38)$$

$$P_{mm} = \frac{4 \times 2.69 \times 10^{16} \times 20}{3.86 \times 10^{15} \times 5.1 \times 10^5} \qquad (4\text{-}39)$$

Therefore,

$$P_{mm} \approx 1 \times 10^{-3} \text{ mm } H_g \qquad (4\text{-}40)$$

It is believed that this result is particularly significant, since the estimate is based on the rate of diffusion through molybdenum, which is expected to be much more susceptible to hydrogen diffusion than the tungsten/rhenium alloys. Therefore, the estimate is very encouraging as to the feasibility of the SOHR-SET concept, and the compatibility of the thermionic diodes with the hydrogen heat exchanger. However, this simple analysis must be verified and strongly implies the need for an experimental program to obtain basic data on the rate of diffusion of hydrogen in tungsten/rhenium alloys at temperatures up to 2500°K.

4.6.2 Hydrogen Diffusion From the Thermal Recovery System

The very fact that diode waste heat is to be recovered implies that the recovery device must be connected to the diode collector by some heat transfer path. In order that the diode operate effectively, hydrogen diffusion through this path from the heat transfer coils to the collector must either be eliminated entirely, or reduced to a tolerable level.

Our preliminary analysis will be directed towards defining the criteria for a "tolerable level." As discussed previously, it is desirable that the partial pressure of hydrogen in the cesium plasma be less than 10^{-5} mm of mercury. This establishes the condition that the hydrogen concentration in the diffusion medium adjacent to the diode plasma never exceed a value C;

$$C' = k\ (10^{-5}\ \text{mm Hg})^{1/2} \qquad (4\text{-}41)$$

where C' is determined from the expression for solubility of a diatomic gas in contact with a metal

$$C = kp^{1/2}$$

C = concentration of hydrogen per unit volume of metal

k = proportionality constant

p = partial pressure of hydrogen in contact with the metal

In further discussions we will assume that the hydrogen heat transfer coils are imbedded in a high conductivity matrix and that in some manner,either directly or indirectly,by means of an interposed metal element--the diode waste heat is transferred to this matrix. Actually as will be shown later by analysis, the nature of the conducting medium is not very important from the standpoint of controlling diffusion by desorption, the geometrical considerations predominate.

The rate of heat flow from the collector to the recovery device will be inversely proportional to the heat transfer path length between collector and coils and proportional to the cross sectional area of flow. Unfortunately, due to the analogy between diffusion and heat transfer, these conditions also favor diffusion. There is, however, one aspect of diffusion on which we may rely, and that is the relationship between the concentration of hydrogen on a metal surface and the partial pressure of hydrogen in the space adjacent. We note that as $p \to 0$, then $C \to 0$. Thus if the metal surface is exposed to a vacuum, the hydrogen will desorb into the vacuum in order that the surface concentration approach zero. Since the gross desorption rate is necessarily proportional to the surface area over which it occurs, then for simultaneous diffusion and heat conduction along bars, rods, thin hollow cylinders and similar geometries the heat transfer will not be affected, but diffused material will desorb to a vacuum if one is present. We will now assume that the heat transfer path allows desorption and proceed to analyse the problem quantitatively. The differential equation for the system (Fick's Law) is,

$$\frac{\partial C}{\partial t} = D \nabla^2 C\ (x,\ y) \qquad (4\text{-}42)$$

C = hydrogen concentration per unit volume of metal
D = Diffusivity of hydrogen in metal
t = time
x = Coordinate along length of flow path
y = coordinate along width of flow path

Since we are considering steady state diffusion the equation reduces to La Place's eqn. in two dimensions,

$$\frac{\partial^2 C}{\partial x^2} + \frac{\partial^2 C}{\partial y^2} = 0 \qquad (4\text{-}43)$$

Note that we need only consider a strip of thickness ℓ and width unity and that for our purposes it may be regarded as semi-infinite along y. The boundary conditions are thus

$$C\ (-\ell/2, y) \equiv C\ (\ell/2, y) = 0 \qquad (4\text{-}44)$$
$$C\ (x, 0) = C_o$$

If there was no diffusion of hydrogen away from the conducting matrix, then the equilibrium concentration of hydrogen in the metal would be $kp_c^{1/2}$, where p_c is the pressure of hydrogen in the heat transfer coils. Since there is diffusion then,

$$C_o < k\ p_c^{1/2}$$

Since Fick's Law implies that a concentration gradient exists in the conducting matrix if a hydrogen flow exists.

As an example, assuming a matrix of copper at collector temperature (1000°K) (Donald P. Smith, "Hydrogen in Metals", University of Chicago, 1958) gives the solubility of hydrogen in copper as 0.533×10^{-2} cm^3/gm (4.7 cm^3 H_2 at STP/cm^3 of copper) for hydrogen at 1 atmosphere pressure. From Carslaw and Jaeger (H.S. Carslaw and J.C. Jaeger, "Conduction of Heat in Solids", Oxford University Press, 1959 pgs. 162-166) we obtain the heat transfer analogue which yields:

$$C/C_o = \frac{2}{\pi}\ \tan^{-1} \frac{\sin\ (\pi x/1)}{\sinh\ (\pi y/\ell)} \qquad (4\text{-}45)$$

From symmetry or other considerations it may be shown that the maximum value of C/C_o is along $x = 1/2$

$$(C/C_o)\ x = \ell/2 = \frac{2}{\pi} \tan^{-1} \frac{1}{\sinh(\pi y/\ell)} \quad . \quad (4\text{-}46)$$

The value of C/C_o decreases rapidly as $y/1$ increases. For $y/1 = 1$, $C/C_o = .556 \times 10^{-1}$ whereas for $y/\ell = 10$, $C/C_o = .320 \times 10^{-13}$. Thus at 10 thickness along the strip the concentration is substantially reduced and by making the ratio of y/ℓ large enough we can achieve any degree of concentration reduction desirable and still have a physically rational system. One possibility for a simple solution to this problem, is to bond the collector to the heat exchanger with a suitable layer of high conductivity porous metal. This approach provides a satisfactory heat transfer path and allows any back diffusion of hydrogen to desorb from the system before reaching the collector, thereby maintaining an acceptably low hydrogen concentration.

5. DEPLOYMENT, INITIAL ORIENTATION, STATION KEEPING

5.1 Deployment and Initial Orientation

Once the SOHR-SET spacecraft has been inserted into a parking orbit, the subsystems must be deployed in the working configuration and oriented. There are a variety of ways for achieving initial deployment. The components may be spring loaded, or they may be deployed by electrical pneumatic or hydraulic actuators. Initial orientation may be achieved by reaction jets powered by high pressure gases such as hydrogen, or nitrogen.

During this initial period, all electrical power requirements must be met by an independent power supply. The power required during the deployment and orientation periods is expected to be very modest, and is definitely of a short duration. (It should be noted that for current spacecraft peak power required during the deployment and orientation phases has not exceeded 200 watts.)* Using silver zinc batteries, the deployment power supply should be less than 10 pounds.

One may wonder as to the feasibility of preheating the thermal storage material before launch, and using this as a means of providing electrical energy during the deployment and orientation phases. This could conceivably be done, but introduces several problems, such as the oxidation of the cavity and materials of construction since they will be oxidized in air. Furthermore, one has to worry about heat rejection for the diodes. Hence, some accommodation would have to be made for the heat rejection to take place while the space craft is in the undeployed state. All of these factors would complicate the design, and as a consequence reduce its reliability.

---

* Private communication C. Cummings.

5.2 Station Keeping

Station keeping capabilities are definitely within the scope of the SOHR-SET system. For example, in the case of a 24-hour satellite, SET diodes could provide sufficient power for signal reception and transmission equipment, while the SOHR propulsion system would provide hot hydrogen for use in vectorable nozzles for orbit correction altitude stabilization of antennae and the solar collector. For very long lifetime satellites, the SET diodes might be used to supply power for small orbit and altitude stabilization electric thrustors.

The two basic types of propulsion requirements for satellite station keeping are: sustaining propulsion for high drag-low altitude orbits, and correcting maneuvers for position maintenance for a 24 hour satellite. The former application, while feasible for solar propulsion, is less desirable because the solar collector contributes very significantly to the drag problem, and the fraction of sun to dark time is relatively low, hence limiting the available power for the system. The requirements for the 24-hour satellite appear much more compatible with the SOHR-SET operating characteristics. The thrust requirements are relatively modest, and the fraction of darktime is relatively large (5 percent of the time) thereby only slightly decreasing the power available for use during sunlight. Section 6, The Suitability of the SOHR-SET for a 24-hour Satellite System is further examined.

6. DESIGN FOR A 24-HOUR SATELLITE SYSTEM

6.1 System Considerations

Data for the discussion in this section is taken from the orbit studies in section 7.4. This preliminary design is based on the launch capability of the Centaur launch vehicle which is expected to be operational early in 1965, thus it will be available for the launching of future systems. The Centaur is capable of placing 8,500 lbs. in a 300 n. mile orbit. The specific impulse level selected for the SOHR propulsion system is 700 sec. and corresponds to a temperature level of about 2000°K. This temperature level was chosen because it is more compatible with available materials for extended duration. This is not to imply that higher specific impulse values are unattainable, in practice an operating temperature range of 2000°K-2500°K (a specific impulse of about 750 sec.) may be considered for a transfer mission of a spacecraft from a 300 n.mile orbit to a 24 hr. synchronous orbit. The system is based on the use of a 9 1/2 ft. electroformed nickel solar collector similar to the type currently being developed by the Jet Propulsion Laboratory for an advanced solar-thermionic generator (JPL Spec. GMP-34211-DTL,Nov. 1963) to be developed by EOS. The cavity of the system is designed to absorb a minimum of 6000 watts and to deliver 400-600 watts of electrical power at 3.0 volts (nominal) for space operation near the earth. In the system under consideration, a major factor is the duration of the transfer or the transit time. One factor affecting this choice is the amount of electrical power required for station keeping and other purposes while the spacecraft is being transferred to the 24 hour synchronous orbit. The thrusting capacity can be increased slightly at the expense of electrical power capacity. If continuous thrust is desired during the orbit transfer, thermal energy storage must be utilized. Therefore, as the orbit altitude increases, a smaller fraction of the total thermal energy received by the cavity is required for storage for the dark part of the orbit. Hence, the rate of energy removal and the thrust can be increased as the orbit altitude increases. The electrical power available has a similar characteristic with orbit altitude. In the section on thermal energy storage, it was pointed out that due to earth shadow considerations, 37.1 percent of the available thermal energy received, must be stored during sunlight operation at 300 n. mile whereas only 5.2 percent has to be stored at the synchronous orbit. Also pointed out, was that due to this consideration maximum energy utilization results if the thrust is varied accordingly to utilize the available energy to the fullest extent. However, the gain in transit time to be achieved by this technique may not be worth the added system complexity. If the initial thrust acceleration was originally about 1×10^{-4} g. then for a 50 percent thrust increase the transit time decreases by much less than 25 percent. Furthermore since the propellant ratio has only a very weak dependence on initial thrust acceleration, then no gain is achieved for the payload ratio. A negligible gain in payload capacity could be achieved by intermittent thrusting to eliminate TES, but the effect of thermal cycling would be deleterious on the system. Therefore, the use of a reduced thrust system with thermal energy storage is suggested. A gain in the overall Centaur-SOHR-SET system transit-time capability may presumably be achieved by optimising the altitude for the parking orbit. This optimization is suggested by the observation that as the altitude increases, the weight that may be placed in orbit by any given booster decreases, whereas the thrust capability of the solar propulsion system increases.

The initial thrust acceleration was chosen to be about 1×10^{-4} g; inasmuch as the thrust requirements are compatible with a reasonable number of 9 1/2 ft. collector modules. Another consideration for choosing 1×10^{-4} g is that a 40 day transit time seems tolerable. However, forty (40)days is not intended to be an optimum time. Optimization will have to be based on the transit time that will result in minimum system cost per unit of operational time of a given quality system, and is beyond the scope of this study.

The next consideration will be the thermal and electrical power characteristics for a single module. For an optimum system, these may depend on their relative importance. If for example, electrical power is very important, then the spacecraft may start out with maximum available electrical power at the 300 n.mile orbit and the thrust will increase as additional thermal power becomes available at higher altitudes. One important mode of operation is the case where the diode output is reduced to a fraction of its rated value during transit and literally all the energy used for thrusting during this phase. This is possible if the diode emitter electron cooling is reduced by changing the impedance in the load circuit to reduce current flow. By this means, the energy withdrawn by the diode may be reduced to a value as low as 20 percent of the nominal.

Assuming the use of the 9 1/2 ft. collector, the cavity will absorb thermal power at the rate of 6000 watts. At the 300 n.m orbit, about 3,780 watts will be available for direct use, the remainder goes to the TES system. At the 24 hour synchronous orbit, 5,690 watts will be available for direct use with only a small fraction going to the TES system. The electrical power output capacity for the system while in the 24 hour orbit is thus a maximum of about 550 watts. With diodes operating at 20 percent capacity, the thermal power available for thrusting at 300 n.m orbit is (3,780-110) = 3,670 watts.

To estimate the number of modules required, we note that the initial weight, m_o is 8500 lbs. and the desirable initial thrust to weight is 1×10^{-4}. Hence required thrust is approximately $F \approx 8,500 \times 10^{-4} = .85$ lbs. From Fig.3-20 along the $P_o = 2$ atm curve we obtain $\eta_N = 0.75$ hence

$$\text{thrust per unit} = \frac{(\text{watts available to jet})\ \eta_N}{21.8\ I_{sp}} = \frac{3{,}670 \times 0.75}{21.8 \times 700} \cong 0.2 \text{ lbs.} \qquad (6\text{-}1)$$

and number of units = 4.

The total power available for propulsion from (4) units is thus 14,700 watts, hence thrust is about 0.8 lbs. and the initial thrust acceleration is 0.95×10^{-4}g.

From Fig. 7-15 we find that the mission time is 40 days; from Fig. 7-11 the propellant ratio is shown to be 0.48. The propellant weight is thus 4,080 lbs. The mirror + support weight is estimated to be about 50 lbs., the cavity and thermionic diodes (exclusive of thermal energy storage) is estimated to be about 15 lbs, the deployment mechanism is estimated to be 15 lbs., the tankage weight 420 lbs., the meteoroid shield weight 210 lbs., the thermal insulation weight 50 lbs., and the thermal energy storage system is 30 lbs. Hence the payload plus other equipment is about 3300 lbs.

The payload estimate also includes accessory equipment such as batteries, power conditioning, command and control, and associated structure. Orbit and attitude stabilization has not been accounted for in this system analysis; the necessary hardware has to be deducted from the 3300 lb. payload calculated here. It is conceivable that residual propellant could be utilized for station keeping, thereby allowing the SOHR components to be used in conjunction with orbit and attitude stabilization. Listed below for convenience is a summary of the system performance characteristics. It should be noted that about 39 percent of the initial weight is "payload" delivered to the synchronous orbit by a relatively simple propulsion system. If a specific impulse of 500 sec. had been used instead of 700 sec. then the payload would be reduced to about 2200 lbs., and the thrusting could be achieved by thermal recovery only, without any superheat in the cavity. Thus, for about a 30 percent payload reduction we can bypass the hydrogen diffusion problem, and other complexities related to incorporating the superheater in the cavity thermal energy storage compartment.

TABLE 6-1
SUMMARY OF SYSTEM PERFORMANCE CHARACTERISTICS

Launch Vehicle = Centaur

Type Collector = Electroformed Nickel 9 1/2 ft. diameter collector

Thermionic Generator = EOS (16) diode generator

Number of Modules = Four (4)

Total Electrical Power output = 2,200 watts at 3 volts (nominal) at the synchronous orbit

Total thrust = 0.8 lbs.

Specific impulse = 700 sec.

Initial thrust acceleration = 0.95×10^{-4} g

Mission time = 40 days

Initial weight = 8,500 lbs.

Propellant weight = 4,080 lbs.

Mirror + support = 50 lbs. x (4) = 200 lbs.

Cavity and Thermionic diodes = 15 lbs. x (4) = 60

Thermal Energy Storage = 30 lbs x (4) = 120

Deployment mechanism = 15 lbs. x (4) = 60

LH_2 Tank weight = 420

Meteoroid shield weight = 210

Thermal insulation weight = 50

Total Fixed Weight = 1120 lbs.

Net Payload* ≈ 3300 lbs.

Payload*/initial weight = 0.39

*Includes payload plus accessory equipment.

6.2 Preliminary Design of Combined Cavity Absorber for 24-Hr Orbit

A preliminary design of the combined cavity absorber for a 24 hour satellite system was evaluated as part of the study. The design concept shown in Figure 6-1 , is based on a cavity absorber which integrates a sixteen (16) converter thermionic generator, and a hydrogen heat exchanger which recovers the waste heat rejected by the diode collectors. At typical operating conditions for peak electrical power output, the diode collector reaches temperatures $\geq 1000^{\circ}K$, thereby indicating the feasibility of heating hydrogen regeneratively to temperatures approaching this level with a suitable heat exchanger. Expansion of hydrogen from this temperature level is equivalent to an actual specific impulse, $I_{sp} = 500$ sec. in space. Although not shown in the cross section drawing of Figure 6-1 , a "superheater" coil of refractory tubing could be placed in the thermal storage matrix of the cavity to achieve hydrogen gas temperatures in the range of 2000-2400°K, which would be equivalent to an $I_{sp} = 700\text{-}750$ sec. However, this additional feature requires detailed design to assure compatibility with the thermal energy storage material and the other components in the absorber. Although the performance is reduced at the lower temperatures, (without superheater) additional flexibility in vehicle design is achieved since the lower temperature gas can be ducted to the optimum location for thrust vector control.

The thermionic generator consists of (16) converters mounted radially on a high conductivity cylindrical section to which the hydrogen heat transfer coils are brazed. The coils are enclosed by a removable heat shroud which insulates the heat exchanger during regenerative operation, and can be discarded for thermionic generator operation only. During the latter mode of operation, the coil and cylindrical section (with suitable high emissivity coating) can function as an extended surface radiator for the waste heat rejected by the diode collectors. The collector of each diode must be bonded securely to the cylindrical section for good thermal conductivity, but must be electrically isolated from the common ground to permit the proper series/parallel arrangement

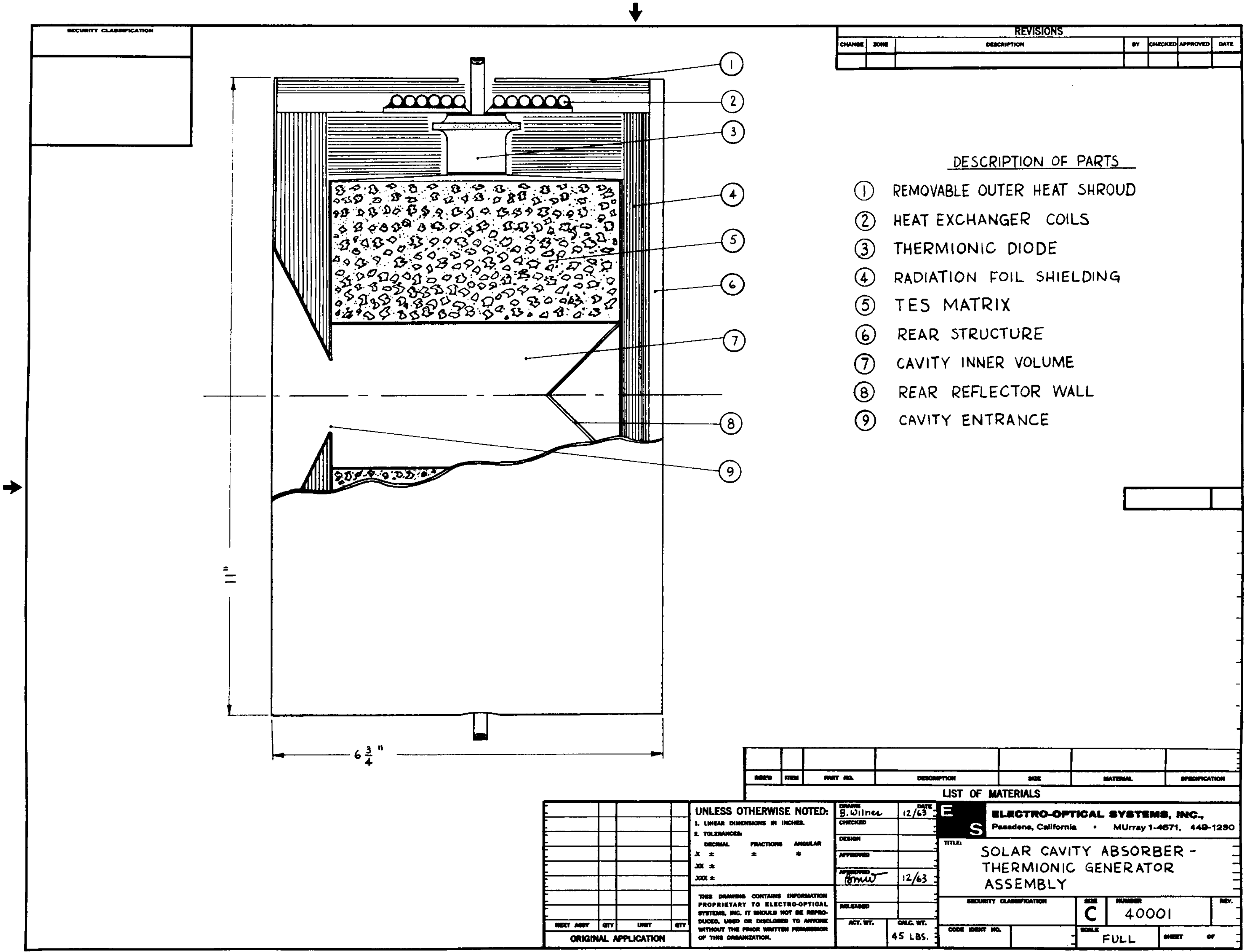
SECURITY CLASSIFICATION
REVISIONS
CHANGE
ZONE
DESCRIPTION
BY
CHECKED
APPROVED
DATE
DESCRIPTION OF PARTS
① REMOVABLE OUTER HEAT SHROUD
② HEAT EXCHANGER COILS
③ THERMIONIC DIODE
④ RADIATION FOIL SHIELDING
⑤ TES MATRIX
⑥ REAR STRUCTURE
⑦ CAVITY INNER VOLUME
⑧ REAR REFLECTOR WALL
⑨ CAVITY ENTRANCE
11"
6 3/4"
LIST OF MATERIALS
UNLESS OTHERWISE NOTED:
1. LINEAR DIMENSIONS IN INCHES.
2. TOLERANCES:
DECIMAL FRACTIONS ANGULAR
THIS DRAWING CONTAINS INFORMATION PROPRIETARY TO ELECTRO-OPTICAL SYSTEMS, INC. IT SHOULD NOT BE REPRODUCED, USED OR DISCLOSED TO ANYONE WITHOUT THE PRIOR WRITTEN PERMISSION OF THIS ORGANIZATION.
DRAWN B. Wilner 12/63
APPROVED 12/63
CALC. WT. 45 LBS.
ORIGINAL APPLICATION
ELECTRO-OPTICAL SYSTEMS, INC.
Pasadena, California • MUrray 1-4671, 449-1230
TITLE: SOLAR CAVITY ABSORBER - THERMIONIC GENERATOR ASSEMBLY
SIZE C
NUMBER 40001
SCALE FULL

FIG. 6-1 SOLAR CAVITY ABSORBER-THERMIONIC GENERATOR ASSEMBLY

of diodes. This feature can be provided by using flame sprayed Al_2O_3 as the joining medium with a suitable metal-ceramic braze for the final bond. The cesium reservoirs of each diode are allowed to extend outside the removable outer heat shroud, thereby controlling temperature at 380-400°C by maintaining equilibrium between conduction down the tube walls and radiation to space.

The inner walls of the cavity absorber are formed by the thermal energy storage matrix which is enclosed in a container of tungsten-rhenium welded sheet stock. As discussed previously, it is anticipated that the TES matrix will consist of a BeO-MgO compound, in the form of small granules coated with a material such as vapor deposited tungsten and the entire mixture will be compacted and sintered to achieve high density. This arrangement provides several desirable features; containment of the TES material in zero gravity, improving the effective thermal conductivity of the matrix, flexibility in forming to complex shapes, and relatively high stability during thermal cycling. In the example shown in Figure 6-1 , approximately 30 lbs of TES material has been integrated in the cavity, sufficient for about 6000 watt-hrs. of thermal storage based on a 24 hr. synchronous orbit. This should be sufficient for full electrical output of the diodes at these conditions. During the sunlight part of the orbit, the energy focused into the cavity is trapped by successive reflections-absorption on the cavity walls and subsequent conduction into the TES material. Several other preliminary design concepts were considered, including one in which the diodes received energy directly by specular radiation and thermal reradiation from the cavity walls. Although this approach appears feasible during the sunlight part of the orbit, serious temperature constraints are placed on the system during the dark part of the cycle. A simplified analysis of the reradiation from the walls of the cavity to the diodes, from energy in the TES material, indicates excessive temperature drops (>500°C) would occur, thereby making the approach impractical. Therefore, the TES was placed between the cavity inner walls and the diodes, providing a more uniform and controllable temperature gradient to the diodes during all phases of operation. In fact, the best of the presently available or known TES materials impose a serious design constraint on the cavity configuration, particularly for the 24 hr. orbit case, where the discharge or dark cycle is relatively long. (1.2 hours).

The remainder of the cavity is enclosed by tungsten, tantalum or moly foil (.001") radiation shielding to minimize thermal losses from the system. Design of this shielding is very critical to the satisfactory operation of the cavity. Special techniques have been developed to "dimple" or corrugate the foil to provide adequate standoff between layers and approach the full effectiveness of the multi-layer shield in vacuum. Analysis has indicated that about 20-30 layers are adequate to prevent excessive losses from the outer surface by radiation to space.

The preliminary design concept was based on a modification of the basic design suggested by the criteria in J.P.L. Specification No. GMP-34211-DTL dated 1 Nov. 1963. EOS is presently under contract to design a (16) converter solar energy thermionic generator designated SET II, for the Jet Propulsion Laboratory. The system is based on the use of (16) "identical" converters operating with an input of 6000 watts thermal to the generator cavity in space at the earth's distance from the sun. It is anticipated that the system will produce 400-600 watts of electrical output, depending on specific operating conditions. As discussed previously, it is anticipated that (4) modules will be capable of providing about 2200 watts of electrical output in a 24 hr. synchronous orbit for a power plant weight of 440 lbs. This is equivalent to a power to weight ratio of 5.0 watts/lb. including energy storage, which is at least a factor of two (2) improvement over conventional solar photovoltaics with electrochemical energy storage.

7. MISSION STUDIES

7.1 Introduction

Due to its simplicity of design, potential high reliability and reasonably high specific impulse (500-800 sec.), the SOHR-SET concept appears ideally suited to the task of providing continuous thrust and electrical power for near-sun space missions. A space mission of particular interest is that in which a probe is sent to within approximately 0.3 Astronomical Units from the center of the sun in order to obtain data regarding the atmosphere and surface of the solar body. In order to justify the use of a SOHR-SET for this type of mission, its performance must be compared with that of current, or foreseeable, propulsion devices. Only two such devices are considered here, namely, the ordinary chemical rocket and the ion engine. In the chemical rocket the thrust is delivered in a single impulse, and in the ion and SOHR-SET systems the thrust acts continuously for a prescribed length of time. The specific impulse (I_{sp}), specific mass of the power plant (α), and engine efficiency(η), assigned to the SOHR-SET and ion engines, are given in Table 7-1 along with the specific impulse for the chemical rocket. Here, $\alpha = M_W/P$, where M_W = mass of the propulsion power plant and does not include part of power plant used to generate electrical power for other than propulsion purposes. P = power delivered to rocket from power supply.

TABLE 7-1
Engine Parameters

	SOHR-SET	Ion Engine	Chemical Rocket
I_{sp}	800 sec.	4000 sec.	400 sec.
α	4 lb/kw thermal	40 lb/kw elect.	---
η	0.6, 0.8	0.63	

The value of α given for the ion engine will, presumably, be achieved with the SNAP-50 power plant (300 kw system).

7.2 Analysis

In order to accomplish the desired mission of passing within three tenths of an Astronomical Unit from the sun, the probe must first escape from the earth. For the ion engine and the SOHR-SET engine the spacecraft is placed into a parking orbit of 1 AU about the sun, and the ion and SOHR-SET engines then act on it to slow it down and spiral it towards the sun. The chemical rocket is considered for the case where it is launched from the parking orbit at 1 AU and for the case where it is launched from a 300 n m parking orbit above the earth.

In the case of the chemical rocket, a single impulse is applied to the probe, in a direction opposite to its motion, such that the resulting ellipse has a perihelion distance equal to 0.30 AU. Refer to Fig. 7-1. The change in velocity required to produce this ellipse is ΔV = 31,300 ft/sec. if the spacecraft is launched from a parking orbit 1 AU from the sun, and 22,300 ft/sec. for the case where it is launched from a parking orbit 300 n m above the earth.

If we assume that the vehicle is a single stage rocket, then the payload plus structure fraction delivered along the ellipse is

$$\frac{M_L + M_s}{M_o} = e^{-\Delta V/(I_{sp} g)} = 0.08716,\ 0.1765 \text{ respectively for the}$$

1 AU and 300 nm parking orbits where

M_L = payload

M_s = structure

M_o = initial mass of vehicle ($M_L + M_s + M_p$)

M_p = total propellant

The time taken to reach perihelion is 95.5 days, which is half the period of the ellipse.

In order for the SOHR-SET, or ion engine, propelled vehicle to fall toward the sun, energy must be removed from the initial orbit over an extended period of time. A simple and efficient way of removing this energy is to maintain the thrust in the plane of the initial orbit, perpendicular to the radius vector from the sun to the probe, in a direction opposite to the probe's motion, refer to Fig. 7-2a. In order to minimize the expenditure of propellant, and thereby maximize the delivered payload, the thrust is terminated at the moment when the perihelion of the subsequent coast ellipse equals the desired 0.30 AU. Refer to Fig. 7-3. For constant thrust, i.e., constant propellant flow rate and constant specific impulse, the power supply and propellant fractions are given, respectively, as follows:

$$\frac{M_w}{M_o} = \frac{I_{sp}\,\alpha}{45.8\,\eta g}\,\frac{F}{M_o} \tag{7-1}$$

$$\frac{M_p}{M_o} = \frac{t_1}{I_{sp} g}\,\frac{F}{M_o} \tag{7-2}$$

where F = thrust, t_1 = time of power flight, g = 32 ft/sec.^{2} The payload plus structure fraction is

$$\frac{M_L + M_s}{M_o} = 1 - \frac{M_w}{M_o} - \frac{M_p}{M_o} \tag{7-3}$$

If the SOHR-SET takes full advantage of the sun's radiation, then the power delivered by the solar concentrator to the engine will vary faster than the inverse of the square of the distance of the probe from the sun, i.e., $P \sim 1/r^2$ represents a rate of power generation which is less than the maximum and at 0.3 AU will be only approximately 70 percent of the true value. The estimation $P \sim 1/r^2$ is, however, adequate for the analysis, and as far as mission time is concerned will give estimates which are very close to the actual values for the maximum thrust case. Having assumed $P \sim 1/r^2$, then since F is proportional to P, $F \sim 1/r^2$ or

$$F = Fo\,(r_o/r)^2 \tag{7-4}$$

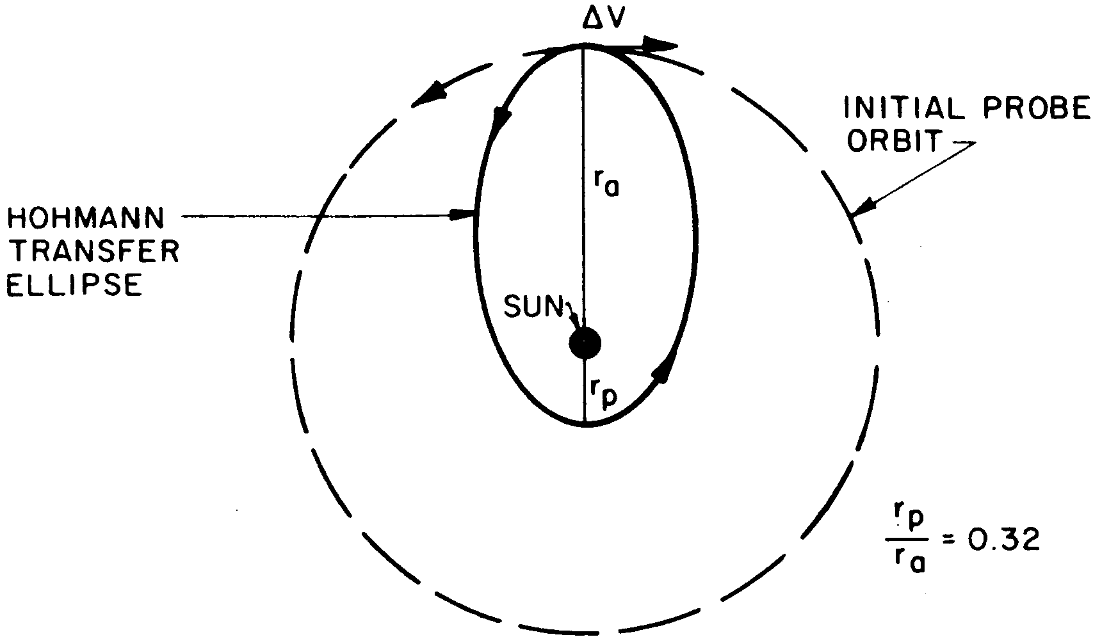
ΔV
INITIAL PROBE ORBIT
HOHMANN TRANSFER ELLIPSE
r_a
SUN
r_p
$\frac{r_p}{r_a} = 0.32$

FIG. 7-1 HOHMANN TRANSFER ELLIPSE FOR CHEMICAL ROCKET
(Parking Orbit = 1 AU)

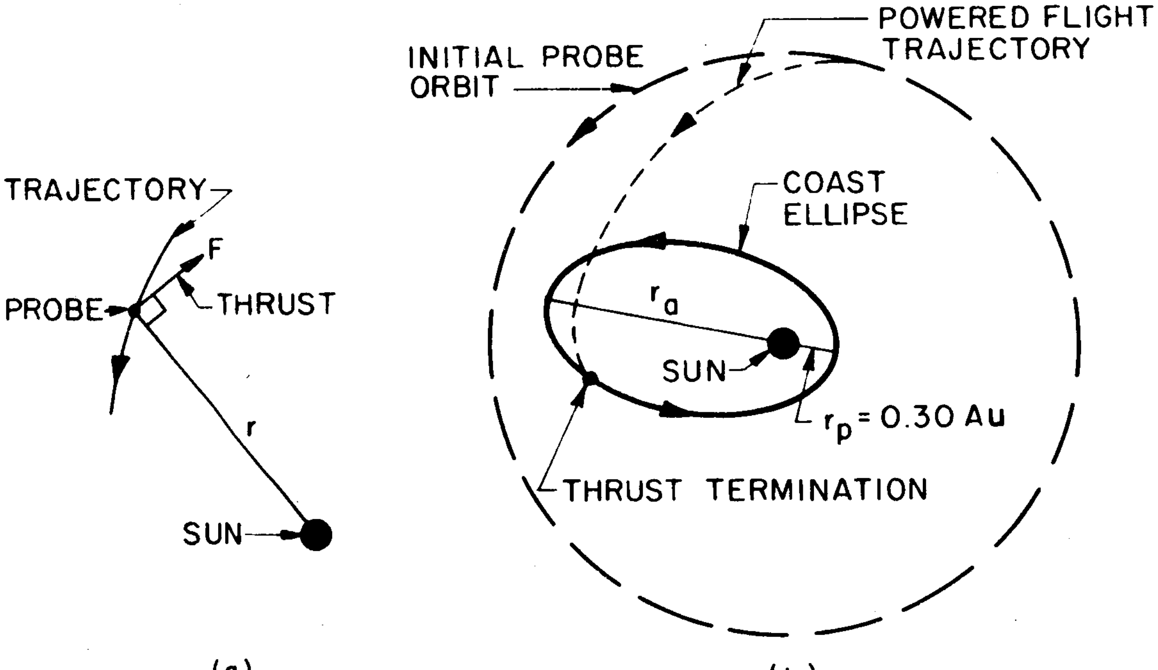
TRAJECTORY
F
PROBE
THRUST
r
SUN
(a)
POWERED FLIGHT TRAJECTORY
INITIAL PROBE ORBIT
COAST ELLIPSE
r_a
SUN
$r_p = 0.30$ Au
THRUST TERMINATION
(b)

FIG. 7-2 COAST ELLIPSE FOR SOHR-SET

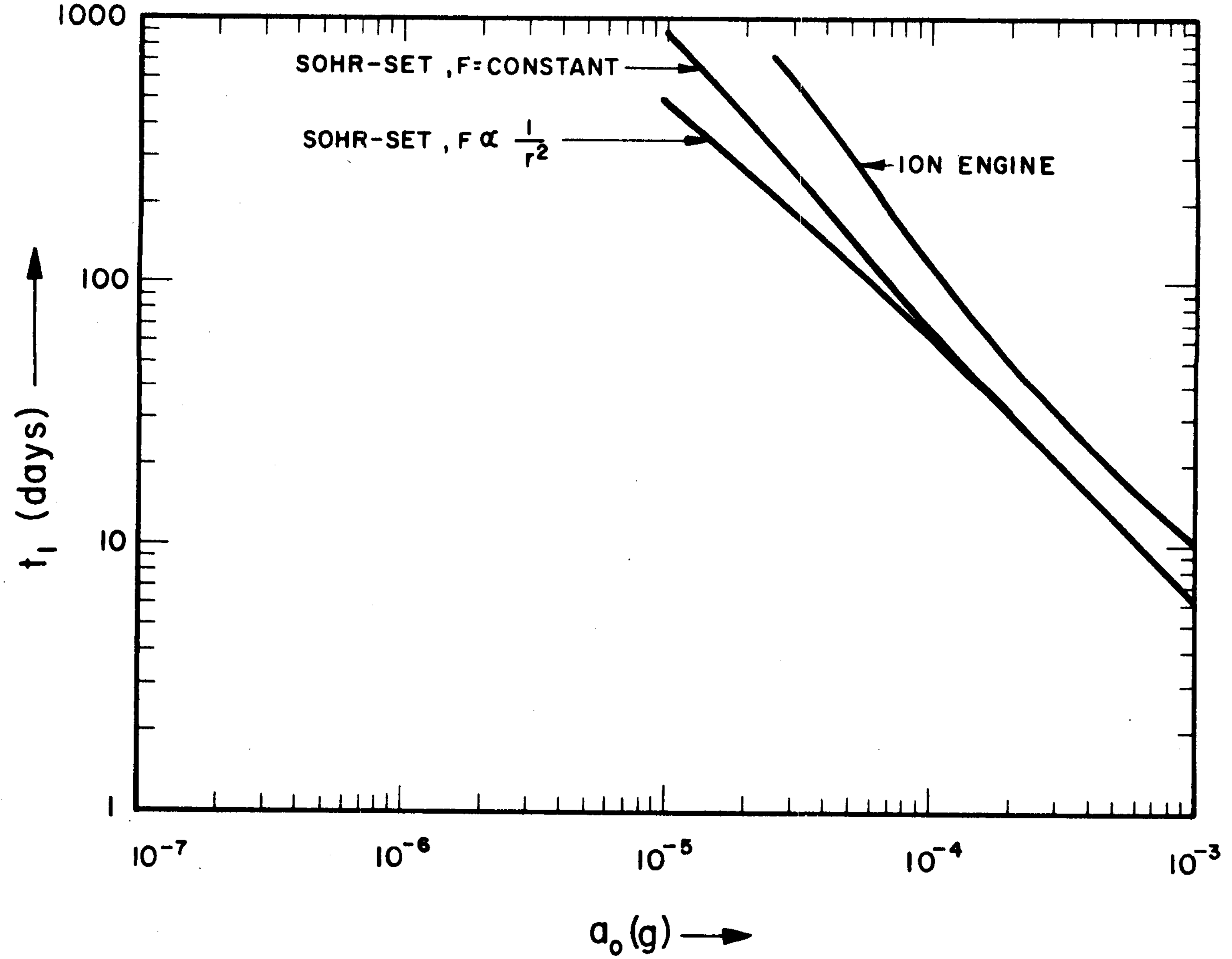

FIG. 7-3 TIME OF POWERED FLIGHT VS INITIAL THRUST ACCELERATION

where $r_o = 1$ AU. Since M_w remains constant during flight, $F = F_o(r/r_o)^2$. The propellant mass fraction is

$$\frac{M_p}{M_o} = \frac{r_o^2}{I_{sp}g} \frac{F_o}{M_o} \int_o^{t_1} \frac{dt}{r^2} \tag{7-5}$$

and the payload plus structure is given by (7-3), where M_p/M_o is now given by (7-5).

The equations of motion (in two dimensions of the probe in the gravitational field of the sun were programmed on an IBM 1620 computer. Trajectories were simulated for values of initial thrust acceleration, a_o, in the range, 10^{-5} g $\leq a_o \leq 10^{-3}$ g. The method of propulsion (SOHR-SET or ion engine) was characterized by the parameters I_{sp} and α, the former appearing in the equations of motion, and the latter occuring only in equation (7-1). Constant thrust was used for both ion engine and SOHR-SET and variable thrust (equation 7-4) for the SOHR-SET. The initial conditions were the same for all trajectories, i.e., a circular orbit about the sun with radius equal to 1 AU.

Figures 7-3 and 7-4 show the time of power flight and distance of the probe from the sun at the instant of thrust termination, respectively, as a function of a_o, for the above three engines. From Fig. 7-3 we see that for a given value of a_o, the powered flight time is longest for the ion engine and shortest for the SOHR-SET variable thrust, as to be expected. Figure 7-4 shows that the ion engine is closest to the sun, and the SOHR-SET variable thrust the farthest, at the instant of thrust termination, for a given value of a_o.

Figure 7-5 shows the power plant mass fraction as a function of initial thrust acceleration for the SOHR-SET and ion engines. The mass fraction for the ion engine equals unity at $a_o = 1.81\ (10^{-4})$ g. The propellant mass fractions are shown in Fig. 7-6. Note that the chemical rocket consumes more propellant than either low thrust device, for $a_o > 5 \times 10^{-5}$ g.

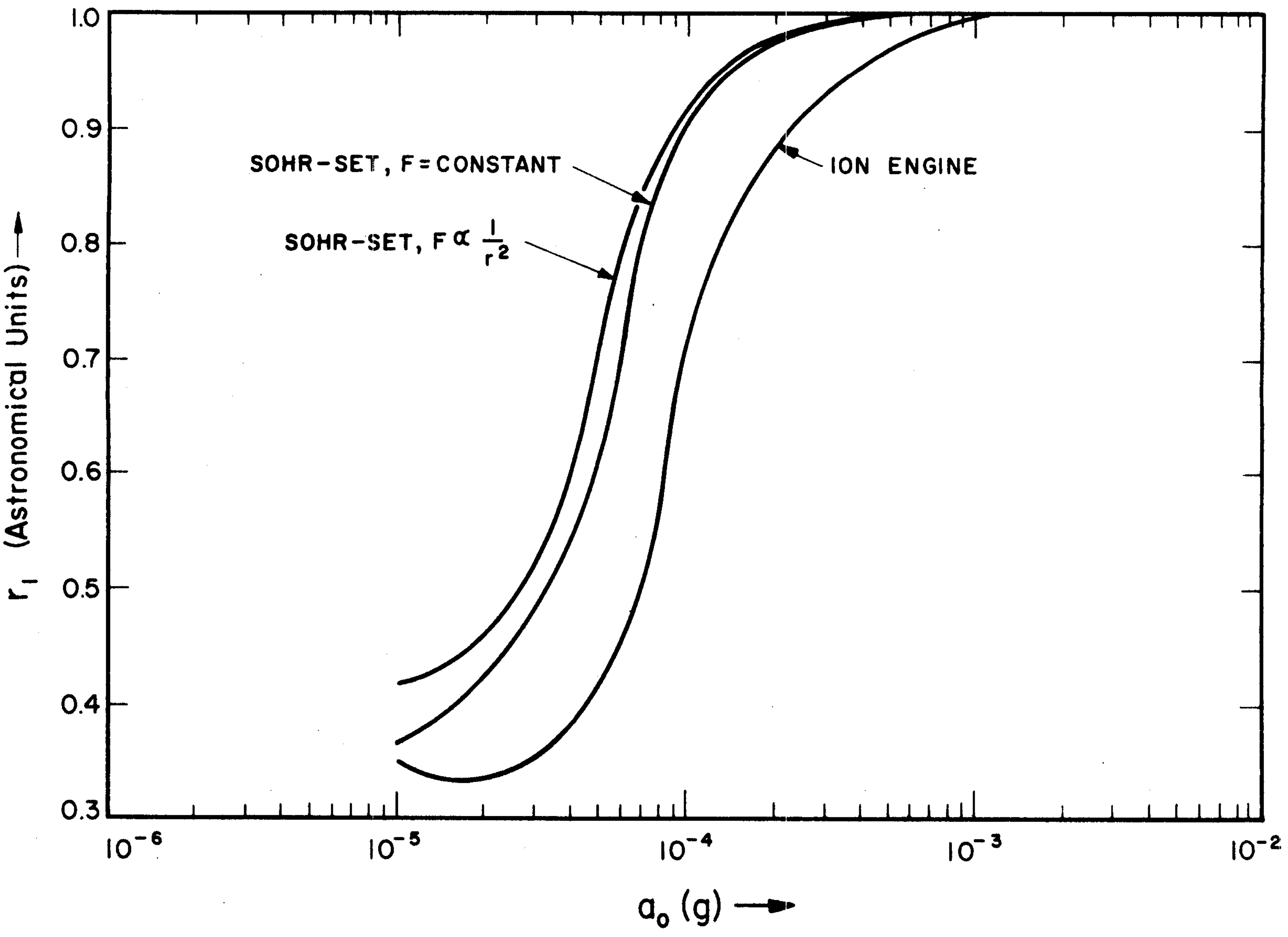

FIG. 7-4 DISTANCE FROM SUN AT INSTANT OF THRUST TERMINATION VS INITIAL THRUST ACCELERATION

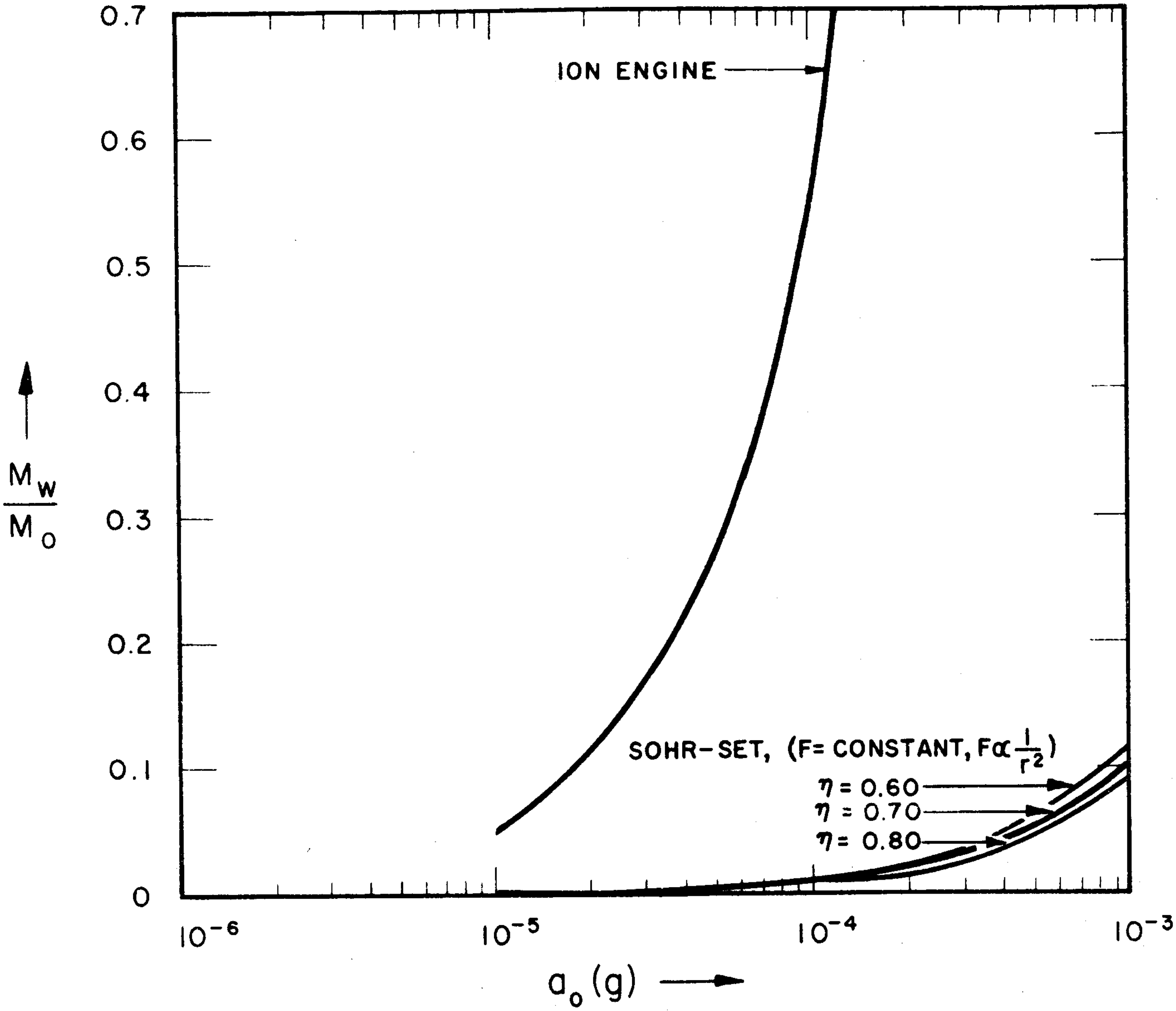

FIG. 7-5 POWER PLANT MASS FRACTION VS INITIAL THRUST ACCELERATION

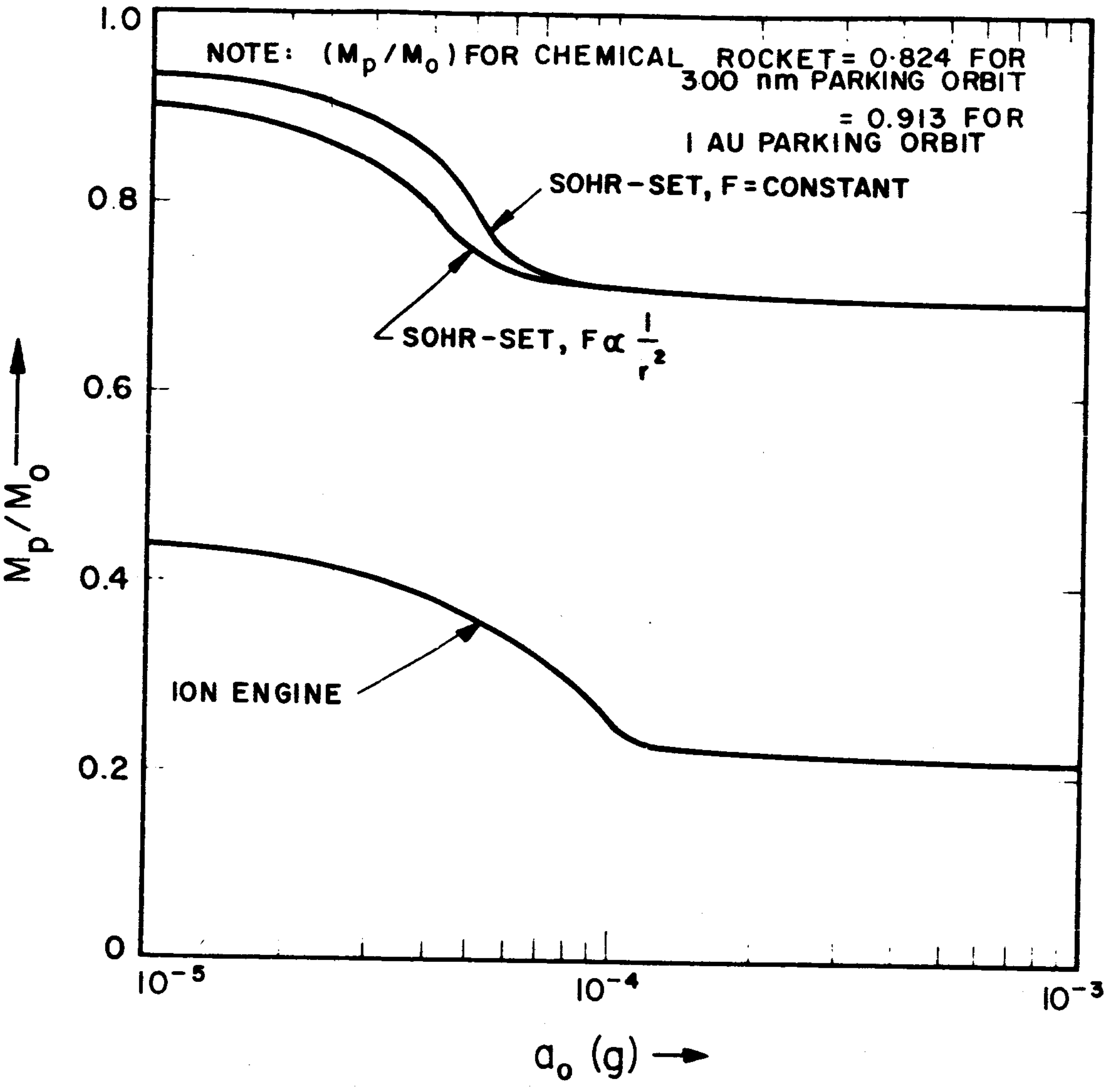

FIG. 7-6 PROPELLANT MASS FRACTION VS INITIAL THRUST ACCELERATION

Employing equ. (7-3), we obtain the payload (plus structure) mass fractions shown in Fig. 7-7. Since $M_w/M_o = 1$ at $a_o = 1.4\ (10^{-4})g$ for the ion engine, therefore the payload fraction is zero beyond this value of a_o. Judging from Fig. 7-7, the payload capability of the SOHR-SET is superior to the ion engine for large thrust accelerations, and inferior for small a_o, the crossover point being at approximately $a_o = 8(10^{-5})g$. Note that the payload delivered by the SOHR-SET variable thrust (eq. 7-4) is greater than that delivered by the SOHR-SET constant thrust only for small values of a_o, i.e., $a_o < 10^{-4}g$. The maximum payload fraction for the chemical rocket is generally less than that of either the SOHR-SET or ion engine.

Equally important as the delivered payload is the time required to perform the mission. The total mission time is the time of powered flight (Fig. 7-3) plus the time taken to go from the point of thrust termination to the perihelion of the coast ellipse refer Fig. 7-2(b). Figure 7-8 shows the total mission time as a function of a_o for the three engines. Note that the mission times for the SOHR-SET are significantly less than those for the ion engine in the region $a_o < 10^{-4}g$. However, this is the region in which the ion engine delivers the larger payload fraction. Clearly, a compromise must be made between payload and mission time.

Having established the probe in an elliptical orbit about the sun, it is of interest to know the properties of this orbit. Two important properties are the period (T) and aphelion (r_a) of the ellipse. These are shown in Figs. 7-9 and 7-10 respectively. From Fig. 7-10 we see that the probe will return to the earth's orbit ($r_a = 1$) only if the vehicle was propelled by the SOHR-SET at initial thrust accelerations exceeding $2(10^{-4})g$.

7.3 Conclusions on Solar Probe Mission

The SOHR-SET (defined in Table 1) is competitive with the ion engine (defined in Table 7-1) in both payload and mission time, for the solar probe mission. The ion engine cannot deliver a payload

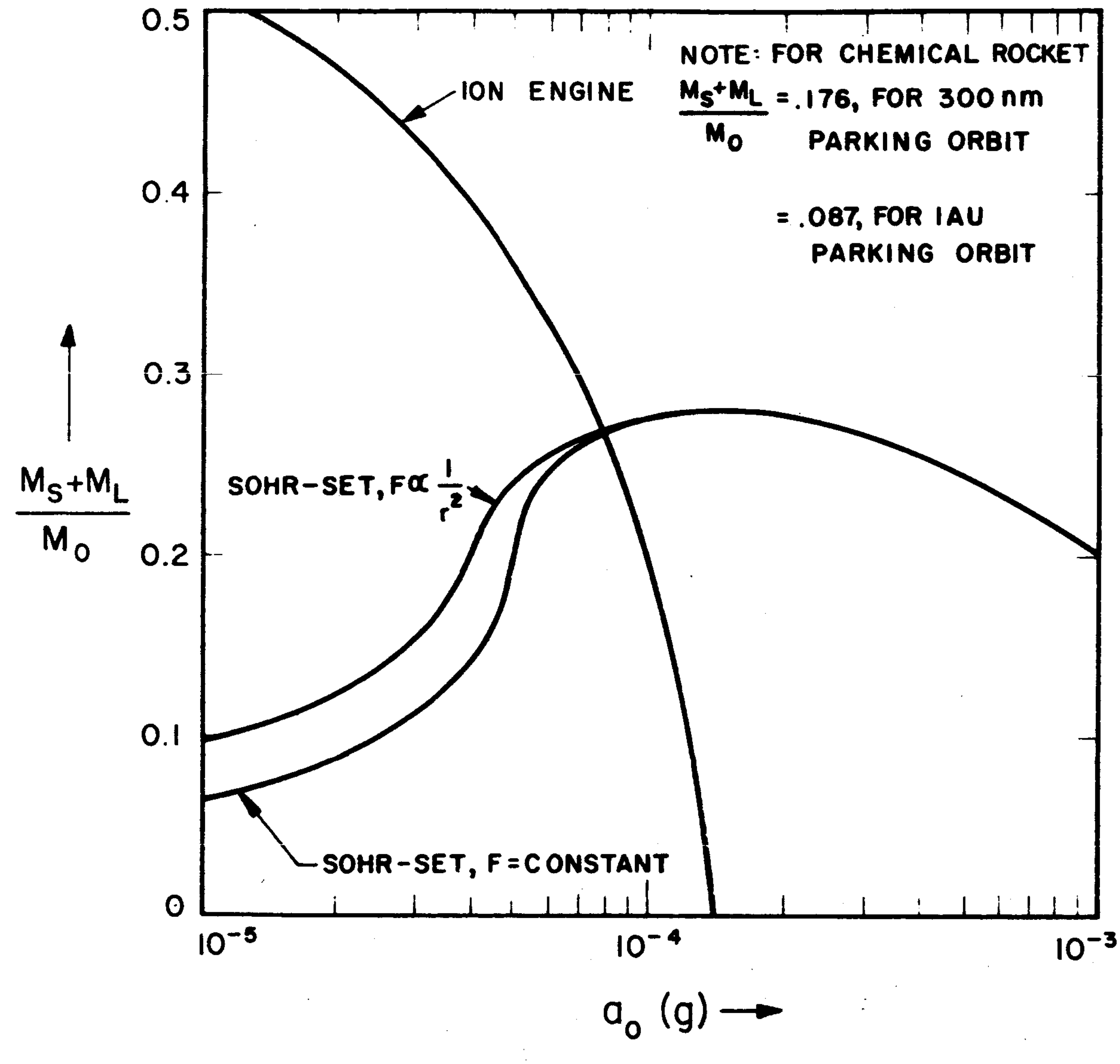

FIG. 7-7 PAYLOAD PLUS STRUCTURE MASS FRACTION VS INITIAL THRUST ACCELERATION

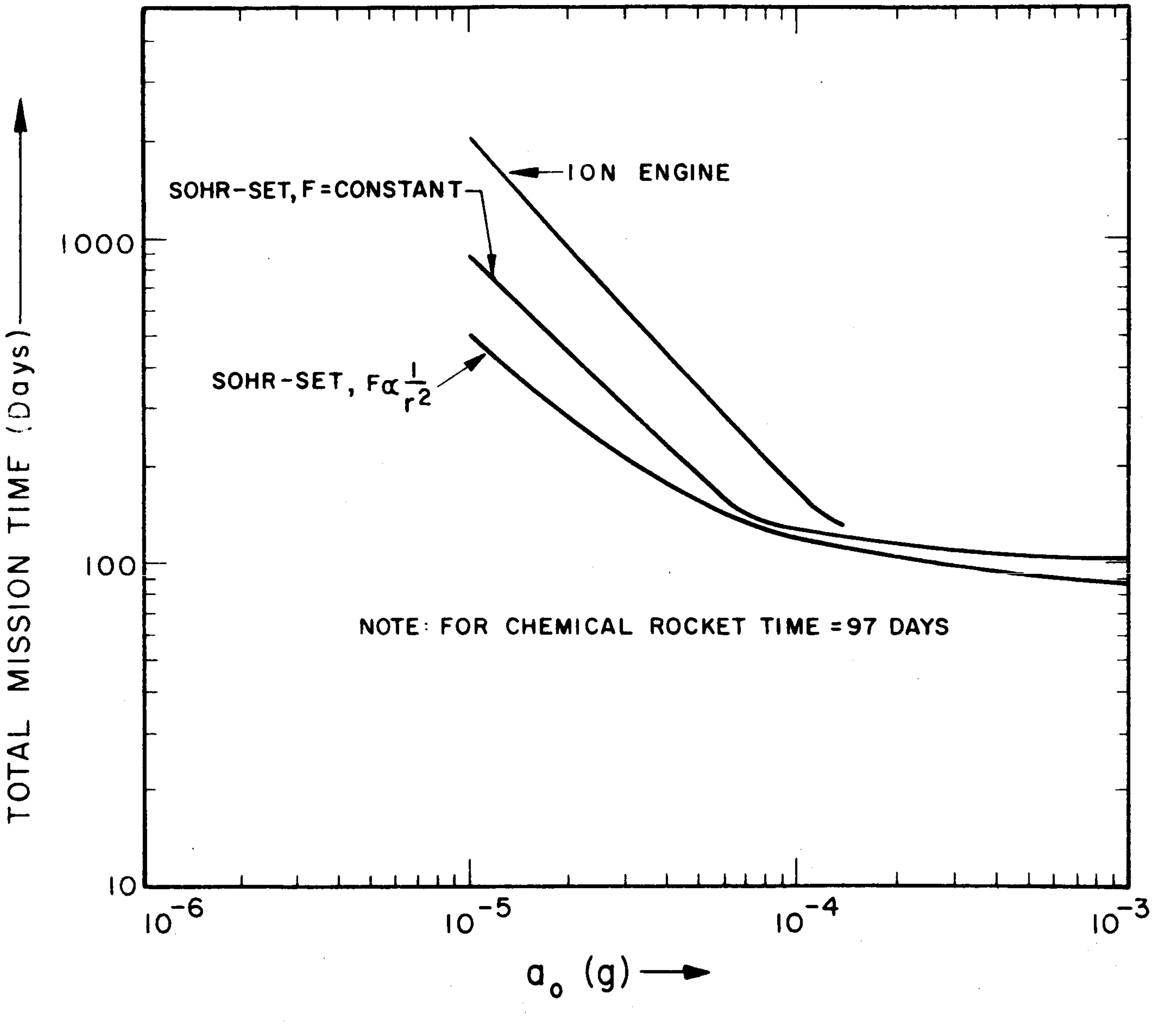

FIG. 7-8 TOTAL MISSION TIME VS INITIAL THRUST ACCELERATION

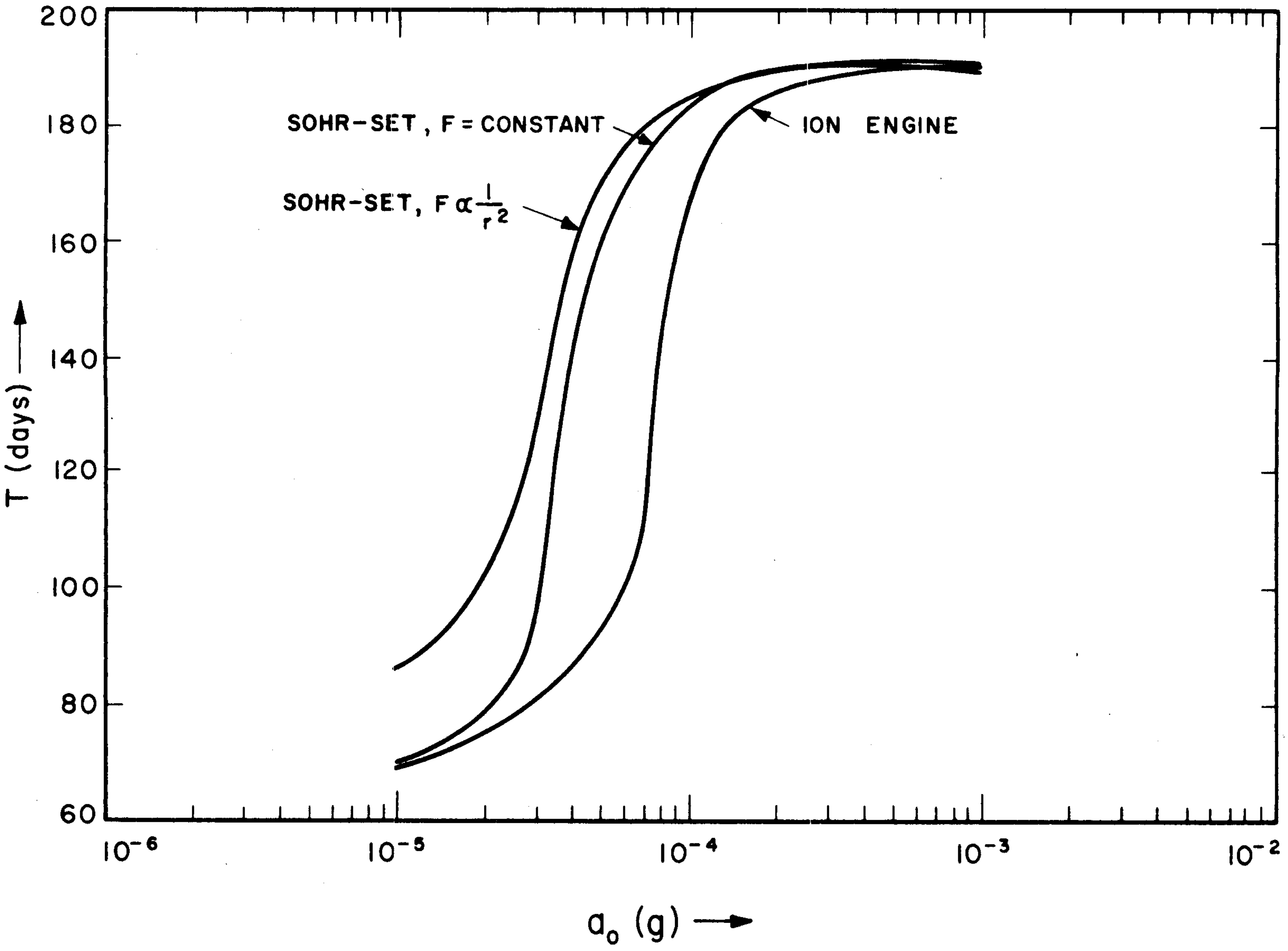

FIG. 7-9 PERIOD OF COAST ELLIPSE VS INITIAL THRUST ACCELERATION

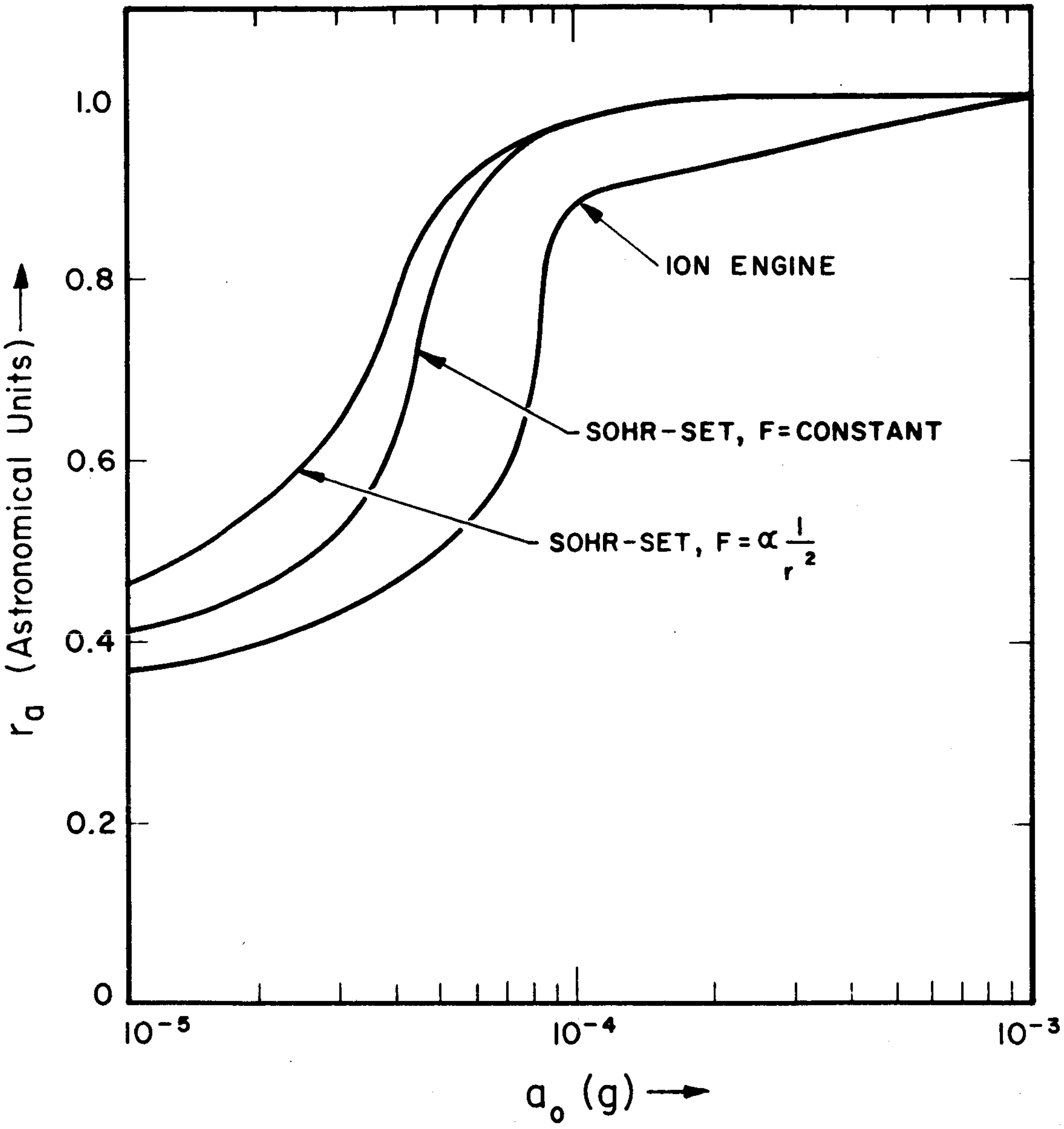

FIG. 7-10 APHELION DISTANCE OF COAST ELLIPSE VS INITIAL THRUST ACCELERATION

at initial thrust accelerations exceeding $a_o = 1.4 \times 10^{-4}$g(refer Fig. 7-7), and although the payload fraction of the SOHR-SET is less than that of the ion engine for $a_o < 1.4 \times 10^{-4}$g, the mission times of the SOHR-SET are significantly less than those of the ion engine for this range of a_o. For thrust accelerations less than 10^{-4}g, the variable thrust ($F \sim 1/r^2$) SOHR-SET delivers a greater payload and provides shorter mission times than the constant thrust SOHR-SET, but the increase in payload is not as impressive as the decrease in mission time. Both ion engine and SOHR-SET are superior to the chemical rocket in "payload" capability, but are inferior in mission time. However, it should be noted that power requirements (excluding conditioning equipment) will be available at approximately 40 lb/kw for the SOHR-SET system, and at 200 lb/kwe for the chemical system assuming solar-cells are used with the latter. Since the power conditioning equipment requirement will be approximately the same for both systems, the true payload advantage of the SOHR-SET will probably be even more favorable.

7.4 SOHR-SET for Synchronous and Lunar Orbit Missions

This part of the study considers transfer from a 300 n. m orbit to a synchronous orbit in detail, and also considers transfer to the lunar orbit, but only to the extent of determining the maximum initial thrust acceleration applicable to such missions. Graphs for the SOHR-SET are plotted with two values of engine (thrustor) efficiency ($\eta = 0.6, 0.8$) to facilitate extrapolation of results which may be of interest due to the variable nature of engine efficiencies that will be encountered. These variations result from the range of thrust and payloads which will be considered in due course. Earlier in this study (Sec. 3.3) the dependence of nozzle energy efficiency on thrust was analyzed and plots were presented. For specific impulses below 800 secs. the frozen flow efficiency for the SOHR-SET system may be regarded as equal to unity, and for all practical purposes $\eta = \eta_N$. Therefore, the correct value of η may be estimated from Sec. 3.3, and the curves in this section used accordingly.

If low thrust is the primary means of propulsion for a space vehicle, then for orbit-lifting missions above the earth the vehicle must initially be placed in a low earth orbit by a chemical rocket since the low thrust is incapable of lifting the vehicle from the earth's surface. Once established in an orbit the low thrust engine can begin thrusting tangent to the orbit, in the direction of motion, thereby adding energy to the orbit and causing the vehicle to move outwards in ever increasing spirals. The engine thrusts continuously until the vehicle reaches the desired orbit altitude, e.g., the synchronous orbit altitude. At this time, the vehicle has a significant radial velocity, due to its motion outward from the earth. Hence, in order to negate this radial velocity and place the vehicle in the synchronous orbit, an appropriate $\Delta\vec{v}$ must be applied to the satellite. This incremental velocity may be imparted by a chemical rocket or by the SOHR-SET system. However, in studying the performance of the SOHR-SET for the synchronous orbit mission, we shall neglect the application of this final orbital correction and consider the mission to be completed when the vehicle attains the synchronous orbit altitude (19,360 n.m).

A measure of the SOHR-SET performance is the amount of payload which it can transport from a low earth orbit to the synchronous orbit. Let M_o be the mass of the vehicle in the initial earth orbit consisting of the payload M_1, the vehicle structure M_s, the power plant M_w and the required propellant M_p. Then we can write

$$\frac{M_1 + M_s}{M_o} = 1 - \frac{M_p}{M_o} - \frac{M_w}{M_o} \tag{7-6}$$

where we have combined M_s with M_1, in order to avoid assigning a value to the structure. Here,

$$\frac{M_p}{M_o} = \frac{t_1}{I_{sp}g} \frac{F}{M_o} \tag{7-7}$$

$$\frac{M_w}{M_o} = \frac{I_{sp}\alpha}{45.8 \, \eta g} \frac{F}{M_o} \tag{7-8}$$

where F = thrust, t_1 = time of flight from initial orbit to synchronous orbit, I_{sp} = specific impulse (sec), η = engine energy efficiency, α = specific mass of the power plant (lb/kw) and $g = 32$ ft/sec^2. Values can be assigned to I_{sp}, α, η and F/M_o, but the equations of motion of the vehicle must be integrated in order to determine t_i. The equations of motion in two dimensions are:

$$\ddot{r} = r \dot{\phi}^2 - \frac{K}{r^2} \tag{7-9a}$$

$$\frac{1}{r} \frac{d}{dt} (r^2 \dot{\phi}) = \frac{F}{M} \tag{7-9b}$$

where r, ϕ are the polar coordinates of the vehicle K the gravitational constant of the earth (14.1×10^{15} ft^3/sec^2), F the thrust and M the vehicle mass. For simplicity, the continuous thrust $\vec{F}$ is maintained perpendicular to the radius vector, $\vec{r}$. $\vec{r}$ and $\vec{F}$ are always in the plane that originally included the parking orbit. For initial conditions we use the fact that the vehicle is originally in a circular parking orbit. For convenience set $\phi(o) = 0$.

Rather than integrating eqs. (7-9a) and (7-9b) on a digital computer, we shall obtain an approximate analytic solution by utilizing the fact that the radial acceleration is very small. Since the ratio F/M will be extremely small ($\sim 10^{-3}g$ or less) for all the engines considered, the orbital spirals will be very nearly circular as the vehicle moves away from the earth except for the case where escape is imminent. We shall therefore assume that $\ddot{r} = 0$. Then eq. (7-9a) gives $r^2\dot{\phi} = (Kr)^{1/2}$, so that eq. (7-9b) becomes

$$\frac{1}{2}\left(\frac{k}{r^3}\right)^{1/2}\frac{dr}{dt} = \frac{F}{M} \qquad (7\text{-}10)$$

We also assume that the propellant flow rate is constant (constant thrust) so that, $M = M_o - \frac{F}{I_g} t$,. Hence, we can perform the following integration:

$$\frac{K^{1/2}}{2}\int_{r_o}^{r}\frac{dr}{r^{3/2}} = \int_{o}^{t}\frac{a_o dt}{1 - \frac{a_o t}{I_{sp}g}} \qquad (7\text{-}11)$$

where, $a_o = F/M_o$ = initial thrust acceleration. Performing the integration gives

$$r^{-1/2} = r_o^{1/2} + \frac{I_{sp}g}{k^{1/2}}\ln\left(1 - \frac{a_o t}{I_{sp}g}\right) \qquad (7\text{-}12)$$

Solving for t we finally have

$$t = \frac{I_{sp}g}{a_o}\left[1 - e^{\frac{1}{I_{sp}g}\sqrt{\frac{k}{r_o}}\left(\sqrt{\frac{r_o}{r}} - 1\right)}\right] \qquad (7\text{-}13)$$

Let r_1 - R (R = radius of earth) = synchronous orbit altitude, and t the flight time between r_o and r_1. Substituting (7-13) in (7-7) then gives

$$\frac{M_p}{M_o} = 1 - e^{\frac{1}{I_{sp}g}\sqrt{\frac{k}{r_o}}\left(\sqrt{\frac{r_o}{r_1}} - 1\right)} \qquad (7\text{-}14)$$

The time dependence of M_p/M_o on a_o is probably weak, since eq. (7-14) which is a good approximation to M_p/M_o - shows that this ratio is independent of a_o. For the purpose of the study, we shall assume that $r_o - R$ = initial orbit altitude = 300 n.mi. Figure (7-11) shows the plot of M_p/M_o vs. specific impulse, I_{sp} obtained from eq. (7-14) for the SOHR-SET, Arc Jet and Ion Engine. We have included the arc jet and ion engine in the study for purposes of comparison. (See Table 7-2).

TABLE 7-2

PROPELLANT MASS RATIOS

Engine	Isp (sec.)	$\frac{M_p}{M_o}$
SOHR	600	0.538
	800	0.440
Arc Jet	1200	0.320
Ion Engine	4000	0.110
Chemical	300	0.73

Before proceeding to the calculation of M_w/M_o and $(M_1 + M_s)/M_o$, we must examine further the limitation of eq. (7-9a). This equation is valid as long as the orbital spirals are nearly circular. However, it is possible that the vehicle may reach escape (from the earth) velocity before arriving at the synchronous altitude, which means that the flight path will cease to be circular and eq. (7-10) will no longer be valid. It is of interest then to know the approximate altitude at which escape occurs. This is obtained by equating the vehicle velocity v to the escape velocity v_e, where $v = (\dot{r}^2 + r^2 \dot{\phi}^2)^{1/2}$ and $v_e = (2k/r)^{1/2}$. Thus,

$$\dot{r}^2 + r^2 \dot{\phi}^2 = \frac{2k}{r} \qquad (7\text{-}15)$$

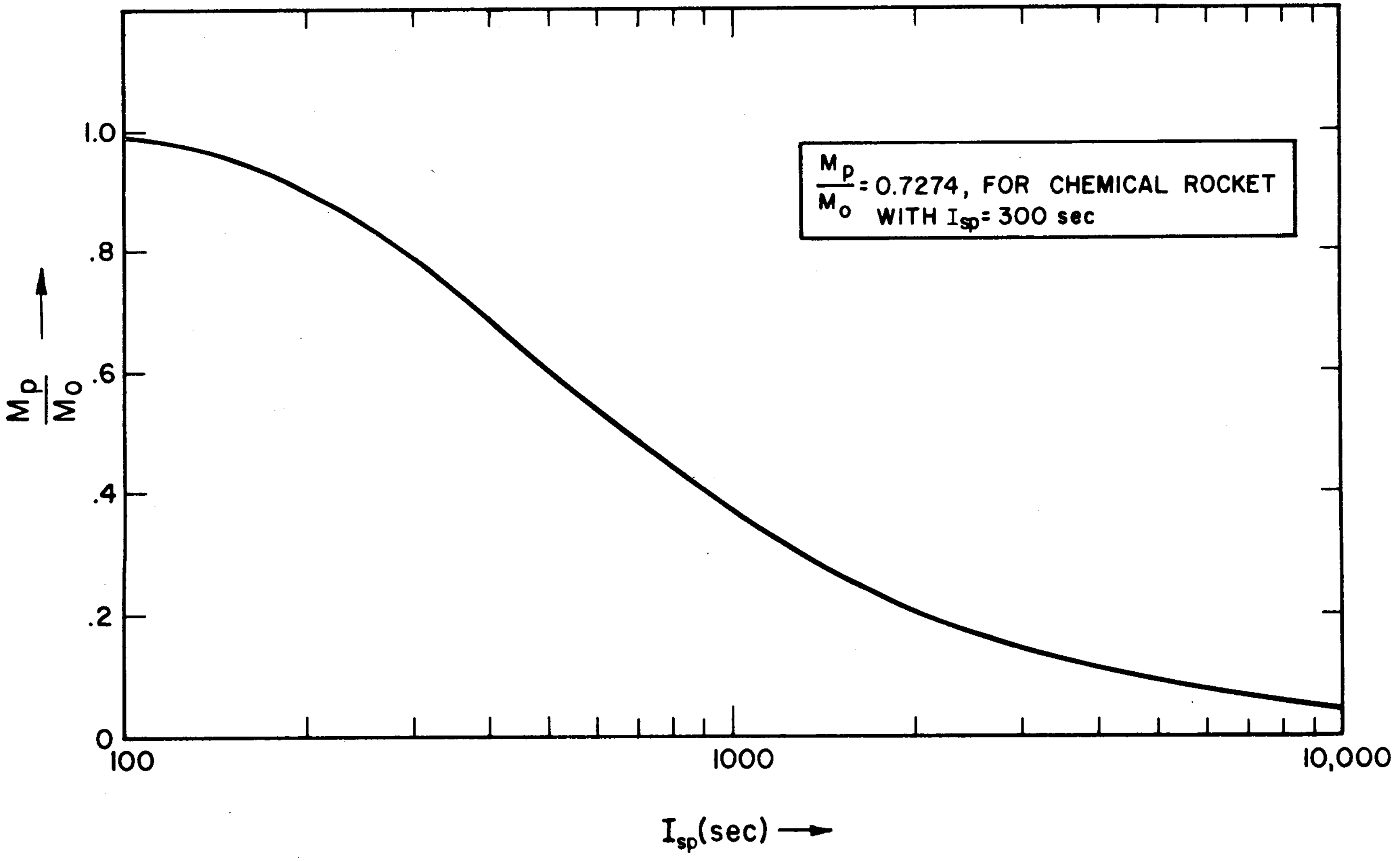

FIG. 7-11 PROPELLANT MASS RATIO (M_p/M_o) VS SPECIFIC IMPULSE (I_{sp}) FOR SOHR-SET, ARC JET, AND ION ENGINES

combining eqs. (7-10) and (7-13) yields

$$\frac{dr}{dt} = 2\, a_o \left(\frac{r^3}{k}\right)^{1/2} e^{\frac{1}{I_{sp}g}\sqrt{\frac{k}{r_o}}\left(1 - \sqrt{\frac{r_o}{r}}\right)} \qquad (7\text{-}16)$$

Also, when $\ddot{r} \sim 0$, eq. (7-9a) gives $r\dot{\phi} = (k/r)^{1/2}$. Substituting this and eq. (7-16) in eq. (7-15), we obtain the following,

$$a_o = \frac{k}{2r_e^2}\; e^{-\frac{1}{I_{sp}g}\sqrt{\frac{k}{r_o}}\left(1 - \sqrt{\frac{r_o}{r_e}}\right)} \qquad (7\text{-}17)$$

where we have replaced r with the escape radius, r_e. It is apparent that eq. (7-17) must be solved graphically for r_e. However, rather than solve (7-17) for r_e, we shall merely let r_e be the radius of the synchronous orbit and obtain a graph of a_o vs specific impulse, I_{sp}. Refer to Fig. (7-12). For general interest, we have also generated a similar plot for the lunar orbit, by letting r_e be the radius of this orbit (207,400 n.mi.). For a given I_{sp}, Fig. (7-12) determines the "critical" initial thrust acceleration a_o' for the synchronous or lunar orbit altitude, i.e., the initial thrust acceleration which will cause the vehicle to escape at this altitude. The quantity a_o' represents the maximum permissable a_o for a given orbit altitude, since any a_o larger than a_o' will cause the vehicle to reach escape velocity before arriving at this altitude. For values of a_o less than a_o', the vehicle will reach escape velocity beyond the desired altitude. As to be expected, Fig. (7-12) shows that, for a given I_{sp} the a_o' for the synchronous orbit is considerably larger than that for the lunar orbit. Table (7-3) shows values of a_o' taken from Fig. (7-12) for the SOHR-SET arc jet and ion engine.

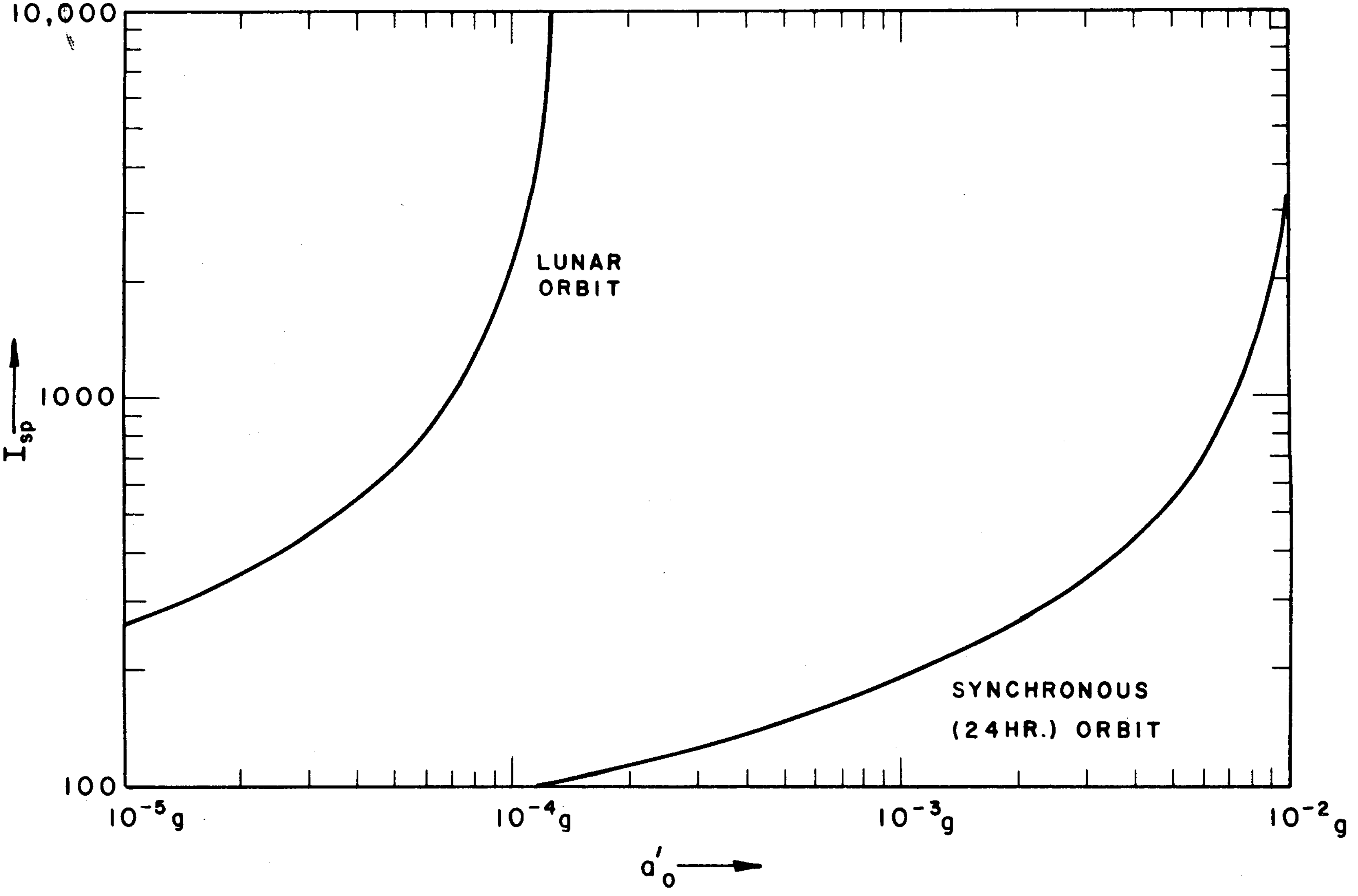

FIG. 7-12 CRITICAL INITIAL THRUST ACCELERATION (a'_o) VS SPECIFIC IMPULSE (I_{sp})

TABLE 7-3

CRITICAL INITIAL THRUST ACCELERATION

Engine	I_{sp}(sec)	a'_o Syn.Orbit	a'_o Lunar Orbit
SOHR-SET	600	$5.33 \times 10^{-3}g$	$4.45 \times 10^{-5}g$
	800	$6.45 \times 10^{-3}g$	$5.90 \times 10^{-5}g$
Arc Jet	1200	$7.83 \times 10^{-3}g$	$7.80 \times 10^{-5}g$
Ion Engine	4000	$1.02 \times 10^{-2}g$	$1.15 \times 10^{-4}g$

Recognising the limitation of eq.(7-10), we how proceed to determine M_w/M_o from eq.(7-8). Table (7-4) shows the values of α and η selected for the three engines.

TABLE 7-4

POWER PLANT SPECIFIC WEIGHT AND THRUSTOR EFFICIENCY

	SOHR-SET	Arc Jet	Ion Engine
α	4 lb/kw_t	40 lb/kw_e	40 lb/kw_e
η	0.60,0.80	0.60	0.60

A realistic range of initial thrust accelerations for these three engines is $10^{-6}g \leq a_o \leq 10^{-2}g$. Fig.(7-13) shows M_w/M_o vs a_o for the SOHR-SET arc jet and ion engine. The dotted line on the far right, at which the curves for the SOHR-SET are terminated, represents the values of a'_o shown in Table 7-3 for the synchronous orbit. For values of a_o to the right of this line, the vehicle will escape before reaching the synchronous altitude, and hence these values are not permissable. The dotted line on the left represents the values of a'_o

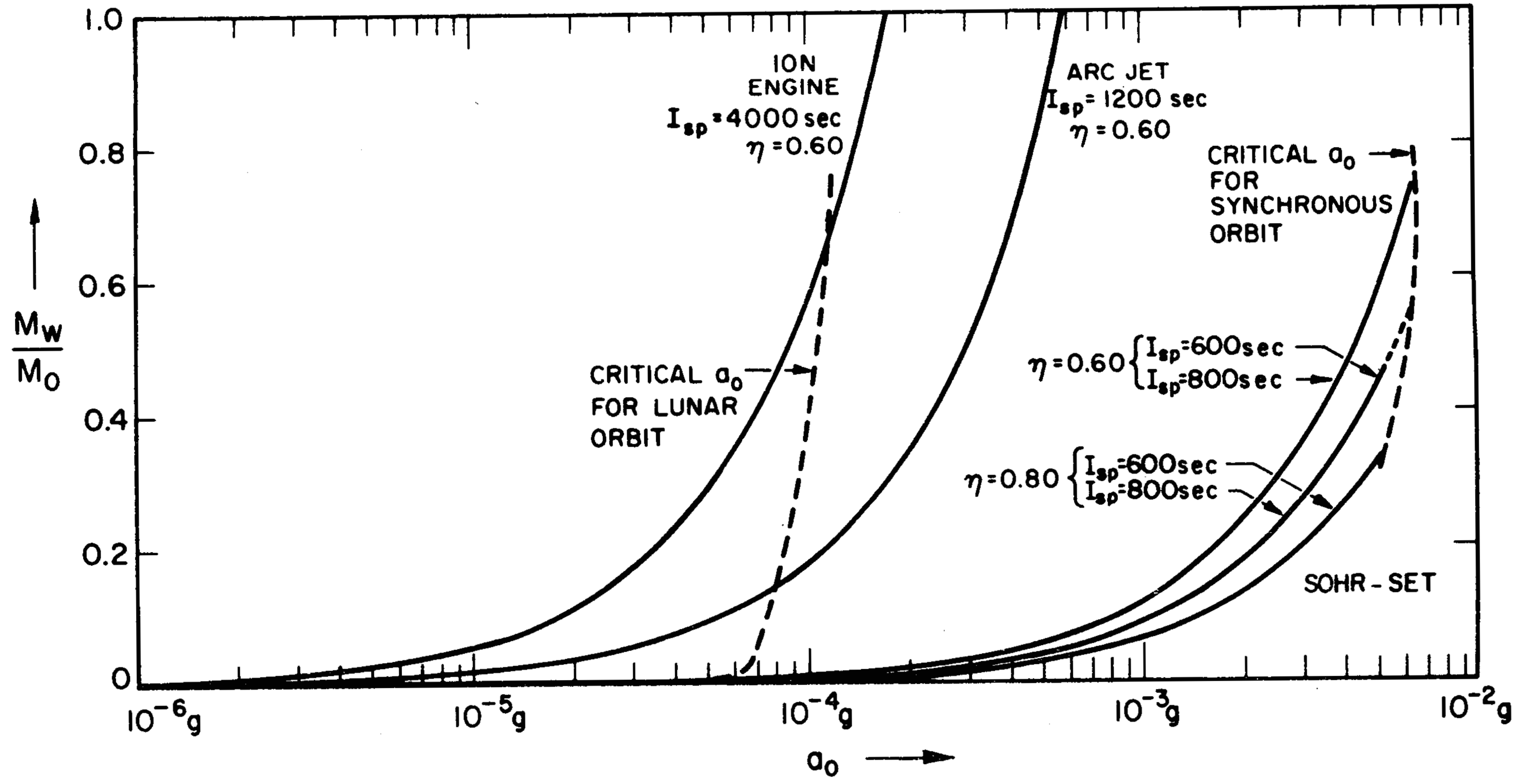

FIG. 7-13 POWER PLANT MASS RATIO (M_W/M_O) VS INITIAL THRUST ACCELERATION (a_o) FOR SOHR-SET, ARC JET, AND ION ENGINES

shown on Table 7-3 for the lunar orbit. Note that the permissible values of a_o for this orbit are less than approximately 10^{-4}_{g}. (This can also be seen in Table 7-3.

Substituting the values of M_p/M_o from Table 7-2 and M_w/M_o from Fig. 7-13 in eq. (7-6), we finally obtain Fig. 7-14, which shows the payload plus structure mass ratio vs a for the SOHR-SET, arc jet and ion engine. Note that the SOHR-SET delivers maximum payload mass fraction at about $a_o \approx 10^{-4}_{g}$, and that this payload ratio is competitive with the payload ratios delivered by the arc jet and ion engine. Due to the large power plants required by the arc jet and ion engine for $a_o > 10^{-4}_{g}$ (ref. Fig. 7-13) these engines are unable to delivery a payload to the synchronous orbit at initial thrust accelerations above $4 \times 10^{-4}_{g}$ and $1.5 \times 10^{-4}_{g}$, respectively.

Also given in Fig. 7-13 is the payload plus structure mass ratio for the chemical rocket ($I_{sp} = 300$ sec.); $(M_l + M_s)/M_o = 0.2725$.

By letting r = radius of synchronous orbit in eq. 7-13, we can compute the mission times for the three engines. These are shown in Fig. 7-15. Note the relatively short flight times for $a_o \geq 10^{-4}_{g}$, which is attainable by the SOHR-SET. Although the arc jet and ion engine can deliver larger payloads than the SOHR-SET the time taken to perform the mission will be significantly larger than that of the SOHR-SET. It should be noted that the minimum transit times for finite payload mass ratios are $t_1 > 35$ days for the ion engine, and $t_1 > 12$ days for the arc jet. It is also significant to mention that the electric thrustors cannot deliver a finite payload to the synchronous orbit in less than about a 30-40 day transit time. Futhermore, this is also dependent on the use of a 40 lb/kw_e - 300 kw type of nuclear-electric system which places a minimum size on the system, below which it is not feasible.

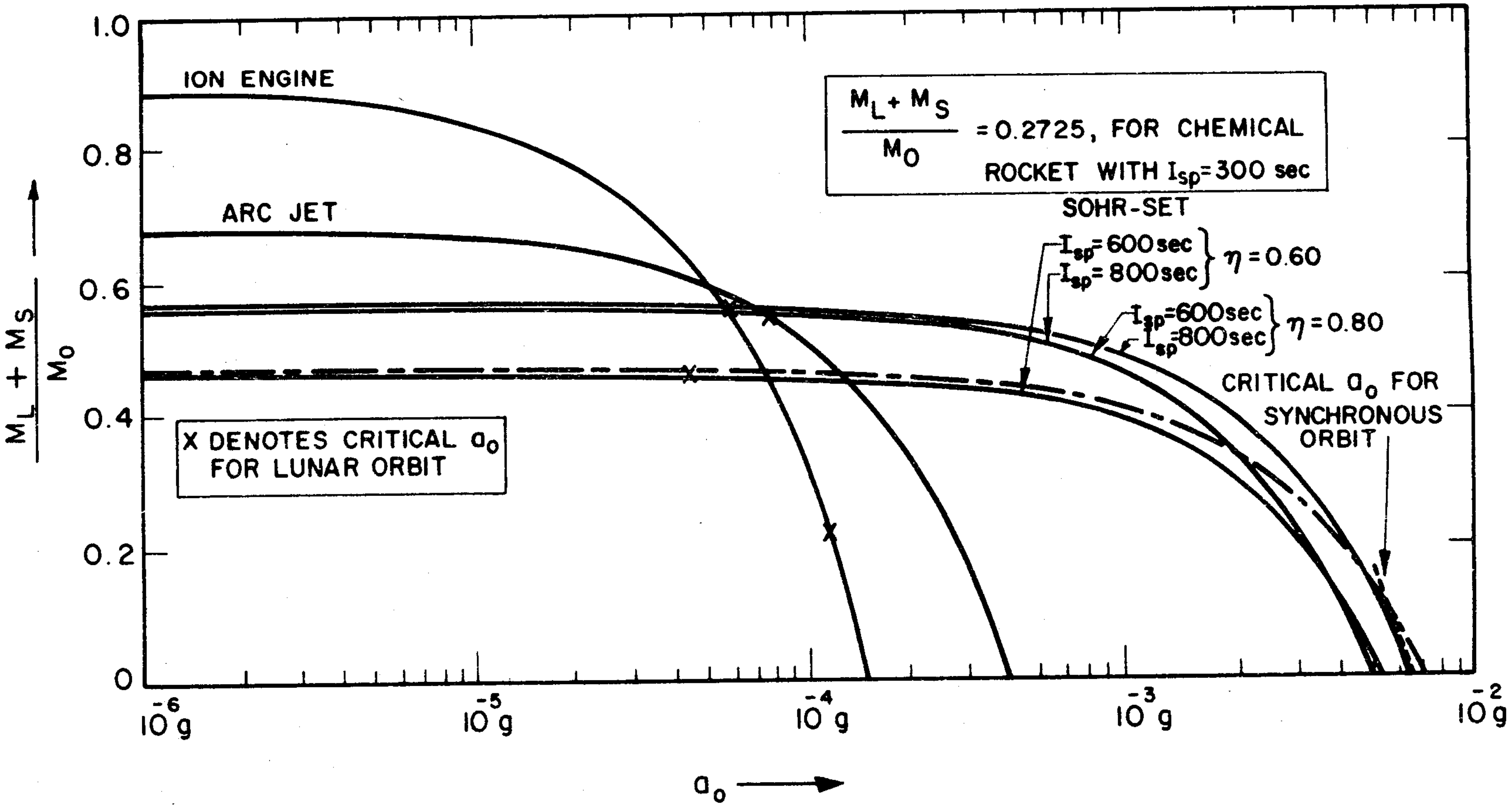

FIG. 7-14 PAYLOAD PLUS STRUCTURE MASS RATIO $\frac{M_l + M_s}{M_o}$ VS INITIAL THRUST ACCELERATION (a_o) FOR SOHR-SET, ARC JET, AND ION ENGINES

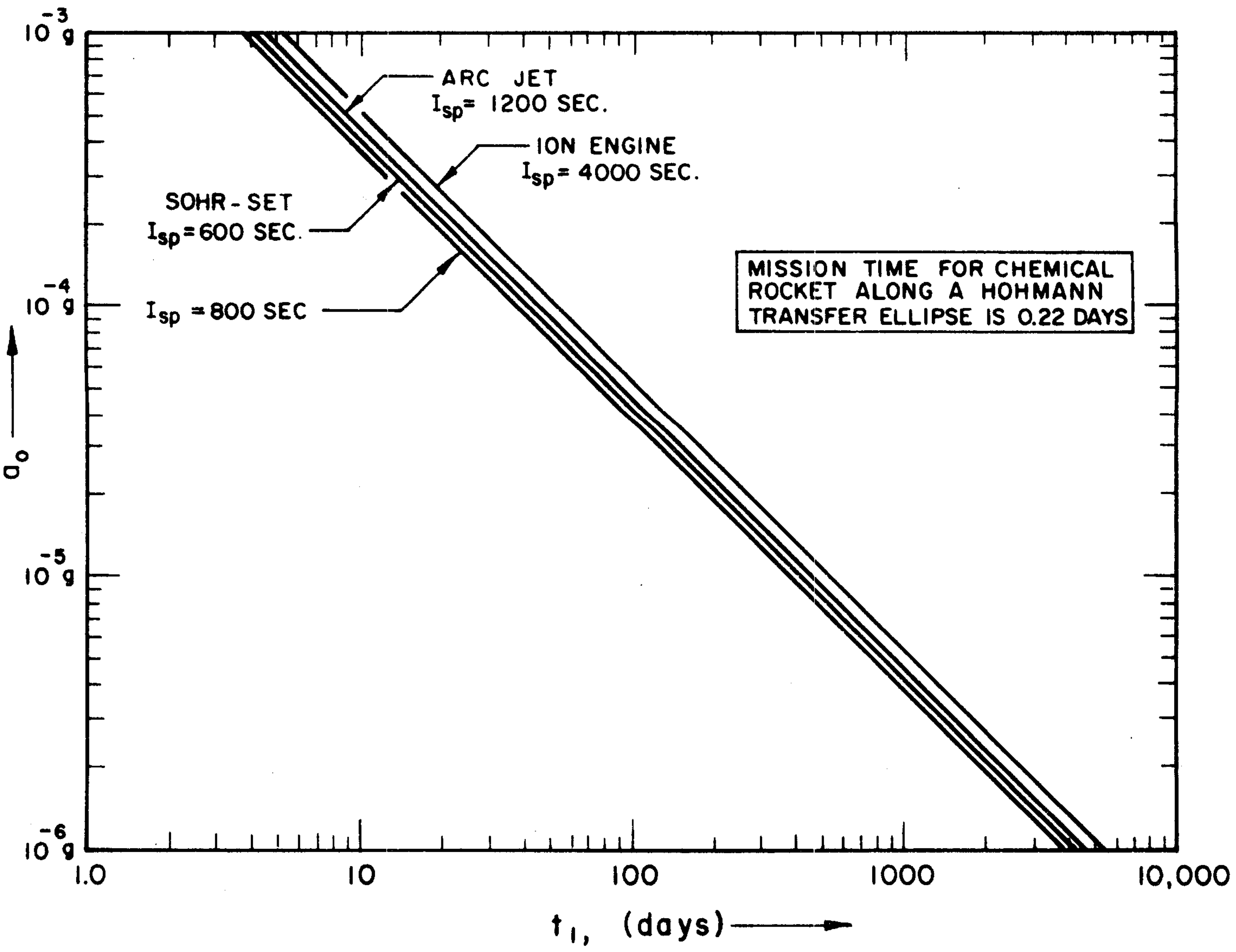

FIG. 7-15 SYNCHRONOUS ORBIT MISSION TIME (t_1) VS INITIAL THRUST ACCELERATION FOR SOHR-SET, ARC JET, AND ION ENGINES

DISTRIBUTION LIST FOR FINAL REPORT

6/10/64

Contract NAS7-231

"Design Study of a Solar Hydrogen Propulsion and Power System"

Electro-Optical Systems, Inc.

Report is to be sent directly to the "Recipients" marked with an "X" under the column headed "Designee" on Pages 1 and 2 only. On Pages 3 thru 10, the report should be sent to the Technical Librarian of the "Recipient" with a carbon copy of the letter of transmittal to the attention of the person named under the column "Designee". The letter of transmittal should contain the contract number and complete title of the final report.

The distribution list should be included in the final report as an appendix.

COPIES	RECIPIENT	DESIGNEE
	NASA Headquarters, Washington, D. C. 20546	
1	Contracting Officer, BCA	( )
1	Patent Office, AGP	( )
	NASA Lewis Research Center 21000 Brookpark Road Cleveland, Ohio 44135	
1	Office of Technical Information	( )
1	Contracting Officer	( )
1	Patent Office	( )
	NASA Marshall Space Flight Center Huntsville, Alabama 35812	
1	Office of Technical Information, M-MS-IPC	( )
1	Contracting Officer, M-P&C-C	( )
1	Patent Office, M-PAT	( )
	NASA Western Operations Office 150 Pico Boulevard Santa Monica, California 90406	
1	Office of Technical Information	(X)
1	Contracts Management Division	(X)
1	General Counsel for Patent Matters	(X)

COPIES	RECIPIENT	DESIGNEE
	NASA Headquarters, Washington, D. C. 20546	
4	Mr. Henry Burlage, Jr. Chief, Liquid Propulsion Technology, RPL	(X)
1	Mr. Vernon E. Jaramillo Advanced Manned Mission, MTC	(X)
25	Scientific and Technical Information Facility NASA Representative, Code CRT P. O. Box 5700 Bethesda, Maryland 20014	(X)
1	(Technical Manager) Mr. John Sanders Mail Stop 54-1 NASA Lewis Research Center 21000 Brookpark Road Cleveland, Ohio 44135	(X)

NASA FIELD CENTERS

COPIES	RECIPIENT	DESIGNEE
2	Ames Research Center Moffett Field, California 94035	Harold Hornby Mission Analysis Division
2	Goddard Space Flight Center Greenbelt, Maryland 20771	Merland L. Moseson Code 623
2	Jet Propulsion Laboratory California Institute of Technology 4800 Oak Grove Drive Pasadena, California 91103	Robert F. Rose Propulsion Div., 38
2	Langley Research Center Langley Station Hampton, Virginia 23365	Floyd L. Thompson Director
2	Lewis Research Center 21000 Brookpark Road Cleveland, Ohio 44135	Dr. Abe Silverstein Director
2	Marshall Space Flight Center Huntsville, Alabama 35812	Hermann K. Weidner Code R-P&VED
2	Manned Spacecraft Center Houston, Texas 77001	Robert R. Gilruth Director
2	Western Operations Office 150 Pico Boulevard Santa Monica, California 90406	Robert W. Kamm Director

GOVERNMENT INSTALLATIONS

COPIES	RECIPIENT	DESIGNEE
1	Advanced Research Projects Agency Washington 25, D. C.	D. E. Mock
1	Aeronautical Systems Division Air Force Systems Command Wright-Patterson Air Force Base Dayton, Ohio 45433	D. L. Schmidt Code ASRCNC-2
1	Air Force Missile Development Center Holloman Air Force Base, New Mexico	Maj. R. E. Bracken Code MDGRT
1	Air Force Missile Test Center Patrick Air Force Base, Florida	L. J. Ullian
1	Air Force Systems Command, Dyna-Soar Air Force Unit Post Office Los Angeles 45, California	Col. Clark Technical Data Center
1	Arnold Engineering Development Center Arnold Air Force Station Tullahoma, Tennessee	Dr. H. K. Doetsch
1	Bureau of Naval Weapons Department of the Navy Washington 25, D. C.	J. Kay, Code RTMS-41
	[redacted]	
1	Defense Documentation Center Headquarters Cameron Station, Building 5 5010 Duke Street Alexandria, Virginia 22314 Attn: TISIA	
1	Headquarters, U. S. Air Force Washington 25, D. C.	Col. C. K. Stambaugh Code AFRST
1	Picatinny Arsenal Dover, New Jersey 07801	I. Forsten, Chief, Liquid Propulsion Laboratory

GOVERNMENT INSTALLATIONS

COPIES	RECIPIENT	DESIGNEE
1	Rocket Research Laboratories Edwards Air Force Base Edwards, California 93523	Colonel Silk
1	U. S. Atomic Energy Commission Technical Information Services Box 62 Oak Ridge, Tennessee	
1	U. S. Army Missile Command Redstone Arsenal, Alabama 35809	Dr. Walter Wharton
1	U. S. Naval Ordnance Test Station China Lake, California 93557	Code 451 Chief, Missile Propulsion Division
1	U. S. Atomic Energy Commission Technical Information Services Germantown, Maryland	Patrick A. O'Riordan

CPIA

1	Chemical Propulsion Information Agency Johns Hopkins University Applied Physics Laboratory 8621 Georgia Avenue Silver Spring, Maryland	Neil Safeer

COMMERCIAL CONTRACTORS

COPIES	RECIPIENT	DESIGNEE
1	Aerojet-General Corporation P. O. Box 296 Azusa, California	L. F. Kohrs
1	Aerojet-General Corporation P. O. Box 1947 Technical Library, Bldg 2015, Dept 2410 Sacramento 9, California 95809	R. Stiff
1	Aeronutronic A Division of Ford Motor Company Ford Road Newport Beach, California	Hans Linhardt
1	Aerospace Corporation 2400 East El Segundo Boulevard P. O. Box 95085 Los Angeles, California 90045	John G. Wilder MS-2293 Propulsion Dept.
1	Arthur D. Little, Inc. Acorn Park Cambridge 40, Massachusetts	A. C. Tobey
1	Astropower, Inc., Subsidiary of Douglas Aircraft Company 2968 Randolph Avenue Costa Mesa, California	Dr. George Moc Director, Research
1	Astrosystems, Inc. 1275 Bloomfield Avenue Caldwell Township, New Jersey	A. Mendenhall
1	Atlantic Research Corporation Edsall Road and Shirley Highway Alexandria, Virginia	A. Scurlock
1	Beech Aircraft Corporation Boulder Facility Box 631 Boulder, Colorada	J. H. Rodgers

COMMERCIAL CONTRACTORS

COPIES	RECIPIENT	DESIGNEE
1	Bell Aerosystems Company P. O. Box 1 Buffalo 5, New York	W. M. Smith
1	Bendix Systems Division Bendix Corporation Ann Arbor, Michigan	John M. Brueger
1	Boeing Company P. O. Box 3707 Seattle 24, Washington	J. D. Alexander
1	Chrysler Corporation Missile Division Warren, Michigan	John Gates
1	Curtiss-Wright Corporation Wright Aeronautical Division Wood-ridge, New Jersey	G. Kelley
1	Douglas Aircraft Company, Inc. Missile and Space Systems Division 3000 Ocean Park Boulevard Santa Monica, California 90406	R. W. Hallet Chief Engineer Advanced Space Tech.
1	Fairchild Stratos Corporation Aircraft Missiles Division Hagerstown, Maryland	J. S. Kerr
1	General Dynamics/Astronautics Library & Information Services (128-00) P. O. Box 1128 San Diego, California 92112	Frank Dore
1	General Electric Company Missile and Space Vehicle Department 3198 Chestnut Street, Box 8555 Philadelphia 1, Pennsylvania 19101	Dr. Joseph Danko
1	General Electric Company One River Road Schenectady, New York 12305	Dr. John Houston

COMMERCIAL CONTRACTORS

COPIES	RECIPIENT	DESIGNEE
1	General Electric Company Flight Propulsion Lab Department Cincinnati 15, Ohio	D. Suichu
1	Grumman Aircraft Engineering Corp. Bethpage, Long Island, New York	Joseph Gavin
1	Kidde Aero-Space Division Walter Kidde and Company, Inc. 675 Main Street Belleville 9, New Jersey	R. J. Hanville Director of Research Engineering
1	Lockheed California Company 10445 Glen Oaks Boulevard Pacoima, California	G. D. Brewer
1	Lockheed Missiles and Space Company Attn: Technical Information Center P. O. Box 504 Sunnyvale, California	Y. C. Lee Power Systems R&D
1	Lockheed Propulsion Company P. O. Box 111 Redlands, California	H. L. Thackwell
1	The Marquardt Corporation 16555 Saticoy Street Box 2013 - South Annex Van Nuys, California 91409	Warren P. Boardman, Jr
1	Martin Division Martin Marietta Corporation Baltimore 3, Maryland	John Calathes (3214)
1	Martin Denver Division Martin Marietta Corporation Denver, Colorado 80201	J. D. Goodlette Mail A-241
1	McDonnell Aircraft Corporation P. O. Box 6101 Lambert Field, Missouri	R. A. Herzmark

COMMERCIAL CONTRACTORS

COPIES	RECIPIENT	DESIGNEE
1	North American Aviation, Inc. Space & Information Systems Division Downey, California	H. Storms
1	Northrop Corporation 1001 East Broadway Hawthorne, California	W. E. Gasich
1	Pratt & Whitney Aircraft Corp. Florida Research and Development Center P. O. Box 2691 West Palm Beach, Florida 33402	R. J. Coar
1	Radio Corporation of America Astro-Electronics Division Defense Electronic Products Princeton, New Jersey	S. Fairweather
1	Reaction Motors Division Thiokol Chemical Corporation Denville, New Jersey 07832	Arthur Sherman
1	Republic Aviation Corporation Farmingdale, Long Island, New York	Dr. William O'Donnell
1	Rocketdyne (Library Dept. 586-306) Division of North American Aviation 6633 Canoga Avenue Canoga Park, California 91304	E. B. Monteath
1	Space General Corporation 9200 Flair Avenue El Monte, California	C. E. Roth
1	Space Technology Laboratories Subsidiary of Thompson-Ramo-Wooldridge P. O. Box 95001 Los Angeles 45, California	G. W. Elverum
1	Stanford Research Institute 333 Ravenswood Avenue Menlo Park, California 94025	Thor Smith

COMMERCIAL CONTRACTORS

COPIES	RECIPIENT	DESIGNEE
1	TAPCO Division Thompson-Ramo-Wooldridge, Inc. 23555 Euclid Avenue Cleveland 17, Ohio	William Leovic
1	Thiokol Chemical Corporation Redstone Division Huntsville, Alabama	John Goodloe
1	United Aircraft Corporation Research Laboratories 400 Main Street East Hartford 8, Connecticut 06108	Erle Martin
1	United Technology Center 587 Methilda Avenue P. O. Box 358 Sunnyvale, California	B. Abelman
1	Vought Astronautics Box 5907 Dallas 22, Texas	Warren C. Trent
1	Electro-Optical Systems, Inc. 125 North Vinedo Avenue Pasadena, California	Dr. A. O. Jensen
1	Research Laboratory General Motors Technical Center Warren, Michigan	Dr. Donald L. Dresser
1	Allison Division General Motors Corporation Indianapolis 6, Indiana	Dr. R. F. Henderson
1	Goodyear Aircraft Corporation 1210 Massillon Road Akron, Ohio 44315	T. J. McCusker